Max Planck Graduate Center
mit der Johannes Gutenberg-Universität

JOHANNES GUTENBERG UNIVERSITÄT MAINZ

JG|U

Computational Study of Segregation Phenomena in Polymer Systems in and out of Equilibrium

Dissertation

for attaining the academic degree of

Doctor rerum naturalium (Dr.rer.nat.)

in accordance with the regulations of the ***Max Planck Graduate Center****, of the departments*

08-Physics, Mathematics, and Computer Science

09-Chemistry, Pharmaceutical Sciences, Geography, and Geosciences

10-Biology, and University of Medicine

of the

Johannes Gutenberg University,Mainz

submitted by

Deepika Srivastva

April 5, 2022

Tag der mündlichen prüfung June 22, 2021

DECLARATION

I, Deepika Srivastva, hereby declare that I wrote the dissertation titled, *Computational Study of Segregation Phenomena in Polymer Systems in and out of Equilibrium* without any unauthorized external assistance and used only sources acknowledged in the work. All textual passages which are appropriated verbatim or paraphrased from published and unpublished texts as well as all information obtained from oral sources are duly indicated and listed in accordance with bibliographical rules. In carrying out this research, I complied with the rules of standard scientific practice as formulated in the statutes of Johannes Gutenberg University, Mainz to insure standard scientific practice.

This dissertation includes three original manuscripts published in peer-reviewed journals and one manuscript in preparation. All published work reprinted with permission.

Deepika Srivastva

Dedicated to my Parents…

PUBLICATIONS

- Srivastva, D., & Nikoubashman, A. (2018). Flow behavior of chain and star polymers and their mixtures. Polymers, 10(6), 599.
- Steinhaus, A., Srivastva, D., Nikoubashman, A., & Gröschel, A. H. (2019). Janus Nanostructures from ABC/B Triblock Terpolymer Blends. Polymers, 11(7), 1107.
- Steinhaus, A., Srivastva, D., Qiang, X., Franzka, S., Nikoubashman, A., & Gröschel, A. H. (2021). Controlling Janus Nanodisc Topology through ABC Triblock Terpolymer/Homopolymer Blending in 3D Confinement. Macromolecules, 54(3), 1224-1233.
- Srivastva, D., & Nikoubashman, A. (2021). Self-assembly of Amphiphilic Polymers into Patchy Polymerosomes. [To be submitted]

ABSTRACT

Segregation phenomena play a key role in the pattern evolution of immiscible multicomponent mixture ranging from simple to complex fluids such as polymers, surfactants, colloids, emulsions *etc.*, and have applications in various fields. In this thesis, we investigate the flow and phase separation of different polymer architectures using computer simulation techniques. We report the effect of macromolecular architecture on the flow properties of polymers and show that the polymer distribution is uniform throughout the channel for both star and chain polymers under steady conditions. While in the presence of flow, the star-shaped polymers migrate more strongly towards the channel center, leading to a flow-based separation of linear and star polymers, with chains accumulating near the channel walls and star polymers at the center. This can help in designing the microfluidic devices for separating polymers based on their architecture. Furthermore, we study the phase separation of triblock copolymers in the melt and solution. We show that the blending of B homopolymer into lamella morphologies of ABC triblock terpolymer allows the continuous tuning of the B microphase in the melt and solution. We vary the volume fraction of homopolymer in the system and find that for polymer melts, the morphological transition of B microphase goes from cylinder to perforated lamellae and further to continuous lamellae. Moreover, for the polymer solution, the transition is from concentric rings to perforated lamellae and finally to continuous lamellae in a microemulsion droplet. Along with the morphological evolution, we rationalize the stability of such microemulsion droplets with our simulations and theoretical considerations. The results from our study suggest that we can generate more complex Janus nanostructures from triblock copolymers. Lastly, we show that the amphiphilic triblock copolymer phase separates into polymerosomes; the architecture and the arrangement of blocks within the triblock copolymer impact the morphology. Additionally, we display that the volume fraction of the hydrophilic blocks influences the

self-assembled morphology of the polymerosome by changing its cavity size, shape, and patches. In general, we show a way to design the polymerosomes with distinct patches on the surface, which can aid in enhancing the on-target effects in drug delivery applications.

ZUSAMMENFASSUNG

Seigerungphänomene spielen eine Schlüsselrolle bei der Musterbildung von nicht mischbaren Mehrkomponentengemischen, die von einfachen bis zu komplexen Flüssigkeiten wie Polymeren, Tensiden, Kolloiden, Emulsionen *etc.*, reichen und in verschiedenen Bereichen Anwendung finden. In dieser Arbeit untersuchen wir die Fluss- und die Phasenseparation verschiedener Polymerarchitekturen mithilfe von Computersimulationstechniken. Wir berichten über die Auswirkung der makromolekularen Architektur auf die Fließeigenschaften von Polymeren und zeigen, dass die Polymerverteilung sowohl für Stern- als auch für Kettenpolymere unter stabilen Bedingungen im gesamten Kanal gleichmäßig ist. In Gegenwart von Strömung wandern die sternförmigen Polymere stärker in Richtung des Kanalzentrums, was zu einer strömungsbasierten Trennung von ketten und Sternpolymeren führt, wobei sich Ketten in der Nähe der Kanalwände und Sternpolymere im Zentrum ansammeln. Dies kann beim Entwurf von Mikrofluidikvorrichtungen zum Trennen von Polymeren basierend auf ihrer Architektur hilfreich sein. Darüber hinaus untersuchen wir die Phasentrennung von Triblockcopolymeren in der Schmelze und in Lösung. Wir zeigen, dass das Beimischen von B-Homopolymer in die Lamellenmorphologien von ABC-Triblockterpolymer die kontinuierliche variation der B-Mikrophase in der Schmelze und auch in der Lösung ermöglicht. Wir variieren den Volumenanteil des Homopolymers im System und stellen fest, dass Bei Polymerschmelzen verläuft der morphologische Übergang der B-Mikrophase von zylindrischen zu perforierten Lamellen und weiter zu kontinuierlichen Lamellen. Darüber hinaus erfolgt für die Polymerlösung der Übergang von konzentrischen Ringen zu perforierten Lamellen und schließlich zu kontinuierlichen Lamellen in einem Mikroemulsionströpfchen. Zusammen mit der morphologischen Entwicklung erklären wir die Stabilität solcher Mikroemulsionströpfchen mit unseren Simulationen und theoretischen Überlegungen. Die Ergebnisse unserer Studie legen nahe, dass wir aus Triblockcopolymeren

komplexere Janus-Nanostrukturen erzeugen können. Zuletzt zeigen wir, dass sich die amphiphile Triblockcopolymerphase in Polymerosome trennt; Die Architektur und die Anordnung der Blöcke innerhalb des Triblockcopolymers beeinflussen die Morphologie. Zusätzlich zeigen wir, dass die Hydrophilie der Blöcke die selbstorganisierten Morphologien beeinflusst, indem sie die Größe des Hohlraums, die Flecken auf der Oberfläche und die Form der Polymerosome ändert. Im Allgemeinen zeigen wir einen Weg, die Polymerosomen mit unterschiedlichen Flecken auf der Oberfläche zu gestalten, was dazu beitragen kann, die zielgerichteten Effekte bei Anwendungen zur Arzneimittelabgabe zu verbessern.

CONTENTS

1

INTRODUCTION

Polymers are an important class of materials and are being used in a wide range of applications from everyday household items, packaging materials to high-tech fibers [1], medical devices and wearable electronics [2]. They are cheap with tunable properties and are easy to process. Moreover, end-user industries are using polymers to substitute glass, paper, and metals due to their low weight and cost, which is anticipated to bolster the Global Polymer Market's growth over the coming years [3, 4].

Conformational changes in polymers through external fields are significant from a fundamental and an application point of view [5, 6]. It plays a vital role in a broad spectrum of applications like polymer extruders, microfluidics [7], and biological systems, like in blood flow [8, 9]. The complex motions of polymers in flow can strongly perturb the flow field of the fluid due to its hydrodynamic interactions (HI). Thus, there is an increasing interest to use this coupling between the deformable polymers and their disturbed flow field [10, 11]. These polymers, also known as soft particles, have quite intriguing dynamical behavior within a flow, including tank-treading, tumbling, stretching, collapse, and cross-stream migration [12–14].

The cross-stream migration of particles under flow in a microchannel is beneficial in separation technology, especially in filtration, cell sorting *etc.* In this regard, separating particles based on their rigidity will have an impactful application in the field of medical sciences. For example, cancerous cells are softer than their healthy counterparts [15], and hence microfluidic devices can be used as a cheap and fast tool for diagnostics of lethal diseases like cancer. On the other hand, conventional cell separation techniques like fluorescence-activated cell sorting (FACS) [16–18], count on the intrinsic properties (like density) or external labels of the cells and are very complicated and expensive. From this perspective, exploring the possibility to sepa-

rate particles based on their cell shape and elasticity opens a gateway to detect lethal diseases at a very early stage. Hence, microfluidic separation methods [19–22] allows for novel sorting modalities and takes advantage of the smaller scale, which can help make such cell separation cost-effective and easy to use.

Star-shaped polymers are a promising candidate to study such separation phenomena under flow because they show a continuous change of properties from linear chains to spherical colloidal particles with a soft pair potential. Also, we can tune the properties of such star polymers by changing the length and the number of arms of the polymer [23].

Separation can also occur in polymers when they are in equilibrium, considering different polymer segments linked via covalent bonds. Such systems form microphase-separated nanostructures by self-assembly of block copolymers [24, 25]. These morphologies have a wide range of industrial applications like sensors, nanoreactors, and dispersant technology, to name a few. The self-assembly of linear diblock copolymers and their phase behavior is very well-known for since long [26, 27]. In contrast, the phase behavior of multiblock polymers like a triblock copolymer and more complex architectures like star polymers remain incomplete due to the larger parameter space.

Computer simulations play an important role in understanding and supporting experimental results at atomistic (molecular calculations) and electronic (quantum calculations) levels. The development of reliable simulation techniques has made computer simulation predictions reflect the experiments adequately. Here, in this work, with the help of computer simulations, we are exploring new conformations and structures that can help deep dive into the research of polymeric systems, which are otherwise expensive and tedious to conduct experimentally. We use Molecular Dynamics (MD) simulations and coarse-grained simulations approach to gain insight at the microscopic level to the flow behavior of star polymers and their mixtures with different arm numbers and phase behavior of block copolymers, especially triblock copolymers of varied architecture.

This thesis is presented in the following order:

In **chapter 2**, we describe the physics of polymer solutions in addition to their thermodynamic behavior. We also discuss the polymer dynamics and the models

describing the flow properties of polymers in confinement and the basics of the self-assembly behavior of block copolymers in melts and solution.

Chapter 3 briefly discusses the simulation techniques used in this work with a focus on the MD simulations and coarse-grained (CG) simulations like Multi Particle Collision Dynamics (MPCD) and Dissipative Particle Dynamics (DPD). We also detail the different representations of polymer models, like the bead spring model.

Chapter 4 examines the flow behavior of single star polymers and their mixtures in ultradilute conditions in a pressure-driven flow. We use a hybrid approach that combines MD and MPCD to study such systems. Here, we show the migration of stars to the channel center with an increasing flow rate. At a specific flow rate, the stars with the higher number of arms are more likely to be found in the channel center leading to a flow-based separation.

In **chapter 5**, we investigate the self-assembly of polystyrene- *b*-polybutadiene-*b*-polymethylmethacrylate (SBM) triblock terpolymer melt with homopolymer Polybutadiene (hPB) blending using DPD simulations. We confirm cylinders in lamellae morphology for the SBM terpolymer system, which is in sync with the complementary experiments. For the blended systems, we show the morphological evolution of B microphase with hPB addition.

In **chapter 6**, we report a variety of morphologies synthesized from ABC triblock terpolymer microphases in microemulsion droplets using DPD simulations. Along with the experiments, we show that the self-assembly of the ABC triblock terpolymers leads to a prolate microparticle with A/C lamellae stacked along the particle's major axis.

In the last **7^{th} chapter**, we use DPD simulations to unravel different morphologies for diverse architecture of triblock copolymers. Further, we explore the morphologies of different polymer block arrangements within the polymer chain. We also show the effect of hydrophilic block length on the nanostructures.

2

THEORETICAL BACKGROUND

2.1 POLYMER PHYSICS

The discovery of polymers came into existence in the nineteenth century when chemists started synthesizing polymers. Polymers are generally repeating units of monomers [28] connected via covalent bonds. The process of generating polymers is called polymerization, and the number of monomers in each polymer gives the degree of polymerization. The molar mass $M_n = NM_m$ with N and M_m being the degree of polymerization and the molar mass of the monomers, respectively. The properties of the polymer are the chemical identity of monomers and the microstructure of the polymeric system.

Polymer chains are either made of monomers of the same type (homopolymers) or different types (heteropolymers). Although the same type of monomers forms the homopolymer, they still differ as per the degree of polymerization, microstructure, and architecture. The polymer architecture can be, for example, linear, circular, star-branched, H-branched, ladder-like, dendritic, or randomly branched (shown in Figure 1). Based on the architecture, polymers can possess different properties like solution viscosity, solubility in solvents, and glass transition temperature [29], which makes them useful in a variety of industrial applications.

Heteropolymers are usually a combination of different types of monomers with unique properties, and the sequence of combination and composition of such monomers defines their properties. A polymer containing two different monomers is called a copolymer, and the monomer is arranged in many ways like alternating, random, block, or graft (Figure 2). Also, based on the number of blocks a polymer contains, they can be categorized as diblock (two blocks), triblock (three blocks), or multiblock

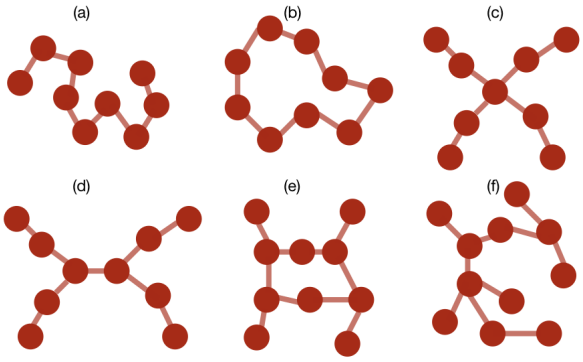

Figure 1: Different types of polymer architecture, (**a**) linear, (**b**) circular, (**c**) star-branched, (**d**) H-branched, (**e**) ladder-like, (**f**) randomly branched polymer.

(many blocks), as shown in Figure 2. Some of the naturally occurring heteropolymers are DNA (deoxyribonucleic acid), proteins *etc*.

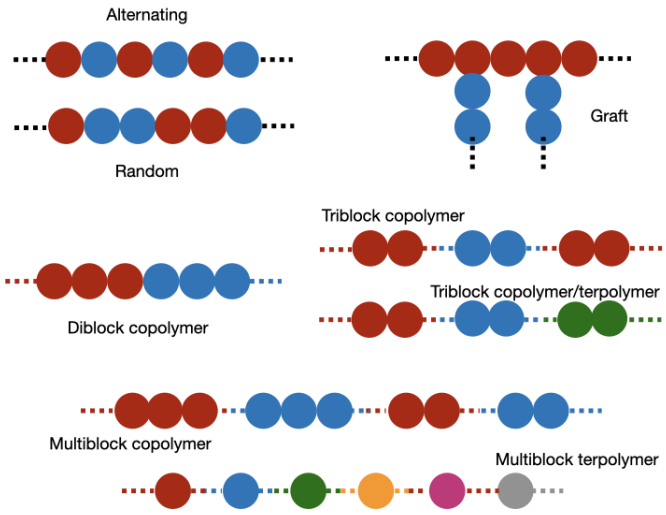

Figure 2: Types of copolymer and terpolymer.

Over the last few decades, many theoretical models have been developed to understand polymer physics. So far, the simplest model is the ideal chain model, which describes the polymer as a random walk and ignores any kind of interaction between monomers.

2.1.1 *Ideal Chain Model*

Consider a chain of many monomers, with $\mathbf{A}_0$ being the position of zeroth monomer and $\mathbf{A}_N$ is the position of the N^{th} monomer. There are total $(N+1)$ backbone monomers, and bond $\mathbf{r}_i$ is the distance between any two consecutive monomers, say between i^{th} and $(i+1)^{th}$ monomer. The chain is considered ideal if there is no interaction between any two monomers of the polymer chain. The end-to-end vector (shown in Figure 3) of such a chain is the sum of all N bond vectors

$$\mathbf{R}_N = \sum_{i=1}^{N} \mathbf{r}_i \,. \tag{1}$$

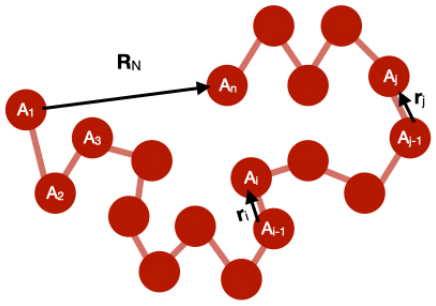

Figure 3: Ideal chain conformation showing end-to-end distance.

Due to different bond vectors, individual chains have different end-to-end vectors. The average end-to-end vectors for an isotropic chain with N monomers is zero. However, the mean square end-to-end distance has a non-zero value. Hence, it is valuable to talk about the average property of this distribution.

$$\langle R^2 \rangle = \langle \mathbf{R}_N{}^2 \rangle = \langle \mathbf{R}_N \cdot \mathbf{R}_N \rangle = \left\langle \left(\sum_{i=1}^{N} \mathbf{r}_i \right) \cdot \left(\sum_{j=1}^{N} \mathbf{r}_j \right) \right\rangle = \sum_{i=1}^{N} \sum_{j=1}^{N} \langle \mathbf{r}_i \cdot \mathbf{r}_j \rangle \,. \tag{2}$$

For identical length of the bond vectors *i.e.*, $|\,\mathbf{r}_i\,| = |\,\mathbf{r}_j\,| = l$, Equation 2 becomes

$$\left\langle R^2 \right\rangle = l^2 \sum_{i=1}^{N} \sum_{j=1}^{N} \left\langle \cos\theta_{ij} \right\rangle , \tag{3}$$

where θ_{ij} is the angle between bond vectors $\mathbf{r}_i$ and $\mathbf{r}_j$. $\left\langle \cos\theta_{ij} \right\rangle$ becomes zero for $i \neq j$ and one otherwise if the bonds are not correlated. If the bonds are correlated then, the mean square end-to-end distance is

$$\left\langle R^2 \right\rangle = Nl^2 . \tag{4}$$

Apart from mean square end-to-end distance, another commonly used measure of chain dimension is radius of gyration (R_g) [30]. The square of the radius of gyration (${R_g}^2$) is the second moment around the center of mass of the chain. ${R_g}^2$ is defined as the mean square of the distance between the monomers and the center of mass of the chain, which is given as

$${R_g}^2 = \left\langle \frac{1}{(N+1)} \sum_{i=1}^{N} (\mathbf{A}_i - \mathbf{R}_{cm})^2 \right\rangle , \tag{5}$$

where R_{cm} is the position vector of the center of mass of the polymer and is defined as the average of all monomer position vectors [31].

There are multiple ways to calculate ${R_g}^2$, for example it can be computed from the summation of the principal moment of gyration tensor. In that case it is given as

$${R_g}^2 = \frac{1}{2} \left\langle \frac{1}{(N+1)^2} \sum_{i,j=0}^{N} (\mathbf{A}_i - \mathbf{A}_j)^2 \right\rangle . \tag{6}$$

Experimentally gyration radius can be determined using techniques like light scattering, small-angle x-ray, and neutron scattering.

Another way of describing the size of a polymer is through its hydrodynamic radius, R_h [32] which is defined as a radius of the equivalent hard-sphere diffusing at the same rate as the polymer.

$$\left\langle \frac{1}{R_h} \right\rangle = \frac{1}{2N^2} \sum_{i \neq j} \left\langle \frac{1}{\mathbf{A_{ij}}} \right\rangle . \tag{7}$$

The ratio of the radius of gyration and hydrodynamic radius provides some information regarding the conformation of the macromolecule. In case of a globular polymer the value of R_h and R_g are similar [33]. Theoretical hydrodynamic radius came from the study of dynamic properties of polymers in a solvent, and generally, it is similar in magnitude to the gyration radius.

2.1.2 *Real Chain Models*

As stated above, the ideal chain model ignores inter-molecular steric or energetic interaction between monomers for simplicity. For more realistic modeling, we should account for the fact that monomers occupy real volumes and interact with other monomers of the chain and with the solvent molecules in the system. Polymer chain models which consider inter-molecular and solvent interactions are termed real polymer chains. Here, the concept of excluded volume of a monomer and Flory's theory of real polymer chains will be discussed.

To understand the monomer interactions, we need to estimate the number of monomer-monomer interactions within a single polymer coil. By knowing the probability for a given monomer to experience another monomer with many bonds away from it and the polymer, we can calculate the interactions. A mean-field estimate can approximate this by replacing the ideal chain in d-dimensional space with an ideal gas of N monomers located in a coil's pervaded volume $\sim R^d$. In this mean-field approximation, the overlap volume fraction (ϕ^*) of a chain inside its pervaded volume gives the probability of a monomer interacting with another monomer. The overlap volume fraction is

$$\phi^* \approx b^d \frac{N}{R^d} , \tag{8}$$

where, b^d is the monomer volume and N/R^d is the number density of monomers in the pervaded volume. Assuming an ideal chain for the time being, which obeys Gaussian statistics in any dimension with $R = bN^{1/2}$. Hence, the overlap volume fraction can be rewritten as

$$\phi^* \approx b^d \frac{N}{(bN^{1/2})^d} \approx N^{1-d/2}. \tag{9}$$

In a three-dimensional system the overlap volume fraction for ideal chain scales as

$$\phi^* \approx N^{-1/2}, \text{ for } d = 3 \text{ and } N \gg 1. \tag{10}$$

In a polymer chain, the number of monomer-monomer interaction is the product of the number of monomers in the chain and the overlap concentration *i.e.*, the volume fraction of chain in the pervaded volume

$$N\phi^* \approx N^{2-d/2}. \tag{11}$$

For a three-dimensional system, this relation will become

$$N\phi^* \approx N^{1/2}, \text{ for } d = 3 \text{ and } N \gg 1. \tag{12}$$

Since the overlap concentration is significant for a three-dimensional system, it is important to account for these interactions along the polymer chain and to understand how the energy arising from these contacts affects the conformation of a real polymer chain. The effective interaction between a pair of monomers depends on the interaction of a monomer with other monomers and its surrounding molecules. For example, in a poor solvent, the monomers prefer to stay close to each other to minimize contact with the surrounding molecules. Whereas in the case of good solvent,

monomers prefer to stay in contact with the solvent molecules. In the case of zero net interaction, it does not matter whether the monomers contact other monomers or with the surrounding molecule. Therefore, in order to quantify monomer-monomer interactions, we need to understand the excluded volume and the Mayer f-function, which we will discuss below.

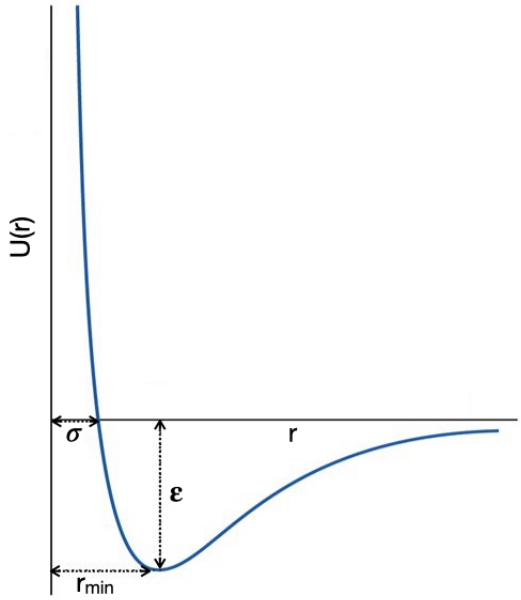

Figure 4: Effective interaction potential between two monomers.

By definition, excluded volume is the volume of a molecule inaccessible by other molecules in the system. As a result of the excluded volume, the polymer coils are typically more swollen than they would be in the absence of excluded volume. To calculate the excluded volume, let us consider the cost of energy $U(r)$ required to bring two monomers from infinite distance to a distance of r. A standard profile of this function $(U(r))$ is given in Figure 4, which shows a hard-core repulsive barrier corresponding to the energy cost of repulsion between two overlapping monomers and an attractive well corresponding to the energy difference between the two monomers as they like each other more than the solvent molecules.

Mathematically, the interaction between a pair of a neutral particle is

$$U(r) = 4\epsilon\left[\left(\frac{\sigma}{r}\right)^{12} - \left(\frac{\sigma}{r}\right)^{6}\right], \tag{13}$$

where ϵ is the depth of the potential well and σ is the distance at which the potential is zero. This expression (Equation 13) was first proposed by John Lennard-Jones, so it is well known as Lennard-Jones potential or 12-6 potential or 6-12 potential as well.

On the contrary, when we have monomers that are chemically identical to the solvent, and there is no energy difference between their interactions, then the $U(r)$ will have only the hard-core repulsion (Figure 5). However, if monomers like one another less than the solvent molecules, then there will be extra repulsion and no attractive well in $U(r)$.

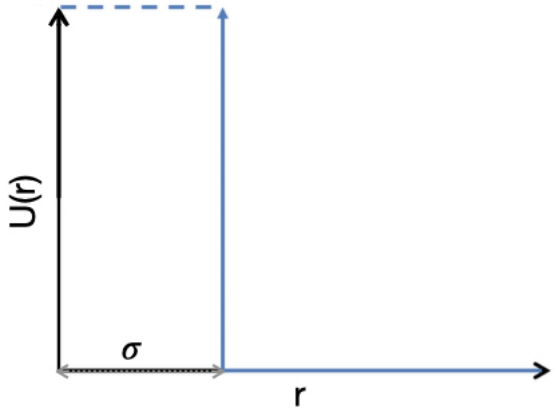

Figure 5: Effective hard-core potential [34].

The probability of finding a monomer pair with a separation distance of r in a solvent is proportional to $\exp[-U(r)/k_BT]$, where k_B is the Boltzmann's constant and T is the temperature. In this case, the probability is zero when $r < \sigma$ and for $r > \sigma$ it is more likely to find monomers at these distances, and the Boltzmann factor is one in the absence of long-range interactions.

The Mayer f-function $f(r)$ [35] is described as the difference between the Boltzmann factor for two monomers at a distance r and at infinite distance

$$f(r) = \exp[-U(r)/k_BT] - 1\,. \tag{14}$$

Due to the hard-core repulsion the energy is large for $r < \sigma$, the likelihood of finding monomers at this distance is less, making the Mayer f-function negative, whereas

for $r > \sigma$, *i.e.*, for an attractive well which enhances the probability of finding a monomer, the Mayer f-function is positive. The excluded volume ν is given by the negative integral of the Mayer f-function over the whole space

$$\nu = -\int f(r) d^3r = \int (1 - \exp[-U(r)/k_B T]) d^3r \,. \tag{15}$$

The behavior of Mayer f-function influences the excluded volume effect, and a net attraction has $\nu < 0$ and a net repulsion has $\nu > 0$. For a given real polymer chain, the value of ν corresponds to the solvent condition, where $\nu > 0$ indicates a good solvent as the Mayer f-function is negative, while for $\nu < 0$, the solvent is a bad solvent. There is a special case where the contribution of repulsion and attraction balances out, which is called the theta solvent (or theta temperature).

The most widespread model for a real chain in a good solvent that determines the energetic and entropic contribution to the free energy is the Flory theory, which works on the assumption that the monomers have no correlation between them and are distributed within the volume R^3, where R is the swollen size of the polymer, $R > R_0 = bN^{1/2}$. The probability of finding a monomer in the excluded volume of a given monomer is $\nu N/R^3$, and the energy cost from being excluded is $k_B T$ per exclusion, *i.e.*, $k_B T \nu N/R^3$. For N number of monomers, this energy will be multiplied to N

$$F_{int} \approx k_B T \nu \frac{N^2}{R^3} \,. \tag{16}$$

The entropic contribution estimated by Flory to the free energy of a real chain is the energy needed to stretch an ideal chain to its end-to-end distance

$$F_{ext} \approx k_B T \frac{R^2}{Nb^2} \,. \tag{17}$$

Now in the Flory approximation, the total energy will become

$$F = F_{int} + F_{ext} \approx k_B T\left(\nu\frac{N^2}{R^3} + \frac{R^2}{Nb^2}\right). \tag{18}$$

The optimum size of a real chain in Flory theory ($R = R_F$) is calculated from the minimum of the free energy of a chain, i.e. $\partial F/\partial R = 0$, and is given by

$$R_F \approx \nu^{1/5} b^{2/5} N^{3/5}. \tag{19}$$

Thus, the size of a long real chain is much bigger than the ideal chain with the same number of monomers, as given in swelling ratio (R_F/R)

$$\frac{R_F}{bN^{1/2}} \approx \left(\frac{\nu}{b^3}N^{1/2}\right)^{1/5}. \tag{20}$$

For $F_{int} < k_B T$, chain does not swell and conformation of the chain remains ideal. Excluded volume only swells the chain, when there is sufficiently large chain interaction parameter

$$z = \frac{\nu}{b^3}N^{1/2}. \tag{21}$$

This prediction of Flory theory is in good agreement with experiments [36] as well as computer simulations [37]. Flory theory gave the universal power-law dependence of polymer size R on the number of monomers N (Equation 19). The estimated scaling exponent from Flory theory is $\nu = 3/5$ for a swollen linear polymer and $\nu = 1/2$ for an ideal polymer. Ideal chains are usually random walks with no correlation, and the real chains are self-avoiding walks (a random walk with monomer not visiting the same site again).

2.1.3 *Thermodynamics of Binary Mixtures*

To study the phase behavior of polymers, we need to understand the thermodynamics of mixing polymer solutions and polymer melts. Polymer solutions can be either homogeneous or heterogeneous. In homogeneous mixtures, the components are mixed at the molecular level, while heterogeneous mixtures consist of several phases and are non-uniform. The equilibrium state of any mixture is determined by the composition dependence of the entropy and energy of mixing. As a rule of thumb, entropy always favors mixing, whereas energetic interactions inhibit mixing. For simplicity let us consider a binary mixture of two species A and B on a lattice. Considering there is no volume change during mixing and the formed mixture is homogeneous, the volume fractions of A (ϕ_A) and B (ϕ_B) in the binary mixture are

$$\phi_A = \frac{V_A}{V_A + V_B} \text{ and } \phi_B = \frac{V_B}{V_A + V_B} = 1 - \phi_A \,, \tag{22}$$

where V_A and V_B are the volumes of species A and B, respectively, and the total volume of the mixture is $V_A + V_B$. The entropy S is defined as the product of the Boltzmann constant k_B and the natural logarithm of the number of states Ω

$$S = k_B \ln \Omega \,. \tag{23}$$

The number of states for species A (Ω_A) before mixing is the number of lattice sites it occupies. Hence, the change of entropy for species A after mixing will become

$$\Delta S_A = k_B \ln \Omega_{AB} - k_B \ln \Omega_A = -k_B \ln \phi_A, \; \Omega_{AB} = n \text{ and } \Omega_A = n\phi_A \,, \tag{24}$$

where n is the total number of lattice sites available after mixing. From Equation 24, we see that the entropy change is always positive as ϕ_A is always less than 1. The total entropy is the sum of entropy contribution of each molecule

$$\Delta S_{mix} = n_A \Delta S_A + n_B \Delta S_B \,, \tag{25}$$

where $n_A = n\phi_A/N_A$, $n_B = n\phi_B/N_B$, N_A and N_B are the lattice sites for species A and B before mixing.

The entropy of mixing for a polymer solution $\Delta \bar{S}_{mix}$ is an intrinsic thermodynamic quantity which has $N_A = N$ and $N_B = 1$, and is given by entropy per lattice site

$$\Delta \bar{S}_{mix} = -k_B \Big[\frac{\phi_A}{N} \ln \phi_A + \phi_B \ln \phi_B \Big] . \tag{26}$$

The entropy of mixing is always positive, making an ideal mixture to be always homogeneous. For an ideal mixture the free energy per lattice site is entropic only, and is given by

$$\Delta \bar{F}_{mix} = -T\Delta \bar{S}_{mix} = k_B T \Big[\frac{\phi}{N_A} \ln \phi + \frac{1-\phi}{N_B} \ln(1-\phi) \Big] . \tag{27}$$

The entropy of mixing is small for polymer solutions, especially at low polymer concentrations. Hence, the change in enthalpy of mixing dictates the miscibility for non-ideal polymers. Since the energetic interaction between species can be positive or negative, we need to find the minimum Gibbs free energy to estimate the equilibrium state. Experiments are conducted mostly at constant pressure, but the Flory-Huggins theory implicitly assumes a constant number of particles (lattice sites). The change in Helmholtz free energy will be considered for energetic interactions. In the mixture, the difference of interaction is characterized by the Flory-interaction parameter χ

$$\chi \equiv \frac{z}{2} \frac{(2u_{AB} - u_{AA} - u_{BB})}{k_B T} , \tag{28}$$

where u_{AA}, u_{BB} and u_{AB} are the three pairwise interaction energies in a binary mixture and z is the coordination number of the lattice (for example $z = 6$ for a simple cubic lattice in three dimensions). The parameter χ is a dimensionless quantity which computes the strength of pairwise interaction energies between species in a mixture. This definition gives the energy of mixing per lattice site

$$\Delta\bar{U}_{mix} = \chi\phi(1-\phi)k_BT\,. \tag{29}$$

Now, combining with Equation 26 for the entropy of mixing we will get Helmholtz free energy of mixing per lattice site, which is a mean field description of all binary mixture and entropy of mixing

$$\Delta\bar{F}_{mix} = \Delta\bar{U}_{mix} - T\Delta\bar{S}_{mix} = k_BT\Big[\frac{\phi}{N_A}\ln\phi + \frac{(1-\phi)}{N_B}\ln(1-\phi) + \chi\phi(1-\phi)\Big]\,. \tag{30}$$

Equation 30 is called the Flory-Huggins equation, as it was calculated by Huggins first and later derived by Flory independently. For a polymer solution with $N_A = N$ and $N_B = 1$, the Flory-Huggins equation will become

$$\Delta\bar{F}_{mix} = k_BT\Big[\frac{\phi}{N}\ln\phi + (1-\phi)\ln(1-\phi) + \chi\phi(1-\phi)\Big]\,. \tag{31}$$

Here, the first two terms are of entropic origin, while the third term has an energetic origin. When the last term in Equation 31 is positive, the mixing is unfavorable, and when it is negative, it promotes mixing, and the mixture is called the ideal mixture while it is zero. We can estimate the Flory parameter for a mixture of non-polar species by using the Hildebrand and Scott relation, which is based on the solubility parameter [38] of a given species and is given as

$$\chi \approx \frac{v_o}{k_B T}(\delta_A - \delta_B)^2 , \tag{32}$$

here, δ_A and δ_B are the solubility parameters for species A and B, and v_o is the volume per site. Flory-Huggins theory works based on the assumption that the volume of the system does not change on mixing. However, in most real polymer blends, the volume changes, which leads to the addition of a temperature-independent constant in the expression of the Flory interaction parameter

$$\chi(T) \cong A + \frac{B}{T} . \tag{33}$$

Here, the temperature-independent part A is referred to as the entropic part, and the temperature-dependent part B/T is called the enthalpic part. The Flory-Huggins equation is very important in polymer solutions as it contains important thermodynamic information required in order to estimate the equilibrium phase behavior of a mixture.

The dissolution of a polymer in a solvent is similar to a low-molecular-weight solute, where solvation lowers the free energy. The major factors defining the properties of a polymer solution are the temperature of the solution and the number of solute particles present in the solution. The phase diagram for a polymer solution is given in Figure 6,

Here, we can see that the θ temperature separates the curve into two halves, with the bottom being the poor solvent region and the top one being the good solvent region. At θ temperature, the solvent is called theta solvent, and the real chain behaves as an ideal chain at all concentrations, and in this case, the value of $\chi = 1/2$ and the excluded volume is zero. At low concentrations, polymers are far apart and exist as isolated coils, and the concentration increases going from left to right in Figure 6. At $T = \theta$ the concentration is equal to the concentration in pervaded volume, and this is the overlap concentration of θ solvent,

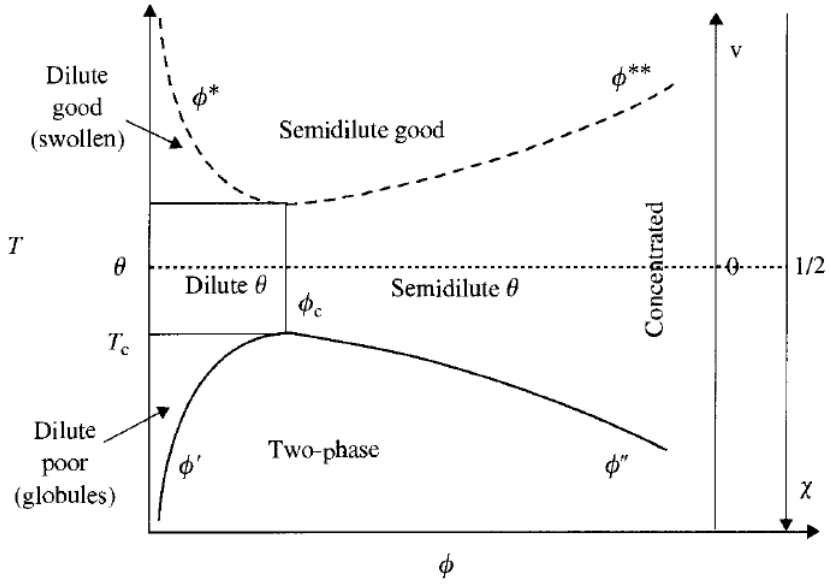

Figure 6: Phase diagram of a polymer solution [39].

$$\phi_\theta{}^* = \frac{1}{\sqrt{N}}\,. \tag{34}$$

2.2 POLYMER DYNAMICS

The flow behavior of polymer solution is interesting due to the numerous conformational degrees of freedom of polymer chains. The flow properties of such polymers microscopically arise from the entanglement of the chains [39–41]. A polymer chain moving in a solvent experiences collisions (each monomer) with the solvent molecules. Apart from frictional forces, it experiences random forces that result in the chain's Brownian motion, which is defined as an uncontrolled motion of particles in a fluid due to the constant collision with other molecules [42].

In polymers, Brownian motion dominates time-dependent phenomenon like diffusion and viscosity and can be described by two equations called Smoluchowski equation and Langevin equation. Langevin equation [43] describes the time evaluation of Brownian particles

$$m\frac{dv}{dt} = -\zeta \mathbf{v} + \eta(t)\,, \tag{35}$$

which contains the frictional force term, ζ being the coefficient of friction and random force term $\eta(t)$.

Smoluchowski equation [44] explains the diffusive motion of a Brownian particle in an external potential and is derived from generalization of diffusion equation

$$\zeta\frac{\delta\rho}{\delta t} = \nabla\cdot(\frac{k_B T}{m}\nabla\rho + \rho\nabla\phi_{ext})\,, \tag{36}$$

where ϕ_{ext} is an external potential and ρ is the density. Here, we will discuss one-dimensional diffusion of a single colloidal particle in solution. Diffusion is described by Fick's law which states that, the flux $j(x,t)$ is proportional to the spatial gradient of concentration $c(x,t)$ when the concentration is non-uniform, and is given a

$$j(x,t) = -D\frac{\partial c}{\partial x}\,, \tag{37}$$

where D is a proportionality constant and is called diffusion constant. The flux is due to the random motion of particles, which leads to the flow of such particles from a high concentration region to a low concentration region. In case of an external potential, Fick's law will be modified and the potential exerts a force which is

$$\mathbf{f} = -\frac{\partial \mathbf{U}}{\partial x}\,. \tag{38}$$

Due to this force, the particle will be pulled in through the liquid, and it will achieve a constant velocity in the same direction as the applied force. The coefficient which relates the force to the velocity is called friction coefficient ζ,

$$\mathbf{f} = \zeta \mathbf{v} \,. \tag{39}$$

Since the force acting on the particle results in a constant velocity, there has to be an equal and opposite force acting on the particle, known as viscous drag.

The friction coefficient is related to the diffusion coefficient through Einstein relation

$$D = \frac{k_B T}{\zeta} \,. \tag{40}$$

This relation is obtained from the fluctuation dissipation theorem [45, 46]. Both the Brownian diffusion and frictional force are caused by the same random force resulting in the friction force. Hence, it is informative to calculate the time required by a particle to diffuse a distance of its size R, which is proportional to the friction coefficient (Equation 41),

$$\tau \approx \frac{R^2}{D} \approx \frac{R^2 \zeta}{k_B T} \,. \tag{41}$$

However, the mechanical properties of a liquid are different from solids, where the stress depends only on the deformation rate for the liquids, not on the total deformation. This deformation rate is given as shear rate $\dot{\gamma} = d\gamma/dt$. The shear rate, according to Newton's law of viscosity, is related to the stress as

$$\sigma = \eta \dot{\gamma} \,, \tag{42}$$

where, the proportionality constant is the dynamic viscosity of the liquid. The friction coefficient is the ratio of force and velocity (Equation 39) which has units $kg\,s^{-1}$. The viscosity has the units $kg\,m^{-1}\,s^{-1}$, as it is the ratio of stress and shear rate. So, the dimensionally correct relation between the friction coefficient and viscosity is,

$$\zeta \approx \eta R\,. \tag{43}$$

This relation (Equation 43) was derived by Stokes in 1851, also known as Stokes' law, for the frictional force exerted on a spherical object in a viscous liquid with a numerical prefactor of 6π which results in, $\zeta = 6\pi\eta R$. The Stokes' law is derived by solving the Navier-Stokes equations (will be discussed in a later section) for a small Reynolds number.

By combining Stokes' law with the Einstein relation (Equation 40), the diffusion coefficient of a spherical particle in a liquid can be calculated by the so-called Stokes-Einstein relation

$$D = \frac{k_B T}{6\pi\eta R}\,. \tag{44}$$

Hence, this will help determine the coil size from the measured diffusion coefficient (dynamic light scattering experiments), and the obtained size is the hydrodynamic radius of the coil.

$$R_h = \frac{k_B T}{6\pi\eta D}\,. \tag{45}$$

Until now, we discussed the Brownian motion of a single particle in a fluid. Let us now consider a situation where we have multiple Brownian particles suspended in liquid and interacting with each other. In this case, to calculate the Smoluchowski equation, we need to obtain the mobility matrix, which depends on the positions and the forces exerted on each particle. Here, the velocity is dependent on the force acting on the surrounding particles because the motion of the fluid is caused due to the force acting on one particle affecting the velocity of every particle. This special interaction coming from the motion of the fluid is called hydrodynamic interaction.

The hydrodynamic interaction usually assumes the fluid to be incompressible and the inertial force of the fluid to be negligibly small.

To understand the behavior of polymers in solution, we need to calculate the velocity vector field, which is perturbed due to the presence of polymeric particles in the fluid. The equation used to calculate the velocities is the Navier-Stokes equation developed by Clade-Louis Navier and George Gabriel Stokes in 1822. This equation is derived from the continuity equation, and basic conservation is applied to the fluid properties. For deriving the Navier-Stokes equation, we need to derive the continuity equation first, which is for the conserved quantities and then the conservation of mass and momentum. The general form of a continuity equation is

$$\frac{dL}{dt} + \nabla \cdot (L\mathbf{v}) + Q = 0\,, \tag{46}$$

where L denotes the change of an intensive property and Q is the energy source. If we apply this continuity equation to density with no source or sink of mass $(Q = 0)$, the Equation 46 will become,

$$\frac{d\rho}{dt} + \nabla \cdot (\rho\mathbf{v}) = 0\,. \tag{47}$$

This euqation 47 is called the conservation of mass. For an incompressible fluid the density is constant so the conservation of mass equation will be simplified to $\nabla \cdot \mathbf{v} = 0$. The equation for conservation of momentum is

$$\rho\frac{D\mathbf{v}}{Dt} = \mathbf{b},\ \frac{D\mathbf{v}}{Dt} = \frac{\partial \mathbf{v}}{\partial t} + \frac{\partial \mathbf{v}}{\partial x}\frac{\partial x}{\partial t} + \frac{\partial \mathbf{v}}{\partial y}\frac{\partial y}{\partial t} + \frac{\partial \mathbf{v}}{\partial z}\frac{\partial z}{\partial t}\,, \tag{48}$$

where $\mathbf{b}$ is the body force. Since the body force on the fluid parcel is assumed to be due to fluid stresses (σ) and external force $(\mathbf{f})$, it is written as, $\mathbf{b} = \nabla\sigma + \mathbf{f}$. By setting the stress tensor to a sum of viscosity (τ) term and pressure term, the equation will look like

$$\rho \frac{D\mathbf{v}}{Dt} = -\nabla p + \nabla \cdot \tau + \mathbf{f}, \tag{49}$$

where p is the pressure and τ is the deviatoric stress tensor, which has order two. Since, the Navier-Stokes equation is specific to fluids, for a Newtonian fluid it can be rewritten as

$$\rho \frac{D\mathbf{v}}{Dt} = -\nabla p + \eta \nabla^2 \mathbf{v} + \mathbf{f}, \tag{50}$$

here η is the viscosity.

The term 'viscosity' is widely used and its meaning can vary. For example, the ratio of solution viscosity η to the solvent viscosity η_s is called relative viscosity η_r, which is a dimensionless quantity,

$$\eta_r = \frac{\eta}{\eta_s}. \tag{51}$$

Now, the difference of the relative viscosity from unity is called specific viscosity η_{sp} and given as

$$\eta_{sp} = \eta_r - 1 = \frac{\eta - \eta_s}{\eta_s}. \tag{52}$$

The ratio of specific viscosity to polymer concentration is called reduced viscosity. At very low polymer concentration, this viscosity becomes an important material property called intrinsic viscosity, which is nothing but the slope of specific viscosity as a function of concentration.

As mentioned before, polymer solutions have interesting mechanical properties such as viscoelasticity. The term viscoelasticity is derived from viscosity and elasticity, which reflects that a polymer solution has both viscosity from the solvent part and

elasticity from polymers. In order to understand the dynamics of a polymer solution, we need to determine its viscoelastic properties. The velocity in shear flow in one direction is given by

$$v_x(r,t) = \dot{\gamma}(t) r_y,\ v_y = v_z = 0\,, \tag{53}$$

where $\dot{\gamma}(t)$ is the shear rate. The shear stress is dependent on shear rate if it is small and can be written as

$$\sigma_{xy}(t) = \int_{-\infty}^{t} dt' G(t-t')\dot{\gamma}(t')\,, \tag{54}$$

with G(t) being the shear relaxation modulus. For dilute polymer solution the solvent has significant effect, due to which the shear stress is rewritten including the viscosity term as,

$$\sigma_{xy}(t) = \eta_s \dot{\gamma}(t) + \int_{-\infty}^{t} dt' G(t-t')\dot{\gamma}(t')\,. \tag{55}$$

Now, in order to calculate the dynamic properties of a polymeric system, we need to model the system. The first and simplest model considered for deriving the properties of the polymeric system is the Rouse model.

2.2.1 *Rouse and Zimm Model*

The Rouse model also uses the Gaussian chain model; however, it is the first successful model to explain polymer dynamics. Let us consider a chain with N beads and a mean square size of R^2, which interact with each other only through connecting springs. Each bead has its friction coefficient ζ. Hence the total friction is the sum of friction experienced by each bead, given as,

$$\zeta_R = N\zeta\,. \tag{56}$$

The diffusion coefficient for the Rouse model is obtained from the Einstein equation,

$$D_R = \frac{k_B T}{\zeta_R} = \frac{k_B T}{N\zeta}\,. \tag{57}$$

The time taken by a polymer to diffuse a distance equivalent to its own characteristic length is known as a Rouse time, τ_R

$$\tau_R \approx \frac{R^2}{D_R} \approx \frac{R^2}{k_B T/N\zeta} \approx \frac{\zeta}{k_B T} N R^2\,. \tag{58}$$

The relaxation time for the motion of an individual bead is given in terms of the Kuhn length b, *i.e.*, $\tau_0 \approx \zeta b^2/k_B T$. The relaxation times τ_0 and τ_R can be rewritten in terms of viscosity as

$$\tau_o \approx \frac{\eta_s b^3}{k_B T},\ \tau_R \approx \frac{\eta_s b^3}{k_B T} N^2\,. \tag{59}$$

In case of time scales smaller than τ_o the polymers behaves elastically, while for time scales greater than τ_R the motion is diffusive. Furthermore for time scales between $\tau_o < t < \tau_R$, the chains exhibits viscoelasticity. The problem with the Rouse model is that it does not take into account hydrodynamic interactions. When the polymer flows in a solvent, it drags some of the surrounding fluid particles along with it. The force acting by the polymer on solvent particles gets smaller with increasing distance between the polymer and the solvent particle, but this interaction is typically rather long-ranged. The Rouse model only considers the interaction between the beads through the spring they are connected with. Although this model

is inappropriate for dilute polymer solutions, it works rather well for describing the dynamics in polymer melts, where hydrodynamics are screened.

The Zimm model considers the hydrodynamic iteration between the polymer beads. Now the friction coefficient is given by stokes' law

$$\zeta_z = 6\pi\eta_s R_h \,. \tag{60}$$

And the diffusion coefficient of the center of mass of polymers is given by

$$D_Z = \frac{D_o}{N} + \frac{k_B T}{6\pi\eta_s R_h} \,, \tag{61}$$

where the first term is due to the random Brownian motion of the N constituent beads with diffusivity D_o, and the second term comes from the hydrodynamic interactions between them.

For a polymer in dilute solution the diffusion coefficient can be calculated by Stokes-Einstein relation. The Zimm time is now given as

$$\tau_Z \approx \frac{R^2}{D_Z} \approx \frac{\eta_s}{k_B T} R^3 \,. \tag{62}$$

The Zimm time is proportional to the pervaded volume of the chain and has a weaker dependence on chain length compared to the Rouse time. Comparison of Zimm time and Rouse time suggests that Zimm time is shorter than the Rouse time in dilute solution.

2.3 POLYMER DYNAMICS IN CONFINEMENT

The dynamics of a polymer solution in confined geometries is interesting to study as it is important for a wide range of applications from oil recovery to coating process to analytic and preparatory separation techniques for macromolecules. Recent advances

in microfluidic and nanofluidic devices have enabled the application in manipulating and characterizing genomics DNA [47–51]. The effects of confinement are noticeable when the size of the polymer is either same or larger than the length scale of the confinement. Generally, the presence of confining walls breaks the translational invariance of the polymeric system so that the situations like simple shear, which will not generate in the homogeneous polymer concentration, but, in bulk solution, may lead to the concentration gradient in confinement. In the presence of an external force, the restrictiveness arising from the confinement leads to a velocity gradient, which changes the chain's conformation and dynamics in the flow. The boundary conditions that restrict the solvent also play a role in affecting the polymer dynamics, relaxation time, diffusivity, and transport process in flow. In the absence of flow, due to steric repulsion between the polymer coil and confinement, a depletion layer occur near the confining walls, which is of the size of gyration radius, R_g [52–54]. Whereas in the case of flow, either shear or pressure-driven, the alignment of polymer coils takes place along the flow direction due to the shear rate, which stretches the polymer and reduces its configurational entropy. Also, migration of polymer chains towards or away from the walls is observed [55]. For a polymer solution in a simple shear or pressure-driven flow in which the flow geometry is much larger than the polymer size, the polymer migrates towards the channel center-line. The main driving force for the migration of polymers is the hydrodynamic drift from the confining wall, driven by the shear rate [56, 57]. In the absence of hydrodynamic interactions, the migration of polymers is towards the channel walls, confirmed by simulation [58]. Hence, it is very much clear that hydrodynamic interactions play a vital role in polymer solution dynamics. However, because of the position-dependent conformations and mobility of polymeric coils, they experience a force away from the channel center called the inertial lift force. Hence, the equilibrium position of a polymer chain in confinement is governed by the balance of these two forces (see Figure 7).

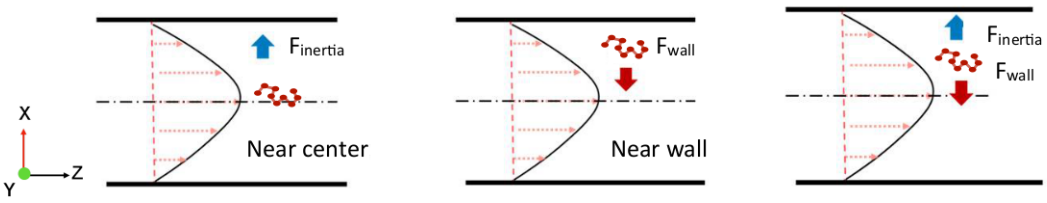

Figure 7: Forces acting on the linear chain in a Poiseuille flow (pressure driven flow) in a slit channel.

2.4 PHASE BEHAVIOR OF BLOCK POLYMERS

The possibility to obtain different monomer combination and block architecture with a wide range of polymerization techniques [59] has led to the interesting study of self-assembly of polymers, especially the block copolymers. The inherent immiscibility of unlike blocks leads to the formation of different nanostructures in the range of $10 - 100\,\text{nm}$ [60], that occurs either in bulk or in selective solvents [61, 62]. These nanostructures have applications in various fields, like, biomedicine [63], energy applications [64] and lithography [65] or as emulsifier and microsurfactants. Additionally, the morphologies obtained from the self-assembled structures of block copolymers have been rapidly expanding their applications in the fields of drug delivery [66–69], advanced materials like elastomers, patterning, and porous materials, *etc.* [70].

Theoretical development in block copolymers led to remarkably predictive theories accounting for the domain shapes, dimensions, connectivity, and ordered symmetry of many types of block copolymers.

The factors responsible for tuning the morphologies of self-assembled nanostructures from block copolymers are primarily the Flory-Huggins interaction parameter (χ), the degree of polymerization (N), and the volume fractions of the individual blocks (f) [71]. For diblock copolymers, the different possible morphologies are, *e.g.*, spherical micelles, cylindrical, bicontinuous structures, lamellae, and vesicles, which have been revealed experimentally and theoretically [72, 73]. Apart from the factors mentioned above, scientists have found that the macromolecular architecture also plays a key role in the morphology and their long-range ordering [74].

Two competing factors responsible for forming different self-assembled morphologies of block copolymers are the interfacial energies between the two blocks (enthalpy contribution), and the second is the chain stretching (entropic contribution). The phase separation occurs in such a way that the total interfacial energy is minimum. The phase separation in block copolymers leads to chain stretching, away from the A-B interface, and the degree by which a block is stretched depends on the volume fraction of that block. This morphological transition of phases is explained by the well-known cone-column mechanism, which states that if the fraction of one block is small, it prefers to aggregate in a spherical domain, and the other block surrounds it as the corona. As the corona volume fraction decreases, the block-forming corona has to opt for a different morphology in order to decrease the chain stretching (Figure 8). The cone column mechanism is quantified with the help of packing factor $p = v/(a_o l_c)$, where a_o and l_c are the diameter and length of the hydrophobic segment, respectively, and v is the volume.

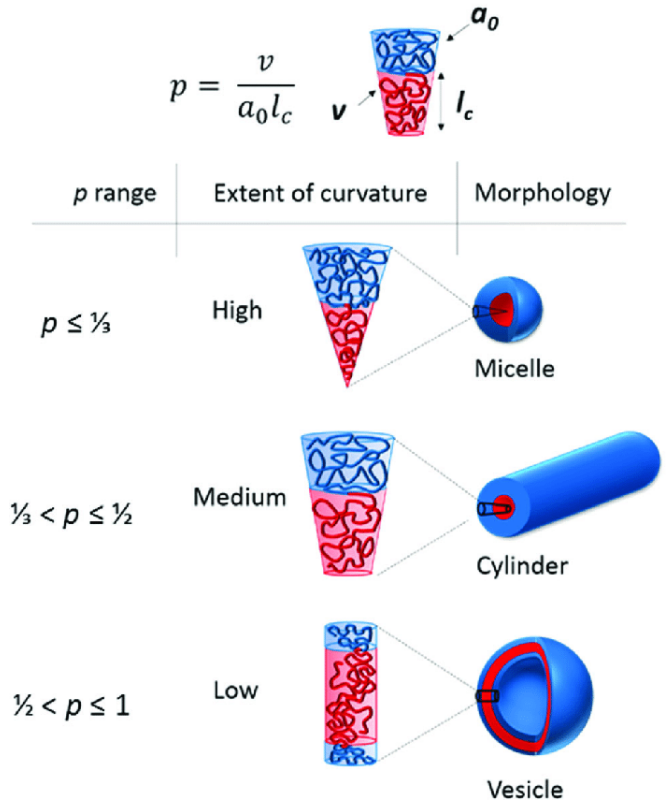

Figure 8: Equilibrium morphologies of AB diblock copolymer in solution explained by cone-column mechanism [75].

As a rule of thumb, for $p < 1/3$ spheres are formed i.e., when $1/3 < p < 1/2$ then cylinders are formed, for $1/2 < p < 1$ flexible lamellae or vesicles are formed, and finally planar lamellae are formed for $p = 1$. Inverted structures can also be observed for $p > 1$, shown in Figure 8 [75].

In thermodynamic control, the morphologies are governed by the composition and/or temperature of the system. In kinetic control, the morphological paths are also relevant, and the aggregate formation depends on the hydrodynamic interaction among the chains as well as the chain dynamics in the hydrophobic domain. In this work, the self-assembly of block polymers is thermodynamically driven *i.e.*, they are in thermodynamic equilibrium.

Among various block copolymers, the most commonly studied ones so far are diblock and triblock polymers.

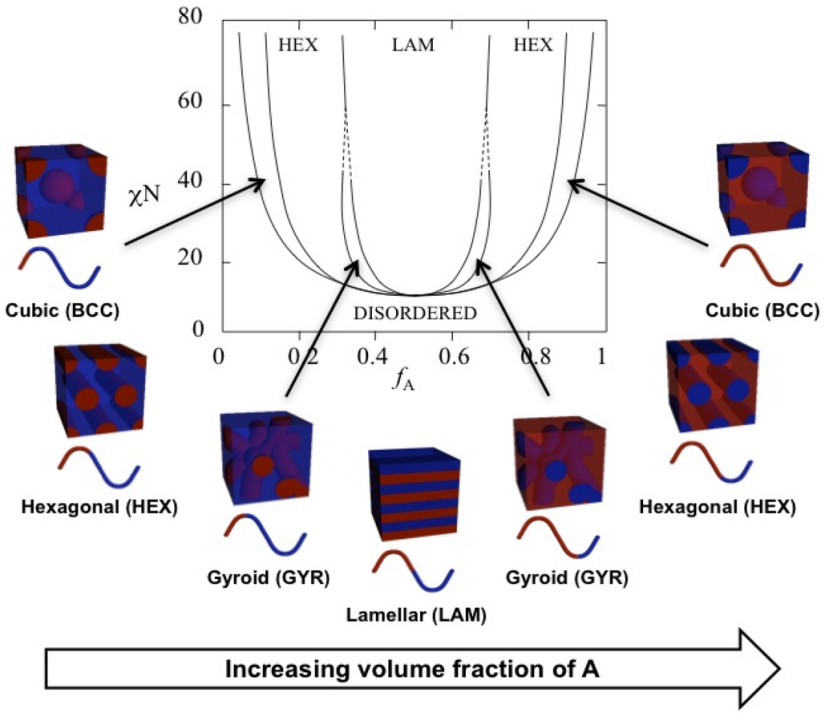

Figure 9: Equilibrium morphologies of AB diblock copolymer in bulk as a function of the volume fraction of the A block, f_A, and the combined Flory-Huggins interaction parameter, χN [71].

Diblock copolymers have been extensively studied in aqueous solutions, as water is applied as a selective solvent for a wide range of materials. A diblock copolymer in water can be amphiphilic, double hydrophobic, or double hydrophilic, depending on the solubility of the blocks in water. The amphiphilic systems are more interesting to

study than the double hydrophobic and double hydrophilic ones due to the different behavior of each block, and they are capable of forming more intriguing structures. Different morphologies ($\approx$ 20) have been observed for such amphiphilic block copolymers in solution, like spherical micelles, rods, vesicles, tubules, "onions", "eggshells" *etc*. The spherical micelles are usually the initial morphology to form when water is added to a diblock system. These initial structures of spherical micelles have been developed considerably further to Janus micelles, multi-compartment micelles *etc*.

A typical diagram for diblock copolymers is shown in Figure 9 as a function of volume fraction (f) of the minority block and the combined Flory-Huggins interaction parameter (χN).

With increasing temperature, χN decreases, and the copolymers undergo an order-to-disorder transition (ODT) and become disordered.

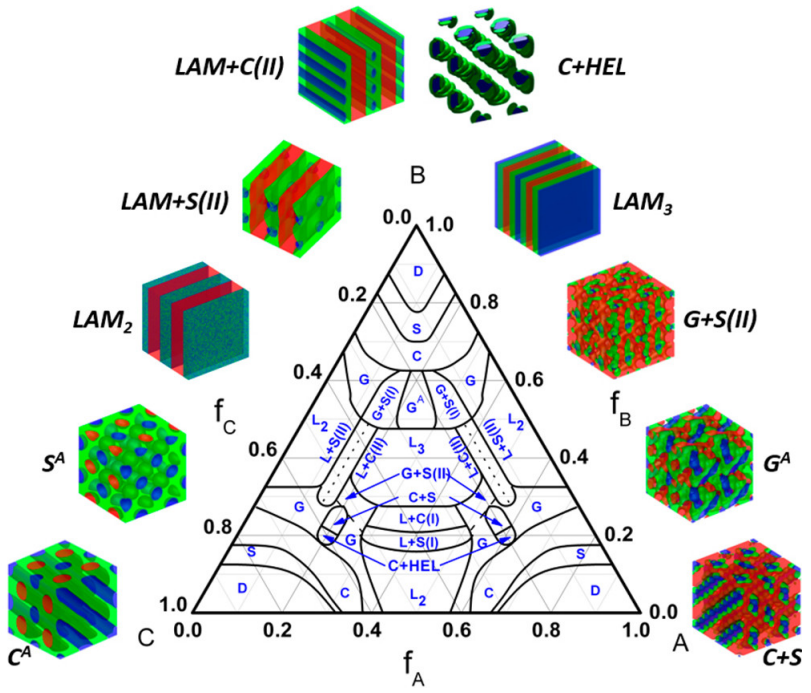

Figure 10: Equilibrium morphologies of ABC triblock copolymer in bulk as a function of volume fraction of A block, f_A, B block, f_B and C block, f_C [76].

The addition of a third block to a diblock is gaining a lot of interest to study in the bulk and solution [77–79], as it allows for different architectural arrangements. Considering the simple case of linear triblock copolymers, three different block arrangements are possible like, A-*b*-B-*b*-C, A-*b*-C-*b*-B and B-*b*-C-*b*-A. The phase behavior of this system in bulk depends on the three different Flory-Huggins parameters and

three volume fractions. Different morphologies have already been reported theoretically and experimentally, and some of the self-assembled structures of the triblock copolymer in bulk are shown in Figure 10.

Going beyond three blocks leads to even more complexity. Though experimentally [25, 68, 77, 78, 80–83] a lot has already been discovered for such block copolymers *etc.*, whereas the computational study of such a system helps to open the door to study the mechanism and transition of one morphology to another, and also in future it will help to study the more complex systems containing four or higher number of blocks.

3

METHODS AND MODELS

Computer simulations are a powerful tool to provide solutions for many statistical mechanics problems that are otherwise hard to solve. Predictions from simulations can be used to understand experimental results that are difficult to access in the laboratory. Hence, computer simulations can act as a bridge between model and theoretical predictions and between model and experimental results [84].

Computer simulations of polymers can be done on different levels as polymers show a hierarchy of length scales and associated time scales. The length and time scales range, for example, from Angstrom and picoseconds, which corresponds to the vibration of atomic bonds, to millimeters and seconds, corresponding to crack propagation in polymers. In polymer modeling, the building blocks are usually atoms, united atoms, monomers, groups of monomers, and chains [85]. That is why we have multiple modeling approaches to model any polymeric system, as shown in Figure 11.

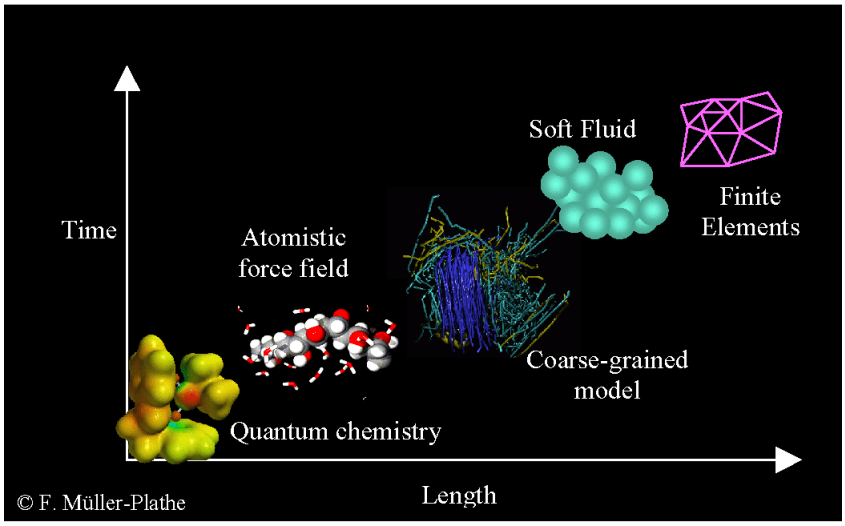

Figure 11: Length scale, time scale and computational method in polymer simulation [85].

Molecular Dynamics (MD) simulations are a useful tool to study systems at an atomistic and molecular scale. In order to study the solvent-mediated hydrodynamic interaction in polymer solutions, mesoscale simulation techniques are mostly used because polymer chains are typically much larger than solvent particles and have slower dynamics. MD simulations retain too many microscopic degrees of freedom, requiring very small time steps to resolve the system. Fine resolution of solvent is unnecessary, and only solvent effect on the solute is relevant. In order to overcome these difficulties, mesoscale simulation approaches (Figure 12) such as Dissipative Particle Dynamics (DPD), Brownian Dynamics (BD), Stokesian Dynamics, and Multi-Particle Collision Dynamics (MPCD) have been developed. In connection to my work, we have used some of these techniques to study the flow behavior of polymeric systems. We used combined MD and MPCD simulations, while coarse-grained DPD simulations are used to study the phase behavior of block copolymers. The detail of these techniques is described below.

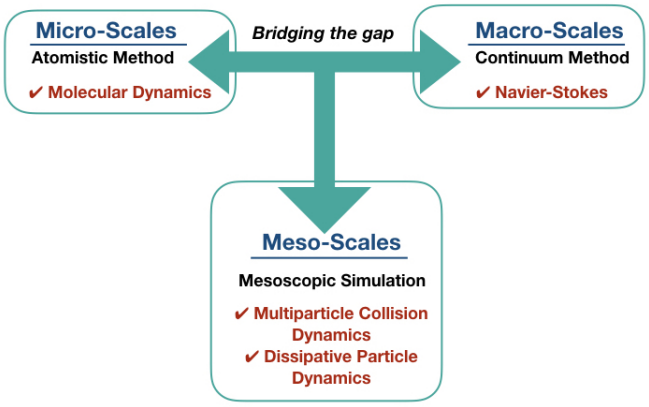

Figure 12: Mesocale techniques-bridging the gap between micro and macro scales [86].

3.1 MOLECULAR DYNAMICS

Molecular Dynamics is a valuable means to calculate the equilibrium and transport properties of many-body systems. It acts as a bridge (Figure 13) between length and time scales of microscopic and macroscopic properties as shown in Figure 13. MD simulations give insight to experiments by revealing hidden details that are otherwise difficult to access in the laboratory due to complexity and high cost.

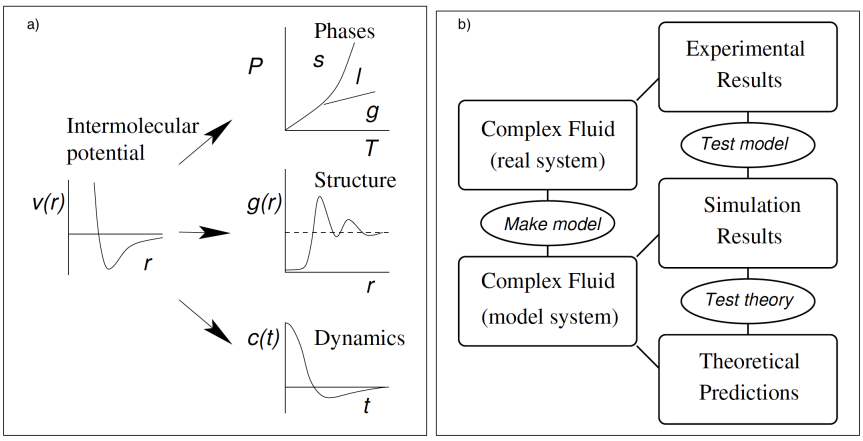

Figure 13: Simulations as a bridge between (**a**) microscopic and macroscopic; (**b**) theory and experiment [87].

In MD simulations we basically solve the Newton's equation of motion of N number of particles (typically N is very large) interacting via relevant potential. The equation of motion of the i^{th} particle is given as

$$\mathbf{v}_i = \frac{d\mathbf{r}_i}{dt}, \sum_{i \neq j} \mathbf{F}_{ij} = \frac{d\dot{\mathbf{r}}_i}{dt}, \tag{63}$$

where $\mathbf{r}_i$ and $\mathbf{v}_i$ are the position and velocity of the i^{th} particle and $\mathbf{F}_{ij}$ is the force exerted by particle i on particle j. In order to measure any observable macroscopic thermodynamic property in MD simulations, the corresponding observable has to be first expressed in terms of the position and momentum of the particles in the system. Here, each atom or molecule is given by position $\mathbf{R}_i$ or momentum $\mathbf{P}_i = m_i \mathbf{v}_i$, to propagate the particles in time. For this purpose, we need to calculate the forces $\mathbf{F}_i$ acting on particles, which are usually expressed in terms of potential energy $U(\mathbf{R}^N)$, where $\mathbf{R}^N = (\mathbf{R}_1, \mathbf{R}_2, ..., \mathbf{R}_N)$ represents the complete set of 3N coordinates. The Hamiltonian H of the system can be written as

$$H(\mathbf{P}^N, \mathbf{R}^N) = \sum_{i=1}^{N} \frac{\mathbf{P}_i^2}{2m_i} + U(\mathbf{R}^N), \tag{64}$$

here $\mathbf{P}^N$ is the union of all momenta, $\{\mathbf{P}_1, \mathbf{P}_2, ..., \mathbf{P}_N\}$ and $\mathbf{R}^N$ is the union of all positions, $\{\mathbf{R}_1, \mathbf{R}_2, ..., \mathbf{R}_N\}$ and $U(\mathbf{R}^N)$ is the potential energy as a function of the positions [88]. Details on the form of the potential energy will be provided later in this chapter. The forces acting on the particles are derived from the potential as,

$$F_i(\mathbf{R}^N) = -\frac{\partial U(\mathbf{R}^N)}{\partial \mathbf{R}_i}. \tag{65}$$

The equations of motion according to the Hamiltonian's equation are

$$\dot{\mathbf{R}}_i = \frac{\partial H}{\partial \mathbf{P}_i} = \frac{\mathbf{P}_i}{m_i}, \tag{66}$$

and

$$\dot{\mathbf{P}}_i = -\frac{\partial H}{\partial \mathbf{R}_i} = -\frac{\partial U}{\partial \mathbf{R}_i} = F_i(\mathbf{R}^N). \tag{67}$$

To integrate the equation of motion, different algorithms have been introduced in MD simulation. The most common and efficient algorithm used so far for integration is Velocity Verlet algorithm as it is time reversible and conserves the phase and volume space [88, 89]. To derive it we use the Taylor expansion of the coordinate $\mathbf{R}_i$ of a particle at time $t + \Delta t$

$$\mathbf{R}_i(t + \Delta t) = \mathbf{R}_i(t) + \mathbf{V}_i(t)\Delta t + \frac{\mathbf{F}_i(t)}{2m_i}\Delta t^2 + \frac{\Delta t^3}{3!}\dddot{\mathbf{R}}_i + \mathcal{O}(\Delta t^4), \tag{68}$$

where Δt is the MD time step, and the estimated error in the new position is of the order of Δt^4. In Velocity Verlet algorithm the velocity and position of a given particle is computed at time t and $t + \Delta t$, using the following equations

$$\mathbf{R}_i(t + \Delta t) - \mathbf{R}_i(t - \Delta t) = 2\mathbf{V}_i(t)\Delta t + \mathcal{O}(\Delta t^3). \tag{69}$$

or

$$\mathbf{V}_i(t) = \frac{\mathbf{R}_i(t+\Delta t) - \mathbf{R}_i(t-\Delta t)}{2\Delta t} + \mathcal{O}(\Delta t^2)\,. \tag{70}$$

Here, the estimated error in velocity is $\sim \Delta t^2$ and temperature, potential energy, and total energy is calculated at each time step. The total energy should be conserved throughout the MD simulation. The old positions and velocities at $t - \Delta t$ can be discarded after all calculations, and the new positions and the velocities become the next starting point. The steps are repeated a given number of times in order to reach the desired time frame.

This integration scheme conserves the total potential energy E, so if the total number of particles N and the total volume V are also kept constant, then the simulation is performed in the microcanonical ensemble NVE. However, typical experiments in the labs are usually performed at constant temperature and not constant energy. Therefore, we need to reproduce an isothermal ensemble in MD simulations, where the number of particles, volume, and temperature T is fixed; this ensemble is called canonical ensemble NVT. We can ensure the constant temperature by applying a thermostat to the system. Popular methods to control temperature include the velocity rescaling thermostat, Nosé-Hoover thermostat, Langevin thermostat, Andersen thermostat, Berendsen thermostat, and Dissipative Particle Dynamics (DPD) thermostat. The DPD thermostat will be discussed in a later section, and the Langevin thermostat will be discussed here.

In a Langevin thermostat the movement of particles is described through a modified Newton's equation of motion which maintains the temperature though [90, 91]

$$m\ddot{\mathbf{R}}_i = \mathbf{F}_C - m\gamma\dot{\mathbf{R}}_i + \mathbf{F}_R\,, \tag{71}$$

where $\mathbf{F}_C$ are the forces on the particles, γ is the drag coefficient and $\mathbf{F}_R$ is the random force which is related to γ by the fluctuation-dissipation theorem, $< \mathbf{F}_R{}^2 >= 2d\gamma k_B t/\Delta t$ with Δt being the time step used in MD and d being the dimensionality.

Generally, a system of N particles is surrounded by vacuum, but in order to simulate the bulk properties of solids and liquids, we need certain boundary conditions. Periodic boundary conditions (PBC) are used in order to (artificially) create large bulk systems in MD simulations in which the cubic box is surrounded by the replicas of itself throughout space to form an infinite lattice. We adopt the minimum image convention where each particle interacts with the nearest atom or image in the periodic array. During the course of the simulation, when an atom moves in the original box, its periodic image moves in the same way in each of the neighboring boxes. This means as soon as the atom leaves a box, its image will enter through the opposite side. There are no walls or surface atoms at the boundary of the original box. This box forms a convenient axis system for measuring the coordinates of the N particle system. A two-dimensional image of such a periodic system is shown in Figure 14. The number density in the central box (implied to the entire system) is conserved. Also, we need not save the coordinates of the entire system; just storing the coordinates of particles of the original box is sufficient [88]. It is important to note that the imposed artificial periodicity works well with short-range interaction potentials but fails for long-range ones like for charged and dipolar systems.

The forces in a system are calculated by pairwise adding the forces on each pair of a molecule. Hence, calculating the forces in an MD simulation can quickly become costly as it involves a large number of pairwise calculations. So, for a short-range energy function, we can restrict the summation by making an approximation. Since the largest contribution to the forces or potential comes from neighbors close to the atom of interest, we normally apply a spherical cutoff, meaning setting the pair potential $V(r)$ to zero for pair distance, greater and equal to the cutoff distance r_c. The introduction of a spherical cutoff should be a small perturbation, and to ensure the minimum effect of this, we need to choose the cutoff distance large enough [88].

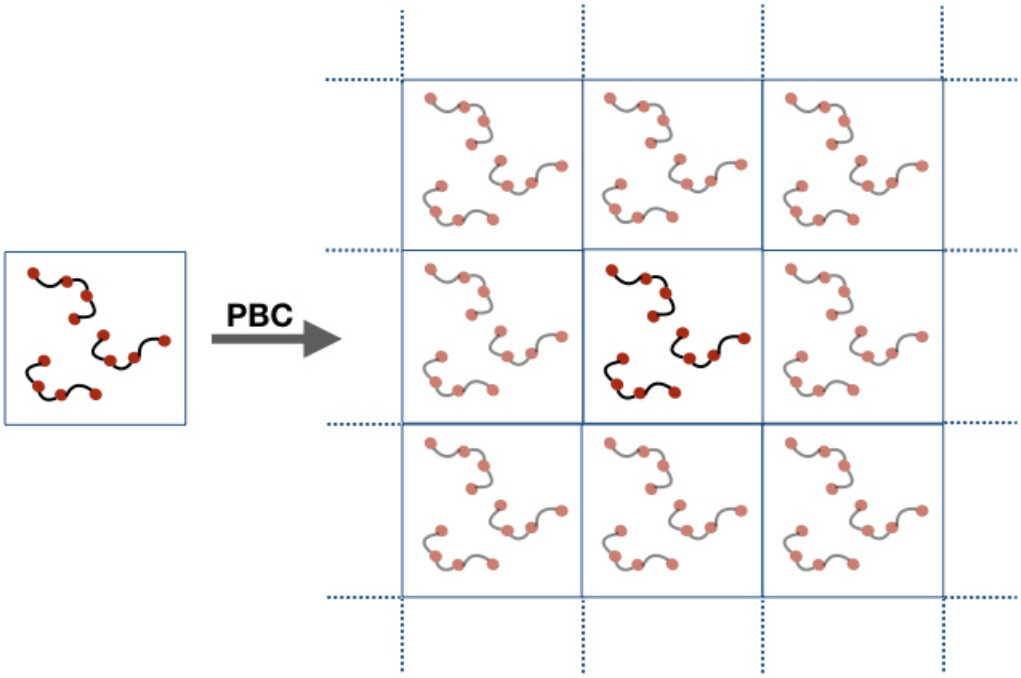

Figure 14: A two dimensional periodic system, the duplicate boxes i.e the image boxes are shown with dull color whereas the original box is shown in bright color.

3.2 MULTI PARTICLE COLLISION DYNAMIC

MPCD was first introduced by Malevenats and Kaprel [92] and is generally termed as stochastic rotation dynamics (SRD) [93], depending on the initial variant of the algorithm. The main aim of MPCD simulation is to adopt a coarse-grained simulation model, which is computationally inexpensive and correctly reproduces the solvent-mediated long-time hydrodynamic interactions. Also, in MPCD, dynamics are well defined for an arbitrary time step Δt, which does not have to be small compared to regular MD.

Algorithms

In MPCD, we model the solvent as a large number of point particles of mass m which move with a continuous distribution of velocity $\mathbf{v}_i$ in continuous space with position $\mathbf{r}_i$. The algorithm here consists of sequential streaming and collision steps (Figure 15).

The particle coordinates $\mathbf{r}_i(t)$ evolve according to Newton's equation of motion and updated at time t, as

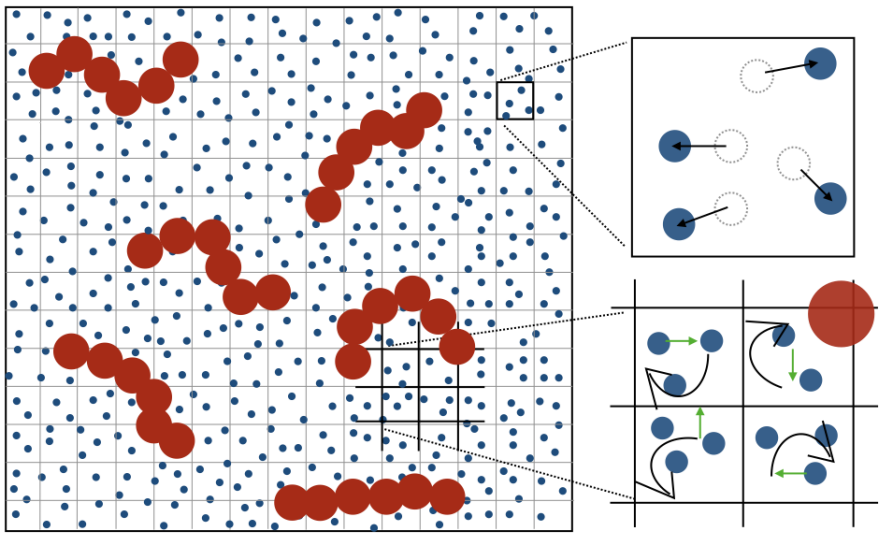

Figure 15: Figure showing streaming and collision step in MPCD simulations [94].

$$\mathbf{r}_i(t+\Delta t) = \mathbf{r}_i(t) + \Delta t \mathbf{v}_i(t)\,. \tag{72}$$

In the collision step, the particles are sorted into cells (Figure 15) and interact with the members of their own cell through stochastic collisions. The system is typically coarse-grained into cells of cubes with unit lattice constant a. The average number of particles per cell is one of the parameters that controls the solvent properties, and it typically ranges from 3 to 21. In SRD, the collision step consists of random rotation $\mathbf{R}$ of relative velocities $\delta\mathbf{v}_i = \mathbf{v}_i - \mathbf{u}$ of all the particles in a collision cell, $\mathbf{u}$ is the center-of mass velocity of each cell, $\mathbf{u} = \sum m_i\mathbf{v}_i / \sum m_i$,

$$\mathbf{v}_i(t+\Delta t) = \mathbf{u}(t) + \mathbf{R}\cdot\delta\mathbf{v}_i(t)\,. \tag{73}$$

There are multiple ways to implement stochastic rotation. The most commonly used in two dimensions is a rotation of $\mathbf{R}$ by an angle $\pm\alpha$, with a probability of $1/2$, and in three dimensions, a rotation by a fixed α about a randomly chosen axis. In general, equation 72 and equation 73 are required to perform MPCD simulations. Malevanets and Kapral [92] demonstrated an H-theorem for the algorithm, which means

that the particle velocity distribution is Maxwellian and yields the correct hydrodynamic equation for compressible flow. In the original form of SRD, the discretization of particles into cells leads to loss of Galilean invariance [93] when the mean free path is smaller than the cell size, which is more pronounced at low temperature and small time steps. This problem can be corrected by performing a random shift of the collision grid before every step. Also, Equation 73 only conserves linear momentum, not the angular momentum [95]. The collision rule can be modified so that angular momentum is also conserved [96], but only at the cost of loss of energy conservation. In order to maintain a constant temperature, the MPCD particles should be coupled to a thermostat, which is also important for non-equilibrium simulations. This can be achieved by incorporating the thermostat directly into the collision step, as in the Andersen thermostat (AT) scheme [97] which is known as MPCD-AT-a.

In this scheme, in the collision step new relative velocities are generated instead of the rotation of the particle velocities relative to center of mass velocity. The components of velocities are random numbers generated from Guassian distribution with variance $k_B T/m$. The collision rule is

$$\mathbf{v}_i(t+\Delta t) = \mathbf{u}(t) + \delta\mathbf{v}_i{}^{random}\,. \tag{74}$$

The salient feature of MPCD-AT is that it is both a collision procedure and a thermostat. Here, no additional velocity rescaling is required for non-equilibrium simulations, where there is no viscous heating. Like SRD, this algorithm (Equation 74) conserves momentum at the cell level but not angular momentum. Angular momentum conservation can be obtained by imposing constraints on the new relative velocity and is called MPCD-AT+a [95, 96].

One of the differences between MPCD-AT and SRD is that the relaxation time decreases when the number of particles increases for MPCD-AT, which on the other hand, increases with the increasing number of particles for the SRD scheme. As a result, the average number of particles is limited to $3-20$ in the case of SRD, but

no such limitation exists for MPCD-AT, where relaxation time scales as $(\ln M)^{-1}$, M being the average number of particles in each cell.

3.3 DISSIPATIVE PARTICLE DYNAMIC

DPD is a coarse-grained approach to address mesoscale problems in complex fluids and soft matter. The DPD method was pioneered by Hoogerbrugge and Koelman [98] and was later reformulated by Espanol and Warren [99]. The main advantage of coarse-grained DPD simulations is that due to the clustering of particles into a coarse-grained bead, the computational work has been reduced significantly, facilitating the simulation of complex systems over a large period. Later, Groot and Rabone estimated the speed-up in such simulation as $1000\,\rho^{8/3}$ for a given volume of the system, ρ being the number density of the coarse-grained bead. Thus, for $\rho = 3$ and $\rho = 7$, the speed-up factor comes around 2×10^4 and 2×10^5 respectively [100]. In a DPD model the particles interact with each other with three types of forces, *i.e.*, a conservative force ($\mathbf{F}^C_{ij}$), a dissipative force ($\mathbf{F}^D_{ij}$) and a random force ($\mathbf{F}^R_{ij}$) [101]

$$\mathbf{F}_{ij} = \sum_{i \neq j} \left(\mathbf{F}^C_{ij} + \mathbf{F}^D_{ij} + \mathbf{F}^R_{ij} \right). \tag{75}$$

These forces conserve linear and angular momenta. The conservative force, $\mathbf{F}^C_{ij}$ is typically a soft repulsive force that acts along the line of centers. The dissipative or frictional force, $\mathbf{F}^D_{ij}$ represents the effect of viscosity and the random force $\mathbf{F}^R_{ij}$ represents the vibrational and thermal energy of the system. These force components are

$$\mathbf{F}^C_{ij} = w^C(r_{ij})\mathbf{e}_{ij}\,, \tag{76}$$

$$\mathbf{F}_{ij}^{D} = -\gamma w^{D}(r_{ij})[\mathbf{v}_{ij} \cdot \mathbf{e}_{ij}]\mathbf{e}_{ij}\,, \tag{77}$$

$$\mathbf{F}_{ij}^{R} = \sigma w^{R}(r_{ij})\theta_{ij}\mathbf{e}_{ij}\,, \tag{78}$$

where $\mathbf{e}_{ij} = \mathbf{r}_{ij}/\mathbf{r}_{ij}$, $\mathbf{r}_{ij} = \mathbf{r}_i - \mathbf{r}_j$, $\mathbf{r}_{ij} = |\mathbf{r}_i - \mathbf{r}_j$ and $\mathbf{v}_{ij} = \mathbf{v}_i - \mathbf{v}_j$. w^C, w^D and w^R are weight functions for conservative, dissipative and random forces. Here θ_{ij} is a Guassian white noise function with zero mean and unit variance, the relation between the two weight function is given as

$$w^{D}(r_{ij}) = [w^{R}(r_{ij})]^2 = \begin{cases} \left(1 - \frac{r_{ij}}{r_c}\right), & r_{ij} < r_c \\ 0, & r_{ij} \geqslant r_c\,, \end{cases} \tag{79}$$

$$\sigma^2 = \frac{2\gamma k_B T}{m}\,, \tag{80}$$

The algorithm in DPD is a Gallilean invariant thermostat which preserves the hydrodynamic interactions [102–104]. The conservative weight function is defined as

$$w^{C}(r_{ij}) = \begin{cases} A_{ij}\left(1 - \frac{r_{ij}}{r_c}\right), & r_{ij} \leqslant r_c \\ 0, & r_{ij} > r_c\,, \end{cases} \tag{81}$$

where A_{ij} is the repulsion parameter between i^{th} and j^{th} particle and r_c is the cut-off distance. Groot and Warren [1997] matched the compressibility of water and determined the repulsion parameter as the number density ρ and system temperature. To get the repulsion parameter between two different types of particles, they

related the DPD parameter to the Flory-Huggins χ parameter [100, 105, 106]. For $\rho = 3$, the self interaction parameter is, $A_{ii} = 25$.

3.4 POLYMER CHAIN MODEL

There are several models by which we can describe polymers for computational experiments, for example, the skeletal chain model, bead-stick model, bead-spring model, and pearl-necklace model [33].

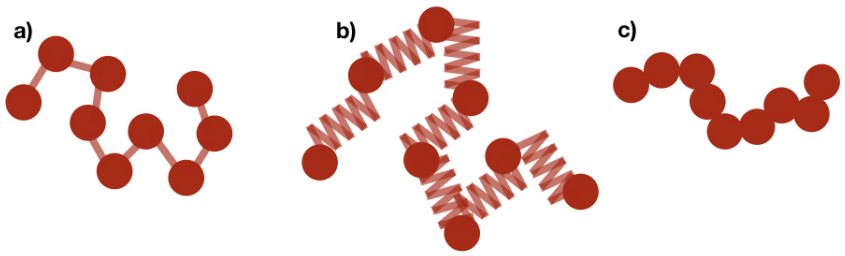

Figure 16: Models of polymer chain, (**a**) bead-stick model, (**b**) bead-spring model, (**c**) pearl necklace model.

In a bead-stick model, also know as a freely rotating model (Figure 16 a), the beads are connected to each other via stick. The properties of such a model can be varied by changing the diameter of the bead. Also, restricting the angle between two sticks or setting it free can have a significant effect. In a coarse-grained bead-stick model, each bead represents the center of a monomer unit consisting of several atoms. Each bead-stick represents a segment which is the smallest unit of a chain. Next, we have the bead-spring (Figure 16 b) model, which is similar to the bead-stick model, where we have a rigid stick in place of a spring. In this model, the virtual springs follow Hooke's law of elasticity, which implies they are infinitely extendable, with a linear elastic response. In a pearl necklace model (Figure 16 c), two adjacent beads are in direct contact *i.e.* it is similar to the bead-stick model with a stick length zero [33].

The bead-spring [107, 108] model will be discussed in more detail here, as it is one of the most popular models and it has been used in this work extensively. The average end-to-end distance at equilibrium for a bead-spring model consisting n beads and $n-1$ springs is given by

$$\langle R^2 \rangle_{eq} = \frac{3k_B T(n-1)}{k}, \tag{82}$$

where k is the Hookean spring constant. The bead-spring model usually behaves as an ideal chain.

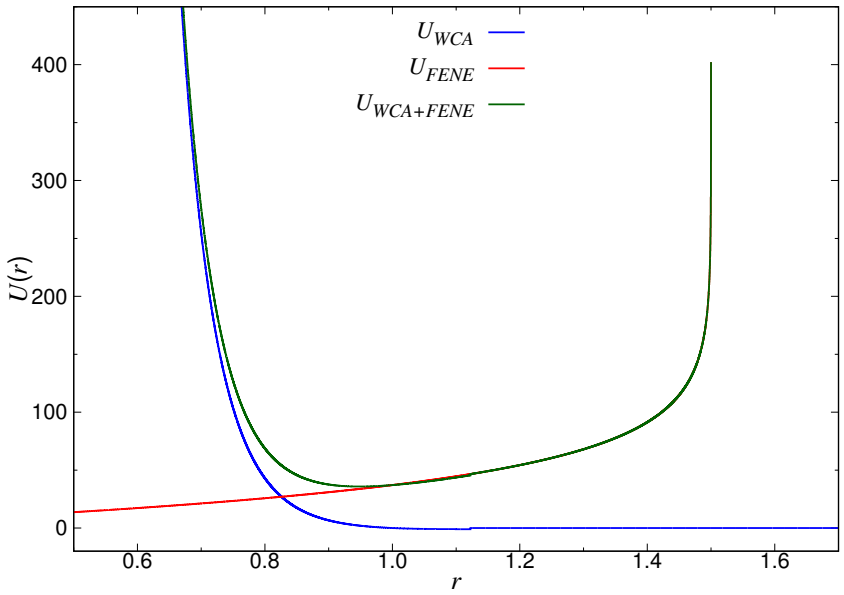

Figure 17: Plot showing WCA potential, FENE Potential and a combination of both.

In the DPD model, chain crossing is possible because the model is characterized by only weak repulsive interactions between the beads. In the MD model, the pair interactions between non-connected beads is given by the Weeks-Chandler-Andersen (WCA) potential, which is a Lennard-Jones (LJ) potential (13) shifted upward by ϵ and truncated at LJ potential minimum of $2^{1/6}\sigma$, σ being the minimum inter-particle distance at which the potential is zero

$$U_{WCA}(r) = \begin{cases} U_{LJ}(r) + \epsilon, & r < 2^{1/6}\sigma \\ 0, & r \geqslant 2^{1/6}\sigma, \end{cases} \tag{83}$$

The bonded interaction in such kind of model is often given by FENE (finitely extensible nonlinear elastic) [109] potential, which is

$$U_{\text{FENE}}(r) = -\frac{1}{2}kr^2 \ln\left[1 - \frac{{r_o}^2}{r^2}\right], \tag{84}$$

where r_o is the maximum bond length which has been set to $r_0 = 3/2\sigma$. The parameter k is the spring constant and has been chosen as $k = 30\epsilon/\sigma^2$. The equilibrium bond length is then calculated as a result of these two potentials used to describe a bead-spring model. Figure 17 shows the potential for $\sigma = 1$ and $\epsilon = 1$.

4

FLOW BEHAVIOR OF CHAIN AND STAR POLYMERS AND THEIR MIXTURES

4.1 INTRODUCTION

Separating particles is immensely important in many industrial as well as biological applications. For such separation, micro-fluidic devices have shown a promising ability, and significant progress has been achieved in their development [7–9, 22, 110–115]. These devices have already been implemented in several applications, including DNA sequencing and fragment sizing. The development of these microfluidic devices is advantageous as they are cost-effective and require a low amount of solvents and reagents. Advancement in such devices has the potential to take a step towards the complete development of lab on chip devices [116]. There is a tremendous interest in the scientific community to unravel the behavior of soft matter systems in microfluidic devices. Flexible polymers are one of the widely studied soft matter systems under flow as they exhibit interesting dynamical and flow properties in confinement [39, 41]. The flexibility of polymeric systems leads to simultaneous deformation of the dispersed polymer chains along with the distortion of the fluid flow field, which strongly affect each other. In channel flow, cross-stream migration of flexible polymers was observed due to hydrodynamic lift forces [58, 117, 118]. Previous studies focused on the flow properties of flexible polymer chains using experiments and simulations. Lately, studies have concentrated on star-shaped polymers as they are ultra-soft and comprised of many linear chains linked to a common center. Star-shaped polymer shows a continuous change of properties from soft linear chains to hard spherical colloid particles by tuning the number and length of arms [23, 119–122].

To establish a connection between the shape of star polymers and their flow properties, we carried out molecular dynamics (MD) simulations. Here, we modeled the

polymers using a generic bead-spring description in order to focus on the general physical mechanisms instead of replicating specific polymer chemistry. Hydrodynamic interactions (HI) were incorporated using the multi-particle collision dynamics (MPCD) algorithm.

4.2 MODEL AND SIMULATION DETAILS

In order to study the dynamics of star polymers under pressure-driven flow, we used a hybrid approach that combines standard MD simulations with the MPCD algorithm. This mesoscopic simulation approach takes into account long-ranged hydrodynamics in a physically accurate and computationally efficient way. We describe the dispersed macromolecules using a generic bead-spring model, where each star polymer consists of f linear chains with p beads each (often referred to as "arms"), which are attached to a common central particle (linear chains can be considered as star polymers with $f = 2$). Thus, a polymer consists of $N = fp + 1$ monomeric units in total. Each spherical bead has a diameter of σ, and the excluded volume interactions between the monomers are modeled through the purely repulsive Weeks-Chandler-Andersen (WCA) potential (Equation 83) [123].

The connection between consecutive monomers within a polymer is described by the FENE potential (Equation 84). The value of spring constant and maximum bond length used in this work is, $k = 30\epsilon/\sigma^2$ and $r_0 = 1.5\,\sigma$ respectively to prevent unphysical bond crossing [124]. With these parameters, the equilibrium bond length is $b \approx 0.97\sigma$.

The simulations are carried out in a slit-like channel with dimensions $L_x = 40\,\sigma$ in the gradient direction, $L_y = 40\,\sigma$ in the vorticity direction, and $L_z = 50\,\sigma$ in the flow direction. Figure 18 shows a schematic representation of the channel geometry and the resulting flow profile. Channel walls are located at $x = \pm L_x/2$ and are modeled as infinitely extended smooth planes, which interact with the monomers through a purely repulsive potential along the wall normal [125].

In MPCD (Section 3.2), the solvent particles are modeled as ideal point particles with unit mass $m = 1$ and their motion is governed by alternating streaming and

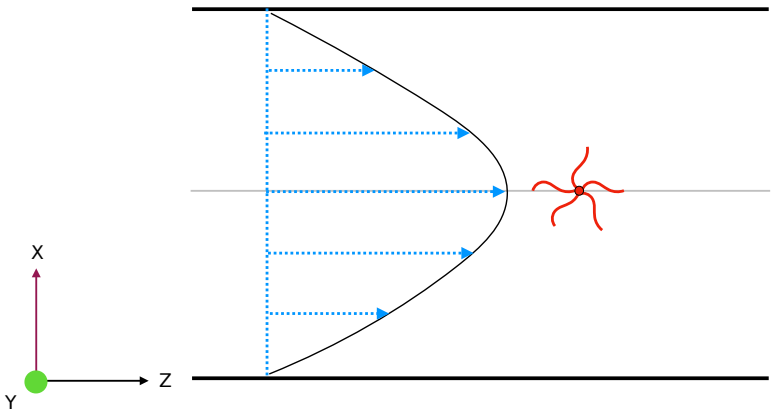

Figure 18: Schematic representation of channel geometry and the flow profile.

collision steps [92, 126]. In the streaming step, the solvent particles move ballistically for a time $\Delta\tau_{MPCD}$ and during the collision step, the solvent particles are sorted into cubic cells of edge length a, which also sets the length scale over which hydrodynamics are resolved [127]. Afterward, particles within the same cell exchange momentum through a stochastic collision while conserving linear momentum on both the cellular and global level. Here, we used an Andersen thermostat (MPCD-AT) collision scheme [128], which also acts as the thermostat in our simulations. In order to realize the interaction between monomers and solvent particles, the monomers are included in the MPCD collision step. The cubic cells were shifted before each collision by a random three-dimensional vector with components drawn uniformly on $[-a/2, +a/2]$ to ensure Galilean invariance [93]. To impose no-slip boundary conditions at the channel walls, we employed a bounce-back rule at the walls by filling the cells that are intersected by the walls with virtual solvent particles [129]. Poiseuille flow was achieved by applying a body force g to all solvent particles [127, 130–132].

The equation of motion for the dispersed solute particles is integrated using the standard velocity Verlet algorithm, with MD time step $\Delta t_{MD} = 2 \times 10^{-3}\,\tau_{MD}$ measured in the reduced unit of time $\tau_{MD} = \sqrt{m\sigma^2/(k_B T)}$. The time step for the MPCD algorithm was set to $\Delta t_{MPCD} = 0.1$, *i.e.*, a stochastic collision was performed every 50 MD step. The cell size was set to $a = \sigma$ and the number density of solvent particles was set to $\rho_s = 5\,\sigma^{-3}$. The mass of the monomers was set to $M = 5$ m. With these parameters, the pure MPCD solvent has a dynamic zero-shear viscosity of $\eta_s = 3.71$ and a Schmidt number of $Sc = 8$ [133], which is consistent with a liquid-

like solvent [134]. Simulations were conducted up to $10^5\tau_{MD}$, and we ensured that the systems reached a steady state before taking measurements. For every set of parameters, we conducted five independent runs to improve sampling and to calculate error bars. Due to the symmetry of the channel geometry, we consider only absolute displacements from the centerline $x = 0$ to improve sampling. Further, if not stated otherwise explicitly, we will use σ as our unit of length, k_BT as our unit of energy, and τ_{MD} as our unit of time. Simulations without hydrodynamics were performed using HOOMD-blue (v.2.2.4) [135–137].

4.3 RESULTS AND DISCUSSION

4.3.1 *Ultradiulte conditions*

In the first part of this work, we studied the flow behavior of single star polymers at infinite dilution for various arm numbers f. Here, we tuned the arm length p (and thus the total number of monomer N) so that, in an unconfined system, the polymers have roughly the same radius of gyration $R_g \approx 4.2$ at each value of f. In particular, we studied linear chains with $N = 40$ monomers, and star polymers with $f = 18$ ($N = 181$) and $f = 30$ ($N = 271$).

Under quiescent conditions, the spatial distribution of the polymer center of mass (CM) between the channel walls, $P_{cm}(x)$, is almost uniform, except for a narrow region of width $\approx R_g$ close to the channel walls (see Figure 19 a). Note that the transition of $P_{cm}(x)$ near the walls becomes significantly sharper with increasing f, since the interior of the polymers is packed more compactly with the constituent monomers, and thus it is more difficult to deform the macromolecule [138]. (For a completely hard colloid, $P_{cm}(x)$ is a step function.) To quantify the shape of the polymers, we computed the radius of the gyration tensor

$$G_{\alpha\beta} = \frac{1}{N-1}\sum_i \left(\Delta r_{i,\alpha}\Delta r_{i,\beta}\right)^2 , \tag{85}$$

where $\Delta r_{i,\alpha}$ is the position of monomer i relative to the polymer CM, while α and β are the components along the Cartesian x, y, and z direction. The polymer radius of gyration is then given by $R_g^2 = G_{xx} + G_{yy} + G_{zz}$. Figure 19 b shows G_{xx} between the channel walls, and it is clear that in the channel center, G_{xx} is independent of f and has the same value as in unconfined systems. When the polymer CM approaches the walls, however, G_{xx} decreases drastically for the linear chains ($f = 2$), whereas this effect is much weaker for the star polymers.

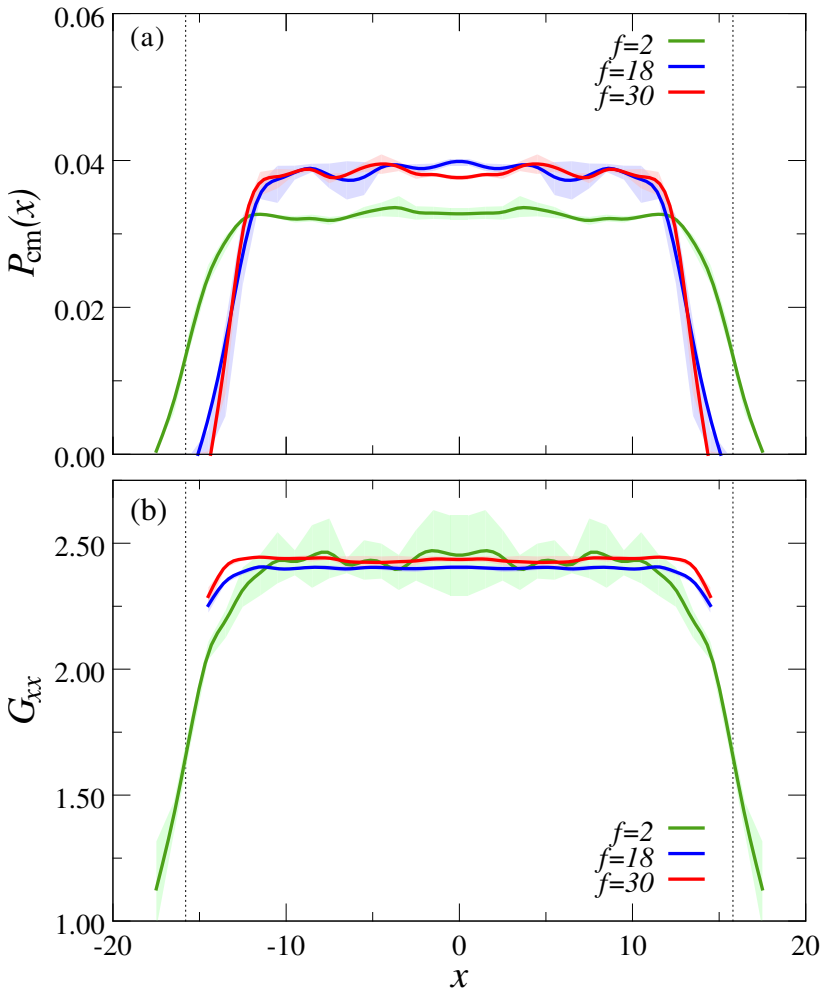

Figure 19: (a) Center of mass probability distribution between the walls, $P_{cm}(x)$, for various arm numbers f at rest. (b) Component of the radius of gyration tensor between the channel walls (G_{xx}) as a function of x. In both panels, the shaded regions around the curves indicate our measurement uncertainty. The dotted vertical lines indicate the excluded regions of width R_g near the channel walls.

When a constant body force g is applied to the liquid along the z direction, then a steady flow develops as a result of the balance between acceleration in the channel center and friction at the channel walls. Due to the low polymer concentration, the

dispersion behaves essentially like a Newtonian liquid with shear viscosity $\eta = \eta_s$, and the resulting velocity profile is parabolic

$$v_z(x) = \frac{g}{2\nu}\left(\frac{L_x^2}{4} - x^2\right), \tag{86}$$

where $\nu = \eta/\rho$ is the kinematic viscosity of the liquid. The velocity profile has its maximum v_{max} in the channel center ($x = 0$) and becomes zero at the channel walls ($x = \pm L_x/2$). The parabolic shape of $v_z(x)$ leads to a locally varying shear rate $\dot{\gamma}(x) = dv_z(x)/dx = -gx/\nu$, which is maximum at the channel walls and vanishes in the channel center. In the following, we will quantify the flow strength in terms of the particle Reynolds number, $Re_p = 2v_{max}R_g/\nu$, which is the ratio between inertial and viscous forces acting on the dispersed polymer. Note that this expression is somewhat approximative, as polymers can deform under flow and thus R_g is not constant. Nevertheless, this quantity provides a reasonable measure for estimating the onset of inertial flow effects ($Re_p \gtrsim 1$).

In Figure 20, we have plotted how the CM distribution of the polymers, $P_{cm}(x)$, changes under flow. As Re_p is increased, both the chains ($f = 2$) and stars ($f = 30$) move away from the channel walls due to the wall-induced asymmetry in the wake vorticity field of the dispersed polymers [58, 117, 139, 140]. This cross-stream migration is significantly more pronounced for the star polymers compared to the linear ones, as the former contains almost seven times as many monomers ($N = 271$ *vs.* $N = 40$), and thus disturb the flow field to a greater extent. Further note that $P_{cm}(x)$ develops a distinct dip near the channel center at the highest investigated flow rates, $Re_p = 6$, for the chains as well as the stars. This partial evacuation of the centerline originates from the nonuniform shear field $\dot{\gamma}(x)$, which leads to a position-dependent polymer deformation (see Figure 21 below) and a subsequent gradient in the chain mobility [58, 117, 139, 140]. Star polymers with $f = 18$ arms exhibit an intermediate behavior, and have been omitted from Figures 20 and 21 for the sake of clarity.

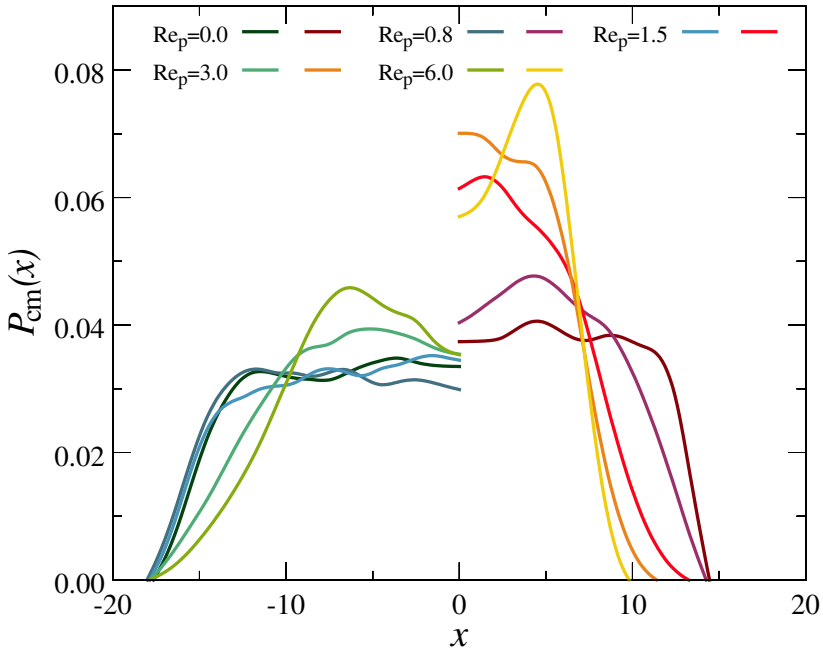

Figure 20: Center of mass probability distribution between the walls, $P_{cm}(x)$, for a chain (left) and a star with $f = 30$ arms (right) at various flow strengths Re_p, as indicated.

Shear deformation of the dispersed polymers occurs typically when $\dot{\gamma}$ exceeds the inverse of the characteristic relaxation time, τ_c^{-1} (or, equivalently, when the Weissenberg number $Wi \equiv \dot{\gamma}\tau_c^{-1} \gtrsim 1$) [10, 32, 41, 141, 142]. For linear chains in dilute solutions, τ_c is essentially given by the slowest Zimm relaxation mode, *i.e.*, $\tau_c = \tau_0 N^{3\nu}$ with $\tau_0 = \eta_s b^3/(k_B T)$ and Flory exponent $\nu \approx 3/5$ [41, 143]. For star polymers, a similar calculation for the blob model leads to the expression $\tau_c = \tau_0 p^{3\nu} f^{1-3\nu/2}$ [144], which has been verified through simulations [141] for the range of star sizes investigated here. One interesting result of these theoretical considerations is that a star relaxes of order $f^{-1/2}$ faster than a linear chain of the same overall R_g [144]. For the polymers investigated in this work, we estimate $\tau_c = 2,600$ (linear chain), $\tau_c = 285$ ($f = 18$, $p = 10$), and $\tau_c = 250$ ($f = 30$, $p = 9$).

To investigate the flow-induced deformation of the polymers, we have plotted in Figure 21 the components of the radius of gyration tensor along the gradient and flow direction, G_{xx} and G_{zz}, respectively, as a function of the polymer CM position between the walls x. (The size along the vorticity direction, G_{yy}, changed only marginally and therefore has been omitted for the sake of brevity.) Here, we can see that G_{xx} in the channel center is almost independent of Re_p, but then decreases

gradually as the polymer CM approaches the high $\dot{\gamma}$ region close to the channel walls. Further, it is clear that, at a fixed CM distance, G_{xx} drops with increasing flow strength since $\dot{\gamma} \propto Re_p$. At the same time, the extension along the flow direction, G_{zz}, increases significantly both with distance to the centerline and flow strength. Comparing the $G_{\alpha\alpha}$ data for the chains and stars, it is clear that the flow-induced deformation is much more pronounced for the linear species. This finding can be rationalized by realizing that the characteristic relaxation time of the chain is approximately one order of magnitude slower than that of the star (see discussion above). Further, even for $Wi \gg 1$, the compact structure of star polymers prevents full extension along the flow direction, as the arms would significantly overlap in such a scenario.

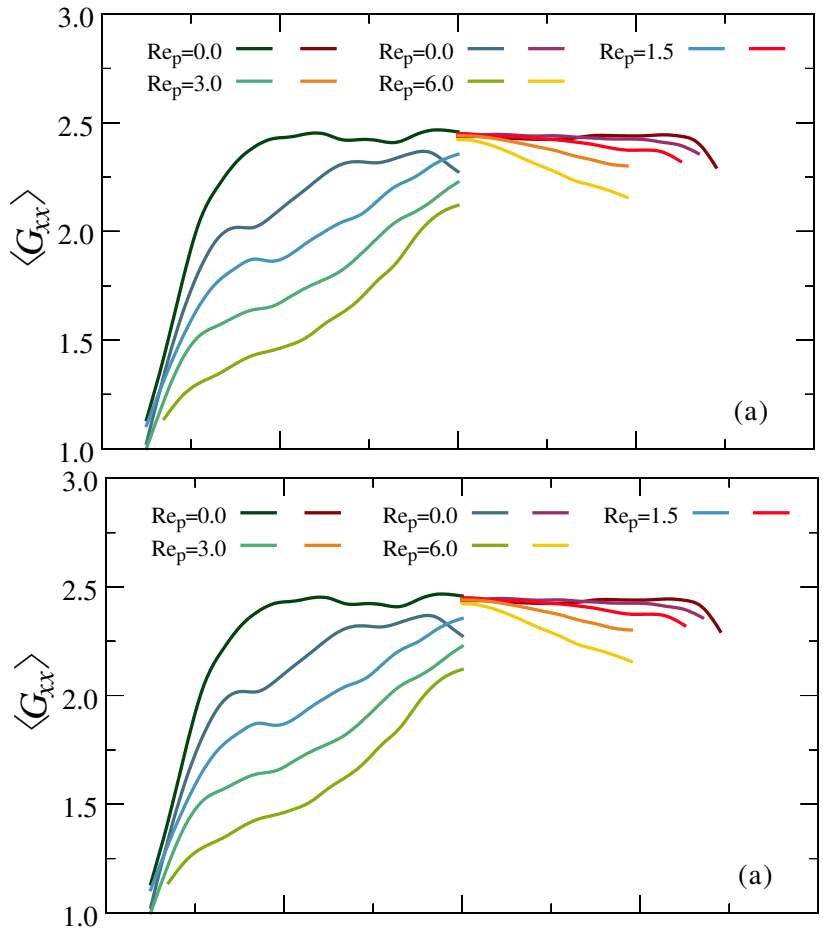

Figure 21: Components of the radius of gyration tensor along (**a**) the gradient and (**b**) the flow direction *vs* the polymer CM position x. Data shown for a chain (left) and a star with $f = 30$ arms (right) at various flow strengths Re_p, as indicated.

In Figure 22 we have plotted the x and z components of the radius of gyration tensor averaged over the entire channel, $\langle G_{xx} \rangle$ and $\langle G_{zz} \rangle$, respectively, as a function of Re_p. Here, we can see that the average extension along the flow direction, $\langle G_{zz} \rangle$, is much more pronounced for the linear polymers compared to the star polymers, which exhibit only weak stretching. (The theoretical maximum of G_{zz} for sheared linear polymers is on the order of half the chain contour length.) A similar trend can be observed for the average contraction in the gradient direction, $\langle G_{xx} \rangle$, which is significantly more expressed for the chains than for the stars. Thus, in this context, the star polymers resemble progressively rigid colloids as the number of arms f is increased.

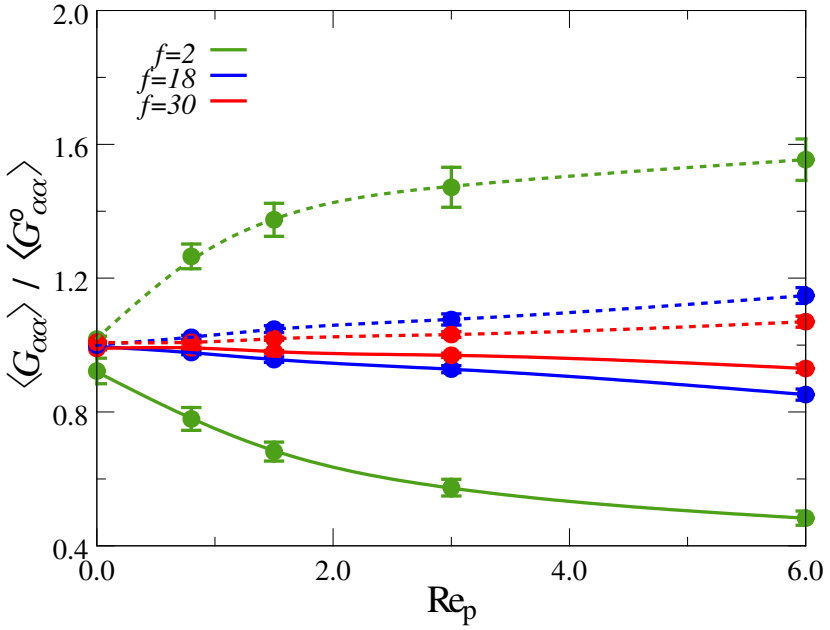

Figure 22: Components of the radius of gyration tensor averaged over the entire channel *vs* flow strength Re_p, normalized by the value at rest. Dashed lines show component in flow direction, $\langle G_{zz} \rangle$, and solid lines show component in gradient direction, $\langle G_{xx} \rangle$ (reprinted with permission [145]).

Based on previously established similarities between the elasticity of polymeric nanoparticles and deformable droplets at rest [138] it is tempting to also draw analogies for the flow-induced migration of the two species. Previous analytical models of droplets in the Stokes regime ($Re \ll 1$) predict that migration to the channel center should occur if the ratio of viscosities of the suspended phase and of the surrounding fluid is either smaller than 0.5 or larger than 10 [146, 147]. In between these ratios, the droplets are predicted to move *a*way from the centerline. However, recent simu-

lations of deformable droplets in the inertial flow regime ($Re \gtrsim 1$) have also found migration *t*owards the centerline for viscosity ratios from unity to 13 [148]. Further, it was shown that these lift forces increase with increasing droplet deformability [148, 149].

Applying those findings to the macromolecular particles studied here, one could then expect that the higher deformability of the linear chains should lead to stronger lift forces towards the channel center compared to the stars. This situation is, however, clearly *n*ot the case here as evidenced by the probability distribution $P_{cm}(x)$ shown Figure 20. One possible explanation for this discrepancy could be that the solvent can (partially) flow through the polymers, whereas the droplets are completely impermeable. Further, the dynamics of polymers are governed by a hierarchy of relaxation times, originating from the many internal degrees of freedom.

We instead hypothesize that the cross-stream migration observed for the polymers stems from wall-induced hydrodynamic lift forces, which are more pronounced for the denser star polymers compared to the chains. To test this hypothesis, we conducted additional simulations where we switched off HI by employing a Langevin thermostat. At rest, the polymer distribution $P_{cm}(x)$ looks identical to the data shown in Figure 19, as expected, since hydrodynamics do not affect the static properties at equilibrium. The flow was then applied to the system by superimposing a velocity profile with the same parabolic shape and amplitude as in our previous explicit solvent simulations. Here we found that the polymer distribution $P_{cm}(x)$ was identical for all values of Re_p, *i.e.*, no cross-stream migration occurred in the simulations without hydrodynamics. This behavior can be rationalized by considering that the interaction matrix, relating the forces acting on the beads and their velocities, is diagonal when hydrodynamics are neglected; in this scenario, the motion along the individual directions (x, y and z) is fully decoupled, and the underlying equations of motion can be solved independently. Hence, we can conclude that the cross-stream migration displayed in Figure 20 originates from hydrodynamic lift forces.

4.3.2 *Polymer Mixtures*

Our simulation results under ultradilute conditions revealed that the cross-stream migration behavior of polymers depends on their number of arms f (and thus their deformability), where polymers moved more and more towards the channel center with increasing f. This finding suggests the possibility of separating mixtures of polymers with different f *via* Poiseuille flow. To test this idea, we first prepared mixtures containing $N_2 = 13$ and $N_{30} = 13$ chains ($f = 2$) and stars ($f = 30$), respectively. This choice leads to a volume fraction of $\Phi = 4\pi R_g^3(N_2 + N_{30})/(3V) \approx 0.1$, *i*.e., the system is still in the dilute regime (note that $R_g \approx 4.2$ for all investigated values of f).

Figure 23 shows the probability distribution of the polymer CM between the channel walls, $P_{cm}(x)$. At rest, the chains are uniformly distributed across the channel, similar to the case at infinite dilution (*c*f. Figure 19 a). The stars, however, are not uniformly distributed anymore but exhibit a distinct layering near the walls. This ordering is due to the fact that the effective interactions between star polymers become progressively hard-sphere like with increasing f; for such (almost) hard spheres, ordered structures near a flat wall result from the excluded volume interactions both within the particles and against the confining wall [150–153].

When flow is applied, the star polymers vacate the region near the walls and migrate to the channel center, as evidenced by the distinct peak at $x = 0$ in Figure 23 b. We can identify two additional, slightly smaller peaks near the centerline at $x \approx \pm 2R_g$, which stem from the saturation of the centerline. At the same time, the linear polymers are largely expelled from the channel center and fill the region near the walls, where they attain a rather stretched-out conformation. In principle, this clear spatial separation of chains and stars under flow allows for a straight-forward separation of the two species.

To elucidate the origin of this flow-induced separation, we again conducted simulations without HI. At rest, we find the exact same distribution as shown in Figure 23 a, as expected. When flow is applied, we observe a qualitatively similar partial focusing of star polymers to the centerline with some differences (*c*f. Figure 23 b and c). When HI is switched off, the chain distribution is somewhat more homogeneous, and the

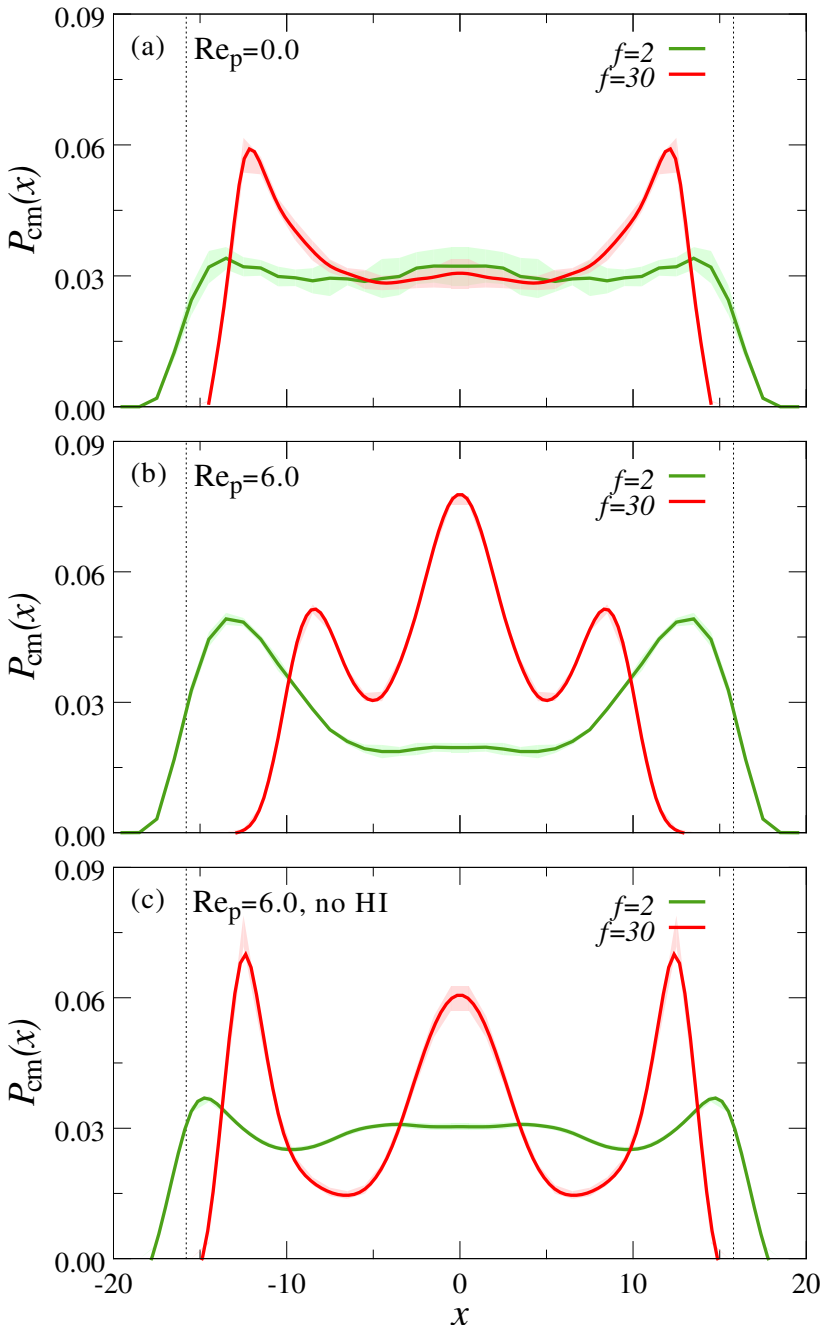

Figure 23: Center of mass probability distribution $P_{cm}(x)$ for a mixture of chains ($f = 2$) and stars ($f = 30$) at (**a**) rest ($Re_p = 0$) and (**b**) under flow ($Re_p = 6$). Panel (**c**) shows the system under flow ($Re_p = 6$), but with hydrodynamic interactions switched off. The volume fraction of polymers is fixed to $\Phi = 0.1$ in all simulations.

two off-center peaks in the star distribution move now closer to the walls. The fact that flow influences the lateral distribution of polymers in the mixtures without HI (in contrast to the infinitely dilute systems discussed in Section 4.3.1) provides crucial insights to the responsible separation mechanism: the non-uniform shear field $\dot{\gamma}(x)$ leads to a more pronounced stretching of the chains near the walls (see Figure 21

b), which thereby push the less deformable stars to the channel center. This effect is somewhat more pronounced in the simulations with HI, likely due to wall-induced hydrodynamic lift forces. We note that this behavior is reminiscent of the viscoelastic focusing of rigid colloids in polymer solutions [112, 130, 131]. However, the mass fraction of linear polymer in the present simulations is much smaller (0.65%) than the typical values of $5-10\%$ used in previous simulations [130, 131] and experiments [111, 112], which might explain the somewhat less pronounced focusing observed here.

In order to explore whether this setup can also be used to separate stars with different numbers of arms, we repeated our simulations for a mixture of $N_{18} = 13$ and $N_{30} = 13$ stars with $f = 18$ and $f = 30$ arms, respectively. The volume fraction is again $\Phi \approx 0.1$. Figure 24 a shows the equilibrium distribution of the stars between the walls, $P_{cm}(x)$, and we can see again that the less deformable species ($f = 30$) occupies the central channel region, whereas the softer particles ($f = 18$) are pushed closer to the walls. Here, we can identify a distinct layering of the stars, which is more pronounced compared to the star-chain mixtures due to stronger excluded volume effects.

Under Poiseuille flow, stars with $f = 18$ as well as $f = 30$ arms move somewhat closer to the channel center, and the lateral layering is slightly smeared out (see Figure 24 b). However, in contrast to the star-chain mixtures, there is no obvious spatial partitioning between the different star species, which could be exploited for particle separation. When hydrodynamics are switched off, the lateral polymer distribution, $P_{cm}(x)$, becomes slightly broader due to the lack of wall-induced hydrodynamic lift forces, but the overall behavior is qualitatively similar. The less pronounced flow-induced focusing in the star-star mixtures can thus be attributed to the weaker viscoelastic forces exerted by the stars compared to the chains.

For achieving a connection between our simulations and experiments beyond a comparison of dimensionless quantities (such as the Reynolds and Weissenberg number), it is required to establish a mapping between the units of energy, length and time. For the energy scale, we chose the thermal energy $\varepsilon = k_B T$, which at room temperature ($T_{room} = 298\,K$) is $\varepsilon = 4.11 \times 10^{-21}\,J$. For the length scale, we map

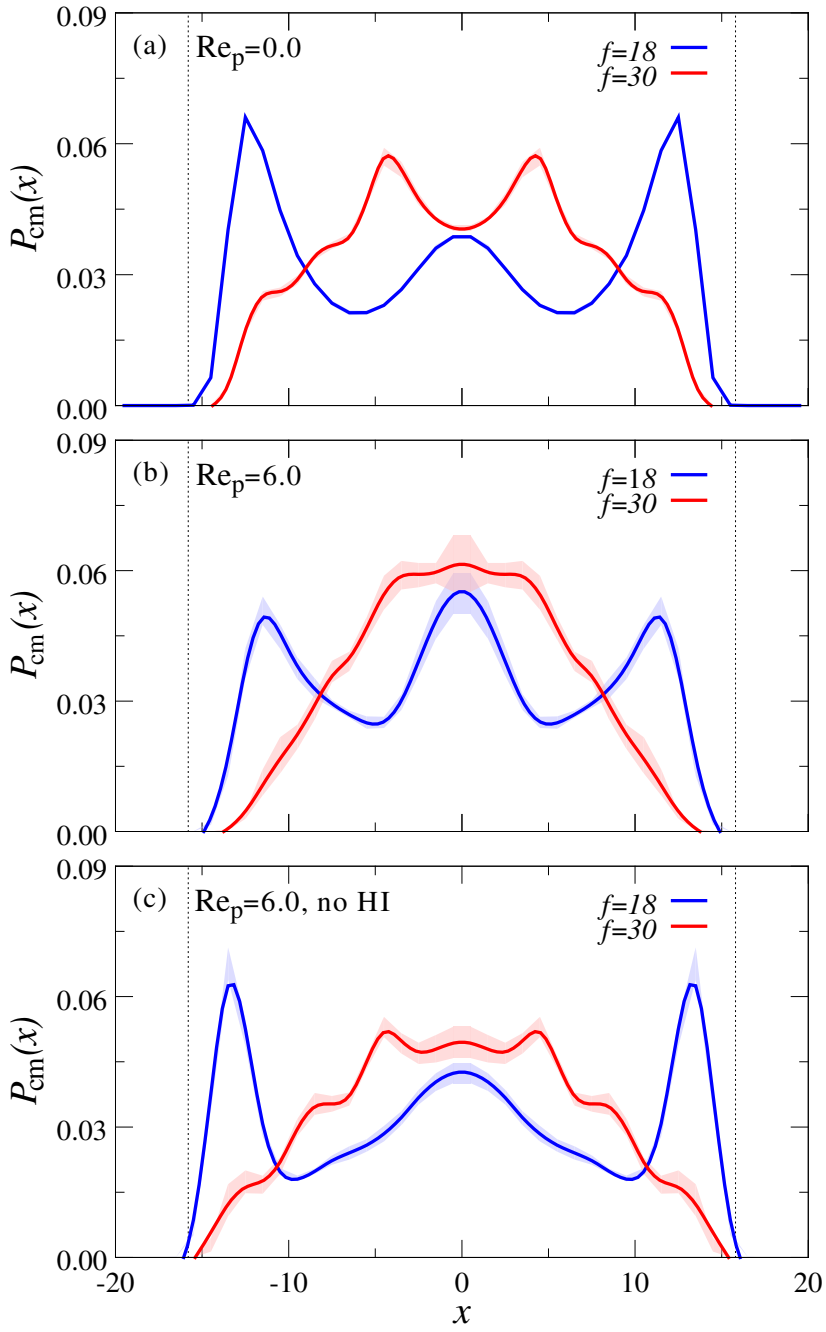

Figure 24: Same as Figure 23, but for a mixture of stars with f = 18 and f = 30 arms.

our linear polymers to poly(ethylene oxide) (PEO) chains with molecular weight $M = 4000\,\mathrm{kg\,mol^{-1}}$, as used in previous viscoelastic focusing experiments [112]. The radius of gyration of PEO chains in water can be estimated via $R_g = 0.215\,M^{0.583}$, with molecular weight M given in mol [154]. Thus, $R_g \approx 150\,\mathrm{nm}$ which leads to a conversion factor of $\sigma = 36\,\mathrm{nm}$. (Please note that this mapping is rather crude, since

roughly 2270 monomers are represented by a single bead, and thus the employed WCA excluded volume interactions between beads are likely too hard.) For the time scale, we matched the long-time diffusion coefficient D of a single chain at dilute conditions. In the simulations we find $D = 0.0045\,\sigma^2/\tau_{MD}$ [133]. The diffusion coefficient of the experimental system can be estimated via $D = k_B T/6\pi\eta_s R_h$ with hydrodynamic radius R_h. Using $\eta_s = 0.89\,\mathrm{cP}$ for water at room temperature and $R_h = 85\,\mathrm{nm}$ [154], we find $D \approx 2.9 \times 10^{-8}\,\mathrm{cm^2 s^{-1}}$ and thus $\tau_{MD} \approx 2.0\,\mu\mathrm{s}$. Using these conversion factors, our channels have a width of $L \approx 1.5\,\mu\mathrm{m}$ and the maximum fluid velocity is $v_{max} \approx 1\,\mathrm{cm\,s^{-1}}$ at $Re_p = 6$. Such velocities can be achieved in a slit channel by applying a pressure drop of 100 kPa over a channel length of 3 mm. Flow-induced partitioning occurred in the star-chain mixtures within the simulation time (approximately 0.2 s), which corresponds to a traveled distance of roughly 2 mm at the highest employed flow strength. This distance is smaller than the channel length, and thus we expect that flow-induced separation of star and chain polymers should in principle be possible in experiments.

4.4 CONCLUSIONS

We performed explicit solvent molecular dynamics simulations of single chains, stars, and their mixtures under Poiseuille flow and explored their conformation and cross-stream migration. We found that at infinite dilution, star polymer experienced stronger lift forces to the channel center compared to their linear counterparts with the same equilibrium radius of gyration. By conducting additional simulations without hydrodynamics, we identified wall-induced hydrodynamic lift forces as the mechanism responsible for this lateral motion.

In the star-chain mixtures, we observed an even more pronounced spatial separation of the two species, where the stars occupied the central channel region and the more deformable chains moved closer to the channel walls. In contrast, the flow-induced demixing of star-star mixtures was much less pronounced. In principle, such flow-induced partitioning can be exploited to filter polymers based on their architecture. Our simulations indicate that the spatial separation in the polymer mixtures

stems from a combination of wall-induced hydrodynamic lift forces and viscoelastic forces originating from the linear chains. Hence, the phenomena observed here appear to be more closely related to the viscoelastic focusing of (rigid) colloids than to the deformation induced lift of elastic capsules.

5

JANUS NANOSTRUCTURES FROM ABC/B TRIBLOCK TERPOLYMER BLENDS

5.1 INTRODUCTION

The ability of block copolymers to phase separate into various nanostructures has gained a lot of scientific interest in the past few decades. These nanostructures have uses in diverse applications, from soft matter to material science; in particular, they have a range of nanotechnological applications, including drug delivery [66–69], microreactors *etc*. The phase behavior of AB diblock and ABA triblock copolymers in bulk is very well understood and has applications in the field of energy conversion [155, 156], lithographic mask [157, 158] and photonics [159] *etc*. Lately, triblock terpolymer systems (ABC) have gained interest as they display a much more complex behavior due to the presence of a third chemically distinct block. Due to many interaction parameters, they give access to an extensive library of multicompartment nanostructures [71, 160, 161]. Some of the known geometries of morphologies of ABC triblock terpolymer systems in bulk are spheres, cylinders, lamellae, and gyroids. The lamellar morphologies are of particular interest as they allow access to synthesize Janus nanoparticles by crosslinking the polymer domains [162–165]. One can synthesize Janus sheets, cylinders, or spheres depending on the weight fraction of such domains, and these Janus nanoparticles can be used as colloidal surfactants and in interfacial stabilization applications. Compared to the conventional AB diblock copolymers, a third block adds a higher level of complexity to the design of the self-assembled structures.

Given the complexity of the ternary phase diagram, it is likely that some morphologies remain undiscovered. However, a synthetic variation of block weight fractions and/or monomer chemistry requires considerable experimental effort to explore suit-

able morphologies challenging. In that regard, blending of low molecular weight additives is a convenient tool to alter domain volumes of ABC triblock terpolymers in a continuous manner [166].

In order to understand such complex morphologies, computer simulations are a useful tool. This work is a collaborative effort of experiments as well as simulations. Here, we demonstrate that the blending of specific amounts of the hPB allows the continuous tuning of lamellar bulk morphologies of triblock SBM from PB cylinders to a continuous PB lamella. We first observe a lateral fusion of the PB cylinders into hexagonally perforated PB lamellae before perforations are closed upon further addition of hPB using DPD simulations, observed in the experiments. Further, the simulations reveal that the added hPB is dispersed homogeneously throughout the PB microdomains.

5.2 METHOD AND MATERIALS

5.2.1 *Experimental setup*

Materials: Chloroform was received from VWR in p.a. quality and used as such. Polybutadiene homopolymer (hPB, $M_n \approx 2000\,g\,mol^{-1}$ and $Đ = 1.39$) and sulphur monochloride (98%) were obtained from Sigma Aldrich. Osmium tetroxide (4% aqueous solution) was obtained from Science Services (Munich, Germany). The $S_{40}B_{22}M_{38}$ triblock terpolymer with $M_n \approx 2000\,g\,mol^{-1}$ and $Đ = 1.05$ was synthesized as described elsewhere [81, 82, 167–170].

Preparation of SBM Bulk Films: For bulk film preparation, hPB was first dissolved in $CHCl_3$ to obtain a solution of $20\,g\,L^{-1}$. Then, in a 40 mL glass vial, 50 mg of terpolymer was dissolved in 2 mL $CHCl_3$, mixed with an appropriate amount of homopolymer solution according to Table 1 and stirred for 2 h. The solvent was evaporated over the course of 5 days under constant $CHCl_3$ atmosphere. After film formation, the vial was cooled with liquid nitrogen and the bulk film released by breaking the vial.

Crosslinking of SBM Bulk Films: The bulk films were placed in a glass chamber, and 100 µL S_2Cl_2 was added in a separate container before the chamber was

closed. Crosslinking proceeded via gas-phase overnight. The next day, the films were removed and left for evaporation of excess sulphur monochloride overnight. For the transmission electron microscopy (TEM) measurements, bulk films were cut into ultrathin sections on a Leica EM UC7 ultramicrotome, deposited on a carbon-coated copper grid (200 mesh, Science Services), and stained with OsO_4 vapor for 3 h prior to measurements. If redispersion was desired, the bulk films were dissolved in THF to obtain a concentration of $1\,g\,L^{-1}$, 3 days prior to measurements at least.

Table 1: Amount of added hPB from 0%–100% relatively to the PB block of SBM and resulting composition of the SBM triblock terpolymer.

Code	hPB added[a]	f_S[b]	f_B[b]	f_M[b]	Thickness PB[c]
SBM-0	0	40	22	38	10.9
SBM-10	10	39	24	37	15.0
SBM-25	25	38	26	36	12.8
SBM-50	50	36	30	34	12.6
SBM-75	75	34	33	33	12.9
SBM-100	100	33	36	31	14.6

[a] amount of hPB added in (%) with respect to PB of SBM; [b] weight fractions of the respective polymer blend in [wt%]; [c] thickness in (nm) according to grey scale analysis

Transmission Electron Microscopy (TEM): The TEM measurements were performed on a JEM-1400 Plus TEM (JEOL, Freising, Germany), operated at an accelerating voltage of 120 kV, a point resolution of 0.38 nm, as well as a line resolution of 0.2 nm. Images were recorded with a 16-bit 4096×4096 pixel CMOS digital camera and processed through the FIJI open-source software package. For sample preparation, one drop of the bulk film solution ($c = 1\,g\,L^{-1}$) was deposited on a carbon-coated copper grid (200 mesh, Science Services). All samples were stained with OsO_4 for 3 h prior to measurements.

5.2.2 *Simulation Model*

In our DPD simulations we used a coarse-grained bead-spring model, where each SBM triblock terpolymer was represented by $N = 40$ spherical beads of diameter

a and unit mass m, connected through harmonic springs. We matched the weight fraction of the individual blocks to the experiments, leading to $N_S = 16$, $N_B = 8$, and $N_M = 16$ beads for the S, B, and M blocks, respectively. Using this level of coarse-graining, each bead has a diameter of $a \approx 2.2\,\mathrm{nm}$ and contained between 35 and 60 monomers depending on the particle type. Thus, each bead effectively represented a coil-like segment of the terpolymer. The effective pair interaction between such coils is rather soft and bounded [119, 171], and therefore we used the typical soft repulsion for the conservative forces, $\mathbf{F}_C$ (simplified version of Equation 76 and 81), between bonded and nonbonded monomers [105]

$$\mathbf{F}_C(r) = \begin{cases} A_{ij}\left(1 - r/a\right)\hat{\mathbf{r}}, & r < a \\ 0, & r \geqslant a\,, \end{cases} \tag{87}$$

where, r is the radial distance between the center of two particles and $\hat{\mathbf{r}}$ is the unit vector connecting them. The parameter A_{ij} controls the maximum repulsion between particles of types i and j (the specific values for A_{ij} are discussed further below and summarized in Table 2. Bonds within a chain are modelled using harmonic springs with force

$$\mathbf{F}_C^B(r) = -k\mathbf{r}\,, \tag{88}$$

with spring constant set to $k = 4k_BT/a^2$ in the reduced simulation units [172].

Table 2: Interaction parameters for the S-M, S-B, and B-M particle pairs.

Interaction pairs	χ	χN	χ_{eff}	A
S-M	0.041	44.82	1.5	30.4
S-B	0.19	192	8.4	54.5
B-M	0.12	130	5.6	44.5

In addition to these conservative forces, the particles are also subject to pairwise dissipative, $\mathbf{F}_D$ (similar to Equation 78), and random forces, $\mathbf{F}_R$ (same as Equation 77), which impart thermal fluctuations and drag while also serving as a thermostat on the DPD particles. The terms are given by

$$\mathbf{F}_D(r) = -\gamma_{ij} w(r)(\hat{\mathbf{r}} \cdot \Delta v)\hat{\mathbf{r}}\,, \tag{89}$$

and

$$\mathbf{F}_R(r) = \sqrt{\gamma_{ij} w(r)}\xi\hat{\mathbf{r}}\,, \tag{90}$$

where, γ_{ij} is the drag coefficient between particles of type i and j, $w(r)$ is a weight function, and Δv is the velocity difference of the particle pairs. The variable ξ is an independent random variable drawn for each particle pair that obeys $\xi(t) = 0$ and $\xi(t)\xi(t') = 2k_B T\delta(t - t')$ to satisfy the fluctuation-dissipation theorem [99]. In this work, we used the same drag coefficient $\gamma_{ij} = \gamma = 4.5$ independent of particle type. For the weight function, we employed the (standard) form

$$w(r) = \begin{cases} \left(1 - r/a\right)^2 \hat{\mathbf{r}}, & r < a \\ 0, & r \geqslant a\,. \end{cases} \tag{91}$$

We chose a particle number density of $\rho = 3\,a^{-3}$ and set the interaction strength between particles of the same type to $A_{ii} = 25$. Note that Groot and Warren have originally determined this parameter combination to match the compressibility of water [105], but since then, this choice has been widely used to model other (incompressible) liquids and polymer melts [172–175]. Groot and Warren have also derived a relationship between A_{ij} and the Flory–Huggins χ parameter [105]

$$A_{ij} = A_{ii} + 3.497\chi\,. \tag{92}$$

In Section 5.3, we discuss how the specific χ values have been obtained. The resulting values for A_{ij} are listed in Table 2. Simulations were conducted in a rectangular box with periodic boundary conditions in all three Cartesian directions. The box dimensions were chosen as $L_x = 40\,a$ and $L_y = L_z = \sqrt{3}L_x/2$, so that a hexagonal arrangement of cylinders fit into the box. The box volume was adjusted for the systems containing homopolymers to maintain a particle number density of $\rho = 3\,a^{-3}$. All polymers were initially placed randomly at positions in the box and the cross interaction was set to $A_{ij} = A_{ii}$ (*i.e.*, $\chi = 0$). Then, A_{ij} was linearly increased to its final value over 5×10^6 steps with a time step $\Delta t = 0.05$. We performed three independent simulations per state point to gather statistics.

5.3 RESULTS AND DISCUSSION

The preparation of bulk films from (SBM/B) blends is outlined in Figure 25 and preparative details are found in the Materials and Methods section. At first, the SBM triblock terpolymer is dissolved in 1 mL $CHCl_3$ ($c_{SBM} = 50\,g\,L^{-1}$), mixed with a suitable amount of hPB solution ($c_{hPB} = 20\,g\,L^{-1}$), and stirred for 3 h to ensure complete mixing of both components. The SBM terpolymer in this study has a weight fraction of $f_{PB} = 22\,wt\%$ and equally-sized outer blocks of PS and PMMA. The amount of added hPB in relation to PB and the resulting weight fractions are summarized in Table 1. Evaporation proceeded in a 40 mL glass vial over the course of five days under constant $CHCl_3$ atmosphere. Upon slow evaporation of $CHCl_3$, the SBM/B blend dried into a solid bulk film, where polymer chains microphase separated into distinct microdomains. Irrespective of the weight fraction, the PB microdomain always remains sandwiched between PS and PMMA lamellae. The bulk film was removed by freezing in liquid nitrogen and breaking the glass vial. Selective crosslinking of PB with sulphur monochloride (S_2Cl_2) vapor fixates the morphology and allows its redispersion in THF. Since PS and PMMA are fully soluble in THF, the bulk film separates into nanoparticles with a crosslinked PB core.

By mixing hPB into the SBM morphology, we increased the volume of the PB microphase (Table 1) and gradually changed its geometry. The triblock terpolymer

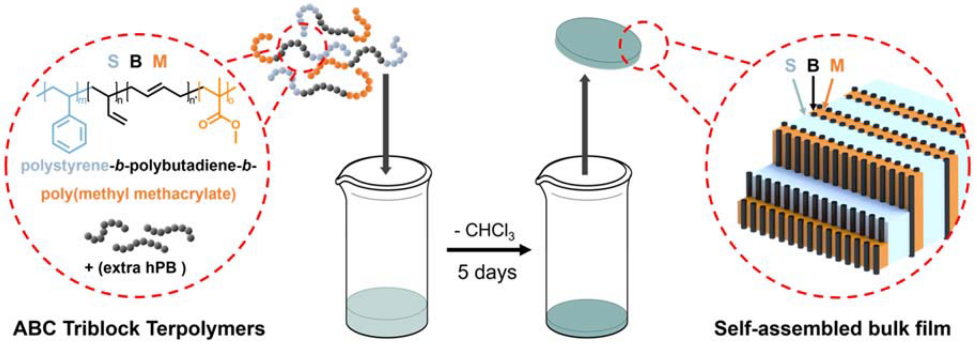

Figure 25: Preparation of SBM/B bulk films. Chemical structure of SBM, casting of the bulk film and lamellar PS/PMMA morphology and varying PB domain depending on polybutadiene homopolymer (hPB) content.

SBM-0 had a molecular weight of $143,000\,\mathrm{g\,mol^{-1}}$ with $Đ = 1.05$ to ensure sufficiently strong microphase separation. The molecular weight of hPB was approximately $M_n \approx 2000\,\mathrm{g\,mol^{-1}}$ to ensure its complete incorporation. The amount of added hPB was calculated relative to the PB microdomain in the SBM terpolymer, *i.e.*, 100% hPB (SBM-100) equals twice the amount of PB in pure SBM-0. As f_{PB} increases, the composition of the terpolymer changes, resulting in equal-sized polymer blocks at 75% hPB (SBM-75). Previous investigations on bulk film structures of SBM resulted in lamellar microphases for similar compositions [168].

To obtain information about the microphase behavior, the bulk films were cut into ultrathin sections and analyzed by TEM imaging. Before cutting, the PB microphases were crosslinked with S_2Cl_2 vapor to enhance the film stability. PB is liquid at room temperature, which softens the film, causing problems when cutting, especially with an increasing amount of added hPB. The TEM images of SBM morphologies are summarized in Figure 26, ranging from 0% (A) to 100% (F) of blended hPB. To enhance their contrast, the films were stained with OsO_4, which bonds covalently to the PB domains causing them to appear dark. After staining, the following three microphases are clearly distinguished: two lamellar microphases, PS and PMMA, separated by an alternating sequence of PB cylinders in between (Figure 26 A). Despite similar weight fractions, the PMMA lamellae appear much thinner than the PS lamellae because PMMA shrinks under e-beam irradiation due to degradation. The PB cylinders appear as black dots when cutting perpendicular to the long axis, whereas they appear as stripes when cut alongside the cylinder axis (both features are seen

at the grain boundary). In certain areas, we find a second morphology, where the PB microphases merge into a mesh-like network, which is the first indication of a morphological transition. The network microstructure is observed more frequently after adding 10 wt% hPB (Figure 26 B, SBM-10). Besides, the hexagonally ordered cylinders merge and could not be distinguished anymore, indicating their coalescence. However, the PB microphase is not completely lamellar, as it does not show homogeneous contrast. This trend does become even more evident at 25 wt% hPB (Figure 26 C, SBM-25), where the PB microphases appear as dotted lines. The grain boundary views this morphology from two sides and is reminiscent of a perforated lamella. Perforated core-shell lamellae have been reported before with a very similar appearance in TEM [176]. In our case, the perforation is formed by the middle block and is thus sandwiched between adjacent PS/PMMA lamellae. Above 50 wt% hPB exclusively lamella-lamella morphologies was obtained (Figure 26 D-F).

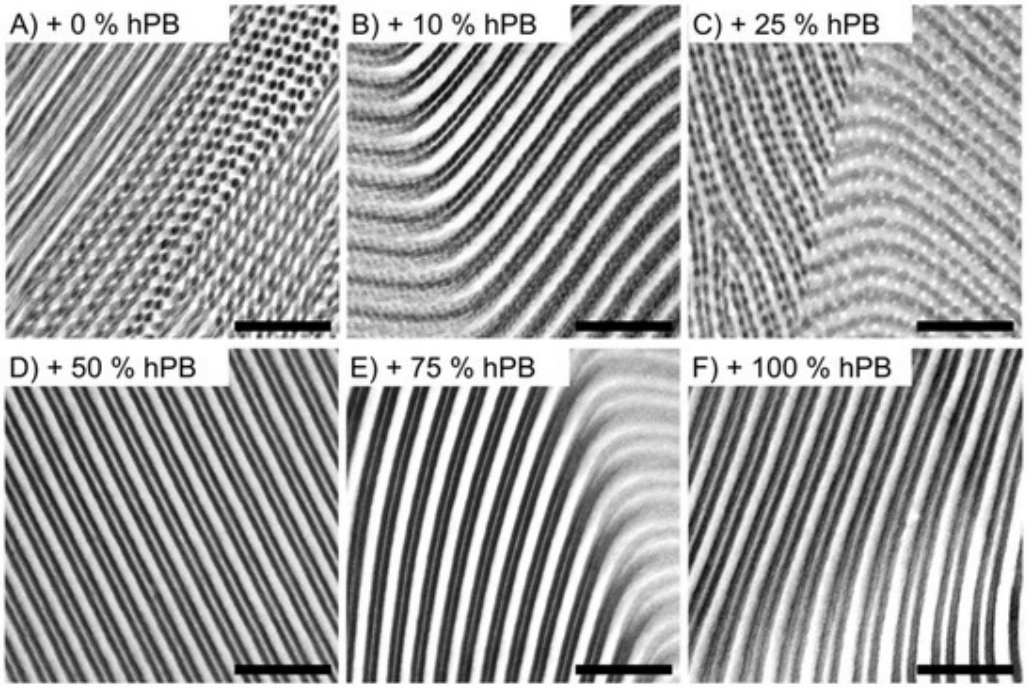

Figure 26: Transmission electron microscopy (TEM) images of bulk morphologies of SBM/B with varying weight fractions of added hPB. TEM images of resulting bulk film from 0% (**A**) to 100% (**F**) hPB in relation to PB domain in SBM. (All samples were stained with OsO_4 to enhance the contrast of PB, scale bars are 200 nm).

Naturally, the thickness of PB domains increases with respect to the amount of additional hPB, measured by greyscale analysis as summarized in Table 1. The PB

thickness increases from approximately 11 nm (SBM-0) to 15 nm (SBM-10) when an amount of hPB up to 10 wt% is added. We attribute this increase in thickness to the swelling of the cylinders with hPB. At 25 wt%, the thickness decreases again to ca. 12.8 nm (SBM-25) because the cylinders merge laterally into the perforated mesh causing redistribution of the cylinder volume across a larger two-dimensional (2D) area between the PS/PMMA lamellae. Further addition of hPB does not seem to have an effect on the thickness that remains approximately the same with 12.6 nm at 50 wt% hPB (SBM-50) and 12.9 nm at 75 wt% hPB (SBM-75). The added hPB does not contribute to the thickness because it is distributed within the PB microphase, filling the perforations of the 2D perforated lamella leading to a complete PB lamella. After complete filling, the thickness increases again reaching a maximum of 15 nm at 100 wt% hPB (SBM-100). It should be pointed out that the cutting process always leads to film deformation. Polymer domains, therefore, may appear distorted in some areas so that high precision in greyscale analysis is demanded. Values of PB thickness might, therefore, not be completely accurate in total, however, they are applicable to make statements about morphological changes.

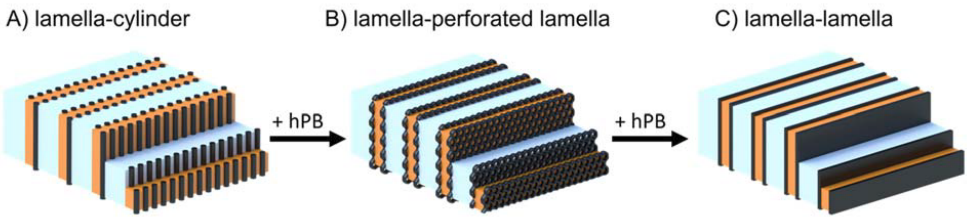

Figure 27: Schematics of SBM/B bulk morphologies with increasing hPB content.

The overall process of PB middle phase transition is outlined schematically in Figure 27. In general, we start with hexagonally stacked cylinders that are not connected to each other, also known as the lamellar-cylinder morphology. By adding hPB, the cylinders first increase in volume before they merge into a perforated network, spreading between PS and PMMA layers, *i.e.*, they form a lamella-perforated lamella morphology. This network is then transformed into a continuous PB lamella upon the further blending of hPB into the SBM morphology. We believe that the perforated PB lamellae always form between the PS/PMMA lamella and are not connected to adjacent PB layers (*e.g.*, by interpenetrating networks), which is confirmed by our sim-

ulations where the PB layers are always well separated from each other (see below). This will be important for the separation of crosslinked layers, as discussed later.

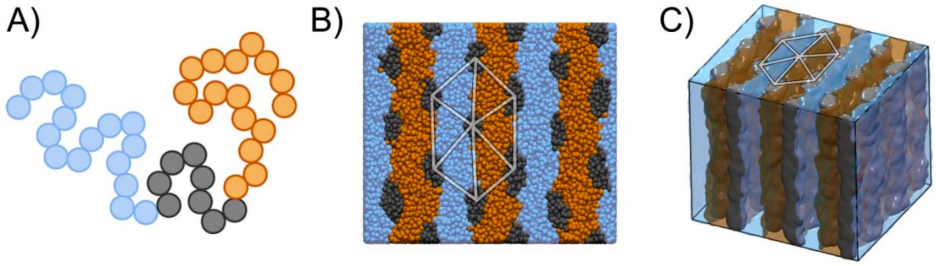

Figure 28: Dissipative particle dynamics (DPD) simulations of an SBM triblock terpolymer melt. (**A**) Schematic representation of the SBM triblock terpolymer used in the DPD simulations. The S, B, and M beads are shown in blue, grey, and orange, respectively. (**B**) Top view showing the lamellar ordering of the PS and PMMA blocks, and the hexagonal arrangement of the cylinders formed by the PB block. (**C**) Three-dimensional view of the simulation box. The white lines in (b) and (c) illustrate the hexagonal ordering of the cylinders. All simulation snapshots have been rendered using visual molecular dynamics [177].

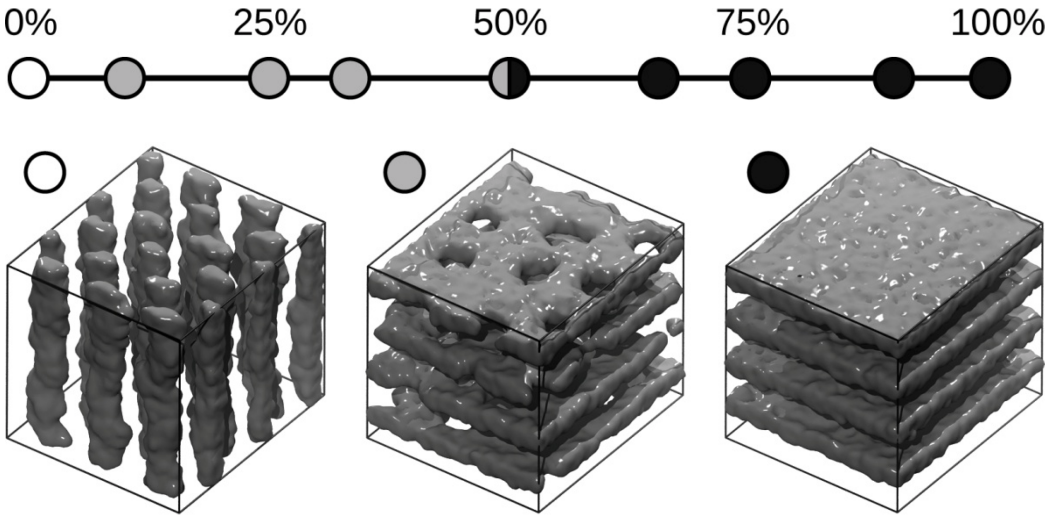

Figure 29: Morphology of the PB microphase as a function of hPB fraction. The PS and PMMA blocks form lamellae in all cases, and they have been omitted for clarity. The symbols indicate results at $\phi = 0\%$, 10%, 25%, 33%, 50%, 66%, 75%, 90%, and 100%. The snapshots show typical configurations of cylinder, perforated lamella, and lamella structures at $\phi = 0\%$, 33%, and 90%, respectively.

The discussed morphological transitions were also found in our DPD simulations, as shown by the simulation snapshots in Figure 28 and Figure 29. In order to replicate accurately the experimental systems, we first determined the Flory–Huggins interaction parameters, χ. For the S–M interactions, we used the expression for χ obtained for SM diblock copolymers via small-angle neutron scattering experiments,

$\chi_{SM} = 0.028 + 3.9/T$, leading to a value of $\chi_{SM} = 0.041$ at room temperature ($T = 298\,K$). For the S-B interactions, we used the expression for χ extracted from the small-angle x-ray scattering analysis of concentration fluctuations in S-B mixtures [178] $\chi_{SB} = 6.96 \times 10^5/T^{2.65}$, resulting in a value of $\chi_{SB} = 0.19$ at room temperature. We were unable to find literature data for the χ parameter for the B-M interactions, and therefore estimated χ_{BM} using the Hildebrand–Scott relation,

$$\chi_{ij} \approx (V_i V_j)^{1/2}(\delta_i - \delta_j)^2/RT. \tag{93}$$

Here, δ_i and δ_j are the Hildebrand solubility parameters, V_i and V_j are the molar volumes of molecules i and j, respectively; and R is the ideal gas constant. Using $\delta_B = 8.31\,cal^{1/2}cm^2$ and $V_B = 59.7\,cm^3\,mol^{-1}$ for B in combination with $\delta_M = 9.29\,cal^{1/2}cm^2$ and $V_M = 87.1\,cm^3\,mol^{-1}$ for M, we find $\chi_{BM} = 0.12$. Note that these χ parameters should not be directly used in the simulations, since in our model, multiple monomers are grouped into a single bead. To account for this mapping, we employed a scaled interaction parameter χ_{eff} in the simulations to reach the same χN values as in the experiments. Table 2 shows a summary of the interaction parameters.

The molecular weight of the used hPB is approximately $M_n = 2000\,g\,mol^{-1}$, which translates to a chain length of $N_{hPB} \approx 0.6$, for our level of coarse-graining. Such a non-integer value for N_{hPB} is, however, unphysical, and therefore we used $N_{hPB} = 1$ in our simulations, *i.e.*, each hPB is represented by a single bead. This choice has two consequences: (i) The hPB in the simulations corresponds to somewhat longer homopolymers than used in the experiments, and, more importantly, (ii) the simulated hPB lack conformational degrees of freedom. However, given the rather low molecular weight of the hPB as compared with the SBM terpolymer, we expect that the conformational details of the homopolymers are negligible. Figure 28 B and C show results for the pure SBM system, where the PS and PMMA blocks self-assemble into lamellae (blue and orange), while the PB blocks form hexagonally arranged cylinders (grey) located at the interfaces between the PS and PMMA domains. We estimate a domain spacing of $D_L \approx 29\,nm$ for the lamella, and $D_C \approx 25\,nm$ for the triangular lat-

tice of the cylinders, which is in almost quantitative agreement with the experimental finding ($D_L \approx 32\,nm$, $D_C \approx 26\,nm$). Looking closer at the cross-sections of the cylinders, it appears that they are not perfectly circular but somewhat compressed along the direction perpendicular to the lamellae. Such a slight ellipsoidal deformation of the PB cylinder has also been observed in the experiments (cf. Figure 26 A), and it might originate from the asymmetry between the S-B and B-M interactions (see Table 2) which leads to asymmetric interfacial tensions.

We next studied the microphase behavior upon adding hPB to the system (Figure 29). Here, we varied the amount of hPB in the melt from $\phi = 0\%$ to $\phi = 100\%$, where a value of $\phi = 100\%$ indicates that there is the same amount of PB in the system in the form of homopolymer and terpolymer (corresponding to SBM-100). For all investigated cases, the PS and PMMA blocks formed lamellae, but the morphology of the PB blocks changed. For $10 \leqslant \phi = 0\% \leqslant 33\%$, the PB blocks microphase separated into perforated lamellae, which became thicker and less porous with increasing ϕ. At $\phi = 50\%$, we observed a transition from perforated lamellae to lamellae. For the remaining investigated cases, $66 \leqslant \phi = 0\% \leqslant 100\%$, we always found lamellar structures, where the thickness of the PB lamellae increased by roughly $\phi = 15\%$ with increasing ϕ, as also observed in the experiments (cf. Table 1).

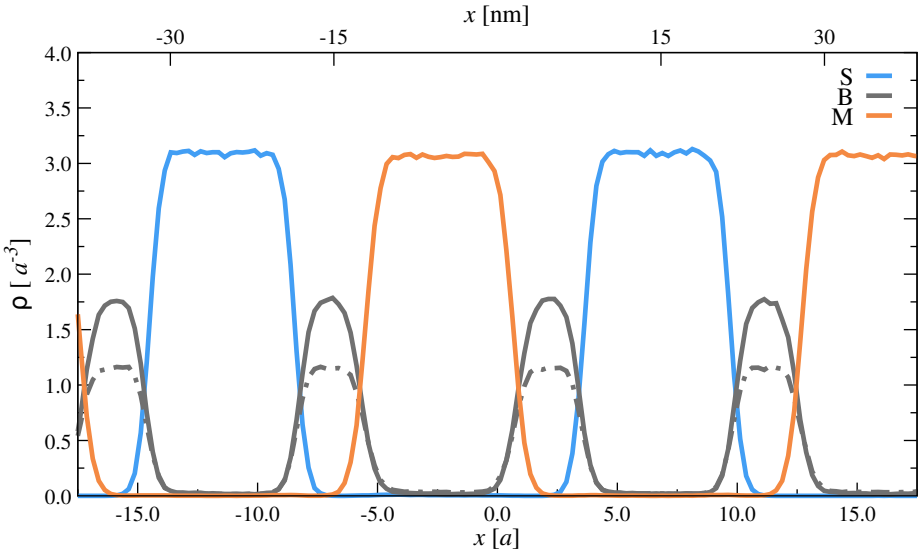

Figure 30: Monomer density distribution of SBM terpolymer (solid lines) with $\phi = 75\%$ hPB (dashed line) in the lamellar phase. The x-axis lies perpendicular, relative to the lamellae.

We also investigated the distribution of hPB in the system and found that the homopolymers are uniformly distributed in the PB microphase for all investigated ϕ values. Figure 30 shows, for example, the monomer number density for a lamellar system with $\phi = 75\%$ perpendicular to the lamellae, highlighting the clear separation between PS and PMMA microdomains through interstitial PB layers. These PB lamellae consist of PB blocks from SBM terpolymers and hPB, where the local number (or volume) fraction of the two contributions are close to the global fraction, ϕ.

To further quantify the distribution of hPB in the system, we computed the radial pair distribution function, $g(r)$, for S-B, M-B, and B-B monomer pairs, distinguishing B monomers from terpolymers and homopolymers. For all investigated cases, the radial pair distributions were virtually indistinguishable with respect to the different sources of B monomers in the system, as shown in Figure 31 for the exemplary case $\phi = 75\%$. Further, the $g(r)$ data for the S-B and S-M pairs are very close to each other (Figure 31 A, B), which is due to the similar χ values for these two pairs. There are some small but notable differences for the B-B data (Figure 31 C) at small interparticle distances, r, which originate from the correlations between bonded B monomers in the SBM terpolymers.

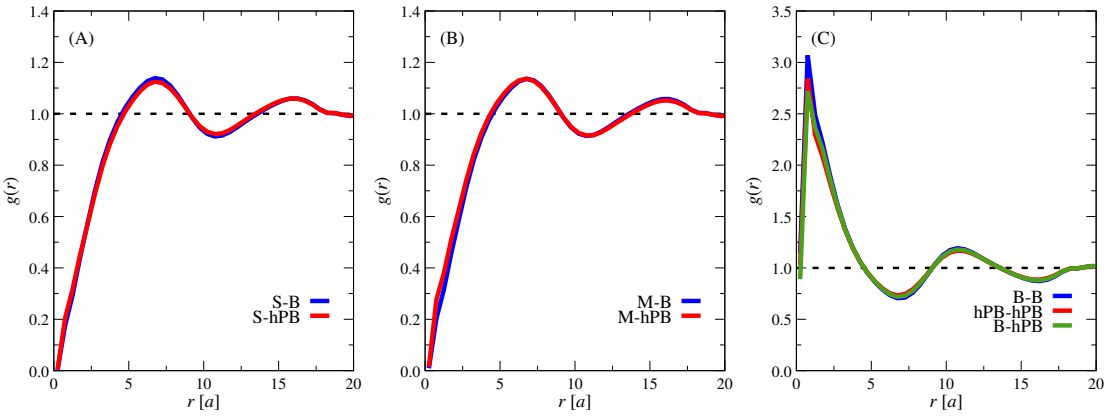

Figure 31: Radial pair distribution function, $g(r)$, between S, B, and M monomers in the system for $\phi = 75\%$ hPB.

Finally, we crosslinked the PB domains of the bulk morphologies and redispersed them in a good solvent for all three blocks (THF) to analyze the resulting nanostructures. Crosslinking the PB domain fixes the microdomain geometry, while the PS and PMMA outer chains are covalently anchored to the PB core and stabilize discrete

nanostructures when exposed to the solvent. All obtained structures have a Janus character, *i.e.*, PS and PMMA are separated from each other on two distinct sides of the nanoparticles. Figure 32 A exemplifies crosslinking and separating of lamella-perforated lamella morphologies into perforated Janus sheets to underline that PS and PMMA polymer chains are connected to the PB network but are completely separated from each other. The TEM results of the nanostructures are summarized in Figure 32 B-E. Starting with SBM-0, Figure 32 B shows Janus cylinders that originate from the lamella-cylinder morphology. The cylinders are several micrometers in length which underline the long-range order within the grain. The Janus character is clearly seen from the assembly behavior, *i.e.*, the cylinders align alongside their PS hemisphere as visible from the grey contrast between the dark cylinder cores.

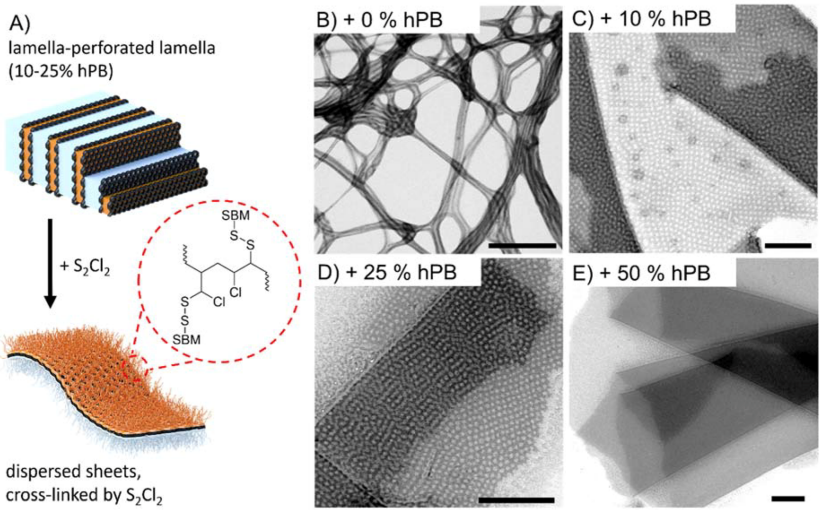

Figure 32: Crosslinking and redispersion of SBM/B morphologies into Janus nanostructures. (**A**) Schematic of lamella-perforated lamella morphology and perforated Janus sheets after crosslinking. (**B–E**) TEM images of crosslinked Janus nanostructures, redispersed in THF.

At $\phi = 10\%$ and $\phi = 25\%$ we find monolayer sheets with relatively uniform perforations (Figure 32 C, D). The pores have an average diameter of $d_p \approx 20\,\text{nm}$ that are separated by $16 \pm 4\,\text{nm}$ of PB membrane, which corresponds roughly to the diameter of the PB cylinders (supporting the assumption of merging cylinders). Monolayer sheets underline our assumption that the added hPB is distributed between the cylinders and did not penetrate through adjacent PS and PMMA lamellae to form a bicontinuous morphology. Although the sheets are not connected with each other,

the sheets overlap on the TEM grid or roll up (darker areas). Similar nanostructures were observed before for terpolymer-based core shell nanosheets of polybutadiene-*b*-poly(2-vinylpyridine)-*b*-poly(tert-butyl methacrylate) [176] and blending of hPB into polybutadiene-*b*-poly(tert-butyl methacrylate)-*b*-poly(2-(dimethyl-amino)ethyl methacrylate) [179]. The perforated lamella in the previous reports had a core-shell-corona character and tetragonally ordered perforations, while in our case, the sheets have a Janus character, and pores are likely in a hexagonal order (Figure 32 D). The fast Fourier transformation of larger areas gives a hexagonal scatter pattern, and areas of overlapping sheets produce a pattern that is characteristic for structures with overlapping hexagonal features. Above $\phi = 50\%$ hPB, sheets with homogenous contrast are found, which agrees well with our previous results from bulk film analysis, as well as our simulations (Figure 32 E).

5.4 CONCLUSIONS

We demonstrated that blending of B homopolymer into lamella morphologies of ABC triblock terpolymers is a promising route for tuning the B microphase. DPD simulations and experiments were in very good agreement regarding observed morphologies as well as morphological transitions. This combined approach helped to gain valuable insight into the formation and stability of sandwiched microphases and offers guidelines to target specific morphologies for other ABC/B terpolymer blends. The formation of perforated Janus sheets is of particular interest, as BCPs have demonstrated to be a versatile and scalable source for isoporous membranes [180, 181]. Due to the uniform porosity, BCP membranes have successfully been applied in water purification, as the nanometer-sized holes are suitable to withhold the smallest impurities [182, 183]. Janus membranes have likewise generated considerable interest in recent years due to their application in selective separation [184]. The presented perforated nanosheets have pore sizes of about 20nm, Janus character, and are flexible, which will allow studies on directional adsorption to interfaces and selective separation of nanoparticles or molecules depending on chemistry. We believe

that the presented blending route will give access to a vast library of perforated Janus nanosheets with tuneable properties depending on the used ABC triblock terpolymer.

6

CONTROLLING JANUS NANODISC TOPOLOGY THROUGH ABC TRIBLOCK TERPOLYMER/HOMOPOLYMER BLENDING IN 3D CONFINEMENT

6.1 INTRODUCTION

The confinement assembly of ABC triblock terpolymers was identified as a promising route to prepare multicompartment microparticles [185–189] as well as Janus nanoparticles (JNPs) with unprecedented shapes such as Janus nanorings [190] and nanocups. For instance, SBM triblock terpolymers with $\phi_{PB} < 20$wt% and equally sized end blocks formed an axially stacked lamellar-ring morphology that, after crosslinking of the PB microdomain, resulted in ring-shaped colloids with a PS brush on the one side and a PMMA brush on the other [190]. However, at $\phi_{PB} < 20$wt%, we observed irregular PB patterns filling the rings, suggesting coalescence of neighboring rings. The PB microdomains experience double confinement, *i.e.*, by the spherical emulsion droplet as well as the adjacent PS and PMMA lamellae, which could lead to a more complex microphase behavior than previously thought. We, therefore, sought to investigate these systems in more detail with experiments and simulations to explore the evolution of the PB microphase and resulting JNP shapes.

In this work, we demonstrate that SBM triblock terpolymers with specific amounts of hPB in the confinement of microemulsion droplets are an efficient route to produce Janus nanodiscs with a variety of morphologies from a single type of triblock terpolymer. The Self-assembly of the SBM triblock terpolymers forms prolate microparticles with S/M lamellae stacked along the particle's major axis with sandwiched B microphase. The morphology of the B microphase is gradually tuned in between the S/M lamellae by blending B homopolymer during microphase separation. Along with the morphological transition, we rationalized the microparticle stability.

6.2 METHOD AND MATERIALS

6.2.1 *Experimental Setup*

Materials: All chemicals were used as received unless stated otherwise. Chloroform ($CHCl_3$), and tetrahydrofuran (THF) were received from Merck in p.a. quality. Sodium dodecyl sulfate (SDS, $> 99\%$) and polybutadiene homopolymer (hPB, $M_n = 2000\,g\,mol^{-1}$ and $Đ = 1.39$) were received from Sigma-Aldrich. Osmium tetroxide (4% aqueous solution) was obtained from Science Services. Ultrapure water from a Milli-Q Integral Water Purification System was used for the preparation of emulsions and for purification. The dialysis tube of regenerated cellulose had an average flat width of 33 mm and a MWCO of $12-14$ kDa (Sigma Aldrich). The $S_{40}B_{22}M_{38}$ triblock terpolymer (subscripts denote the block fractions in wt%) with $M_n = 143000\,g\,mol^{-1}$ and $Đ = 1.05$ was synthesized following an established recipe [167].

Preparation of SBM Emulsion Droplets: SBM and hPB were dissolved in $CHCl_3$ to obtain stock solutions with concentrations of $c_{SBM} = 10\,g\,L^{-1}$ and $c_{hPB} = 20\,g\,L^{-1}$. Both solutions were mixed in suitable ratios and stirred for 3 h prior to emulsification. Emulsification was done by passing 10 mL of the polymer mixture into 150 mL of an aqueous SDS solution ($c_{SDS} = 5\,g\,L^{-1}$) using a Shirasu Porous Glass (SPG) membrane with a pore size of $0.6\,\mu m$ while stirring at 250 rpm. Constant nitrogen pressure was applied. The organic phase was evaporated over 5 days at room temperature (RT). After evaporation, microparticles were purified from excess SDS by dialysis against Milli-Q water and diluted to a concentration of $2\,g\,L^{-1}$. Samples remained stable for several months.

Cross-Linking of PB Domains: To 2 mL of the purified microparticle dispersion $25.5\,\mu L$ of a 4% aqueous OsO_4 solution was added per 1 mg of microparticles. The dispersion was stirred at RT for 2 h with a closed cap, before the cap was removed and the solution was stirred overnight. The crosslinked microparticles were purified by three centrifugation cycles (600 rpm, 20 min) and redispersion in Milli Q water. At last, the microparticles were redispersed in THF and nanoparticles stored at a concentration of $0.5\,g\,L^{-1}$.

Solvent Absorption Annealing: Into a 40 mL glass vial containing 2 mL of $CHCl_3$, a smaller vial containing 2 mL of microparticle dispersion ($c = 2\,g\,L^{-1}$) was placed so that both solutions were separated. The 40 mL vial was closed, and the polymer dispersion stirred under elevated temperatures of 45°C overnight. Afterwards, it was removed from the 40 mL vial and stirred openly at RT overnight.

Platinum Loading: Imaging was performed in air using a Bruker Dimension Icon with NanoScope V controller in tapping mode using RTESPA cantilevers (nom. $f_0 = 256 - 326\,kHz$, $k_C = 20 - 80\,N\,m^{-1}$, tip radius $r_{Tip} = 10\,nM$, Bruker) and in PeakForce QNM mode using SAA-HPI-SS cantilevers (nom. $f_{Res} = 55\,kHz$, $k_C = 0.25\,N\,m^{-1}$, tip radius $r_{Tip} = 1 - 2\,nm$, Bruker) for higher resolution measurements. AFM specimens were prepared by spin-coating a drop of the crosslinked nanoparticle solution ($0.5\,g\,L^{-1}$ in THF) on freshly cleaned (ethanol p.a.) pieces of silicon wafer ($10 \times 10\,mm^2$) with an in-house built spin-coater at 3200 rpm for 5 s. Images were processed with Bruker's NanoScopeAnalysis software (version 1.9). The presented images were processed by 1st order plane fit.

Atomic Force Microscopy (AFM): Measurements were performed on an LS spectrometer operating with a Cobolt laser (max. 100 mW constant power output at $\lambda = 660\,nm$). At concentrations of $0.1\,g\,L^{-1}$, samples were prepared and purified from dust by passing through a PTFE filter with 5 µm pore size directly into dust-free cylindrical quartz cuvettes ($d = 10\,mm$). Three intensity-time autocorrelation functions were measured at a scattering angle of 90° and an acquisition time of 60 s. Recorded data were analyzed with the LS spectrometer v.63 software package.

Transmission Electron Microscopy (TEM): Measurements were done on a JEOL JEM-1400 Plus TEM, operating at an accelerating voltage of 120 kV, a point resolution of 0.38 nm as well as a line resolution of 0.2 nm. Images were recorded with a 16 bit 4096×4096 Pixel CMOS digital camera and processed with the FIJI open-source software package [191]. Samples were prepared by depositing one drop of microparticle dispersion ($c = 2\,g\,L^{-1}$ or $c = 0.5\,g\,L^{-1}$) onto a carbon-coated copper grid (200 mesh, Science Services) and excess solution was blotted after 30 s using filter paper. Microparticle samples were stained with OsO_4 for 3 h prior to measurements.

Scanning Electron Microscopy (SEM): Measurements were performed on a cryo-field emission SEM equipped with in lens-, chamber- as well as energy-selective detectors for 16-bit image series acquisition with up to $40,000 \times 50,000-$ pixel resolution. Samples were prepared by putting one drop of an approximately $2.0\,\mathrm{g\,L^{-1}}$ sample dispersion on a mica wafer. After 30 s, the solution was blotted with filter paper, and the wafer was dried for at least 12 h. Afterward, a layer of 2 nm was sputtered on the samples using a Quorum PP3010T-Cryo chamber with integrated Q150T-Es high-end sputter coater and Pt-Cd target.

6.2.2 *Simulation Model*

We performed dissipative particle dynamics (DPD) simulations [98, 99, 105] of coarse-grained polymers in an explicit solvent. The SBM terpolymers were modeled as bead-spring chains, consisting of $N = 38$ spherical beads with diameter a and mass m. Mapping the simulated chains to the experimental SBM terpolymers with $M_n = 143\,\mathrm{kg\,mol^{-1}}$ leads to $a \approx 2.3\,\mathrm{nm}$, so that each bead effectively represented 35 to 60 monomers depending on the polymer type [192]. At this level of detail, hPB chains ($M_n = 2\,\mathrm{kg\,mol^{-1}}$) and solvent molecules were represented as single beads. Surfactant molecules were not modeled explicitly, but their effect was included implicitly through the polymer-solvent interaction. Thus, our simulations contained five different bead types, *i.e.*, S, B, M, C (for $CHCl_3$), and W (for water). Non-bonded interactions between any pair of particles were modeled using a soft repulsion

$$\mathbf{f}_m(r) = \begin{cases} A_{ij}(1 - r/a)\hat{\mathbf{r}}, & r \leqslant a \\ 0, & r > a\,, \end{cases} \tag{94}$$

where r is the distance between the two particles, and $\hat{\mathbf{r}}$ is the unit vector connecting the two. The parameter A_{ij} sets the strength of the repulsion between particles of type i and j, and the employed values are discussed further below.

Polymer bonds were modeled through harmonic springs with force

$$\mathbf{f}_b(r) = -k\mathbf{r}\,, \tag{95}$$

with spring constant $k = 4\,k_B T/a^2$ used for all polymer types [172].

In addition to these two conservative forces, particles were also subject to pairwise dissipative and random forces given by

$$\mathbf{f}_d(r) = -\gamma_{ij}\omega(r)\,(\hat{r}\cdot\Delta\mathbf{v})\,\hat{r}\,, \tag{96}$$

$$\mathbf{f}_r(r) = \sqrt{\gamma_{ij}\omega(r)}\xi\hat{r}\,, \tag{97}$$

with drag coefficient γ_{ij}, weight function $\omega(r)$, and velocity difference between the two particles $\Delta\mathbf{v}$. The parameter ξ is a uniformly distributed random number drawn for each particle pair, with zero mean $\langle\xi(t)\rangle = 0$ and variance $\langle\xi(t)\xi(t')\rangle = 2k_B T\delta(t-t')$ to satisfy the fluctuation-dissipation theorem. For simplicity, we used the same drag coefficient $\gamma_{ij} = \gamma = 4.5\sqrt{mk_B T}/a$ for all particles. Further, we used the standard DPD weight function[105]

$$\omega(r) = \begin{cases} (1-r/a)^2, & r \leqslant a \\ 0, & r > a\,. \end{cases} \tag{98}$$

The particle number density was set to $\rho = 3\,a^{-3}$ and the interaction strength between particles of the same type to $A_{ii} = 25\,k_B T/a$ [105]. The cross-interaction parameters A_{ij} were determined *v*ia the (empirical) expression[105]

$$A_{ij} = A_{ii} + 3.497\chi\,. \tag{99}$$

Note that the experimental χ interaction parameters should not be used directly in Eq. (99) because the coarse-grained polymer beads contain multiple monomers. We can account for this mapping by introducing an effective interaction parameter χ_{eff} that leads to the same χN values as in the experiments. We have summarized the employed interaction parameters in Table 3, and provided a brief discussion on how those values were obtained in Section 6.3.

We estimated the volume fractions of the S, B, and M blocks in the experimental terpolymers as $\phi_S \approx 0.40$, $\phi_B \approx 0.25$, and $\phi_M \approx 0.35$, respectively, and therefore initially used $N_S = 15$, $N_B = 10$, and $N_M = 13$ beads for the corresponding terpolymer blocks in the simulations (noting that there is no distinction between number and volume fraction in our model). With this choice, however, we observed slightly different morphologies of the PB block in the simulations and experiments, *e*.g., perforated lamellae *vs.* concentric rings at $\phi_{hPB} = 0$. We surmise that this mismatch originated from the rather coarse-grained nature of our model, where tens of monomers are lumped into a single bead, and the only difference between the polymer types is their mutual cross-interaction parameter A_{ij}. Because we are primarily interested in the self-assembled structures, we slightly adjusted the composition of the simulated polymers to $N_S = 17$, $N_B = 5$, $N_M = 16$, resulting in morphologies much closer to the experiments.

Simulations were conducted in cubic simulation boxes with an edge length of $100\,a$ and periodic boundary conditions applied to all Cartesian directions. Initial configurations were created by placing 9,474 chains at random positions inside the simulation box. The box was then filled with solvent particles (initially all of type C) until the desired particle number density $\rho = 3\,a^{-3}$ was reached. For simulations with hPB, the box volume was adjusted accordingly to maintain $\rho = 3\,a^{-3}$. The equations of motion were integrated using the velocity Verlet algorithm with a time step of $\Delta t = 0.05\,\tau$, with intrinsic unit of time $\tau = \sqrt{m a^2/(k_B T)}$. To mimic the change in solvent quality during evaporation, we gradually increased the monomer-solvent interactions from $A_{iC} = 25\,k_B T/a$ to their final values $A_{iW} = 120\,k_B T/a$ over a period of $\tau_{mix} = 2.5 \times 10^4\,\tau$. All simulations were performed using HOOMD-blue (v. 2.5.1) on graphics processing units.[135, 136, 193]

6.3 RESULT AND DISCUSSION

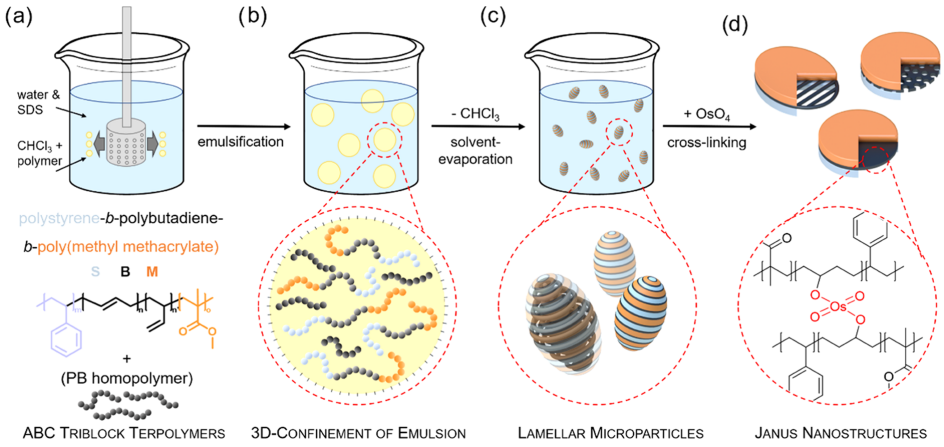

Figure 33: Preparation of SBM microparticles. (**a**) SPG membrane emulsification process and chemical structure of SBM. (**b**) Microemulsion with $CHCl_3$ droplets containing the polymer chains, stabilized in aqueous SDS surfactant solution (**c**) Microparticles after solvent evaporation with stacked lamella morphology. (**d**) OsO_4 crosslinked Janus nanodiscs dispersed in THF.

General Preparation: The preparation of multicompartment microparticles and JNPs thereof is outlined in Figure 33 . First, stock solutions of $S_{40}B_{22}M_{38}$ (M_n = 143,000 g mol^{-1}) and hPB (M_n = 2000 g mol^{-1}) were prepared separately in chloroform ($CHCl_3$) with concentrations of $c_{SBM} = 10\,g\,L^{-1}$ and $c_{hPB} = 20\,g\,L^{-1}$, respectively. Both solutions were mixed in varying amounts and equilibrated overnight. Oil-in-water nanoemulsions were prepared by passing the polymer mixture with nitrogen pressure through a SPG membrane with a pore diameter of $D_{pore} = 0.6\,\mu m$ into an aqueous SDS solution with $c_{SDS} = 5\,g\,L^{-1}$ (Figure 33 a, b). Evaporation of $CHCl_3$ from the emulsion droplets resulted in solid SBM microparticles stabilized by SDS in water. During evaporation, the volume of the emulsion droplets decreased continuously inducing microphase separation of the initially dissolved terpolymer chains into morphologies according to their block volume fractions (Figure 33 b, c). The equally-sized endblocks of PS and PMMA formed axially stacked lamellae, while the PB middle block was sandwiched between this two-dimensional confinement; each PB layer was strictly separated from neighboring PB layers. Due to the incompatibility of PB with PS and PMMA (Table 3), we assumed that the added hPB preferentially accumulated in these PB layers and increased their volume, thereby al-

lowing to tune the microparticle morphology. Through selective crosslinking of PB with OsO_4 (4 wt% aqueous solution), the PB morphology was fixed and the microparticles were separated via redispersion in THF into individual JNPs with a PB core and PS/PMMA surface. The resulting JNPs then exhibited various shapes depending on the overall PB content (Figure 33 d).

Table 3: Flory-Huggins interaction parameters χ_{ij}, and interfacial tension γ_{ij} for the polymer pairs employed in this work.

	PS-PB	PS-PMMA	PB-PMMA
χ_{ij}	0.193[194]	0.041[178]	0.116
γ_{ij} (mN/m)	3.3 [195]	3.3 [196]	3.1

Control of Particle Size and Shape with Membrane Emulsification: We start by identifying suitable emulsification parameters to obtain homogeneous microparticle populations. A narrow size distribution is desirable, as confinement effects will be identical for equally sized microparticles, which is more likely to produce homogeneous morphologies and nanoparticles after crosslinking. Although the defined pore size of the SPG membrane was reported to produce narrowly dispersed microparticles for AB diblock copolymer [197], it was unclear whether this method would also be suitable to fabricate microparticles of SBM triblock terpolymers or SBM/hPB blends. In fact, we found that nanoemulsions using toluene, a frequently utilized solvent, exclusively resulted in spherical SBM microparticles with a concentric, onion-like morphology irrespective of evaporation rate, and concentrations c_{SBM} and c_{SDS}. However, using $CHCl_3$ as the volatile oil phase directly resulted in prolate ellipsoidal SBM microparticles with an aspect ratio of $\alpha \approx 2$ and axially-stacked lamellae. Figure 34 a, b shows TEM and SEM overview images of the obtained microparticles. TEM samples were stained with osmium tetroxide (OsO_4 (4 wt% in water) to enhance the contrast of the PB microdomain. The PS and PMMA end blocks are close to equal in size with $\phi_{PS} \approx 40$ vol% and $\phi_{PS} \approx 35$ vol% , promoting the formation of PS/PMMA lamellae. During imaging, the PMMA blocks shrink due to the e-beam damage, which reduces the PMMA lamella's thickness compared to the PS lamella. Based on the initial polymer concentration and the final microparticle size, we esti-

mated the diameter of the emulsified droplets D to be about 3.3 times larger than the pore diameter D_{pore} . This ratio is in good agreement with previous experiments that reported $D/D_{pore} \approx 3.6$ [197, 198]. In our simulations, we also found prolate microparticles with a similar aspect ratio α and stacked lamellar morphology (see inset of Figure 34 c).

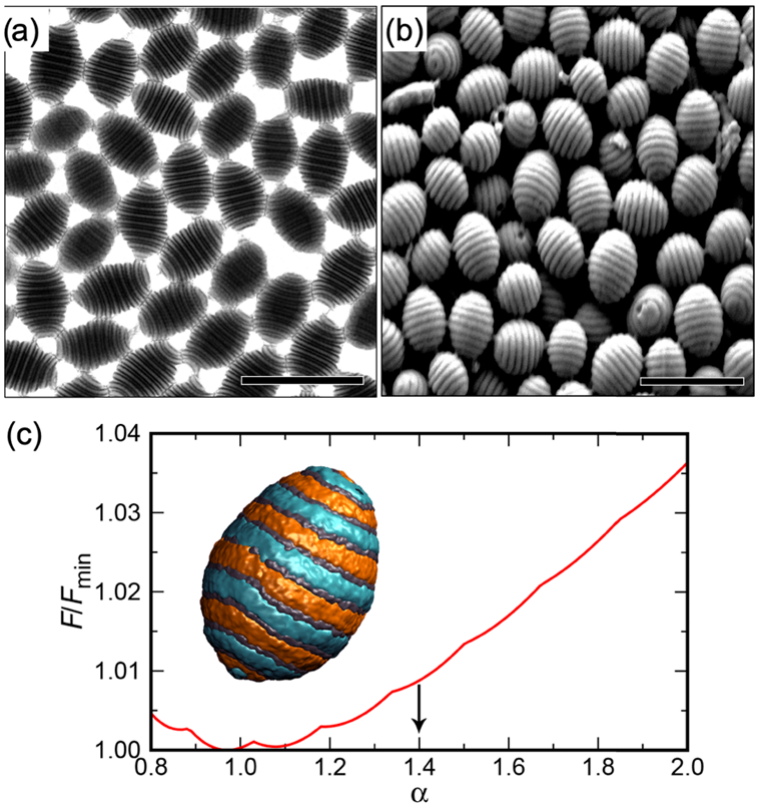

Figure 34: SBM microparticles prepared with the SPG membrane. (**a**) TEM and (**b**) SEM overview images of narrowly dispersed ellipsoidal microparticles (scale bars are 1 µm). (**c**) Free energy of a microparticle F, reduced by its minimum energy Fmin, as a function of the aspect ratio α. The inset shows a typical prolate SBM microparticle from our DPD simulations (color code as in Figure 33).

The droplet size and evaporation rate play an important role in the shape of the final microparticle and the orientation of the internal morphology; in slowly evaporating droplets, the self-assembled microdomains (and their constituent polymers) have sufficient time to relax and rearrange towards their equilibrium configuration, whereas for fast evaporation, the microdomains could become trapped in long-lived metastable states. Typically, the drying regime can be classified through the Péclet number, which is defined as the ratio of the characteristic diffusion and evaporation times. The evaporation time can be measured easily in experiments or estimated the-

oretically for (spherical) droplets [199, 200], but it is more challenging to accurately identify the relevant diffusive timescales for microphase separating BCPs [201]. To determine whether the final microparticles and internal morphologies are in true equilibrium, samples were annealed with $CHCl_3$ vapor. The lamellar morphology remained, while the aspect ratio of the particles slightly decreased.

This shape deformation towards spherical microparticles suggests that the prolate ellipsoids are indeed metastable, which is corroborated by the theoretically estimated free energy of the microparticles: In the limit of strong segregation, an assumption that is validated by our estimates of $\chi_{ij}N_{ij}$ (see Table 3), the free energy of a microparticle can be expressed as,

$$\mathbf{F} = \mathbf{F}_{srf} + \mathbf{F}_{int} + \mathbf{F}_{str}, \tag{100}$$

where $\mathbf{F}_{srf}$ represents the interfacial energy between the microparticle and the surrounding medium, $\mathbf{F}_{int}$ corresponds to the interfacial energy between the self-assembled domains in the particle, and $\mathbf{F}_{str}$ originates from the stretching of the lamellae. Figure 34 c shows the (normalized) free energy $\mathbf{F}$ of a microparticle is a function of its aspect ratio α for emulsion droplets with an initial diameter $D = 2\,\mu m$. The free energy is minimized for nearly spherical particles ($\alpha \approx 1$), suggesting that the prolate microparticles found in the experiments and simulations were indeed trapped in long-lived non-equilibrium states. According to our theoretical model, prolate ellipsoids become the true equilibrium shape only when the interfacial tension between the polymers and aqueous medium was reduced by a factor of 50 to $\gamma_{PW} \approx 0.3\,mN\,m^{-1}$, which is much lower than typical interfacial tensions reported for SDS-stabilized oil droplets in water [202]. As an additional test, we also performed the theoretical calculations using the parameters from our simulation model, for which all required values are known exactly (see Methods section). However, even in this case, the theory predicted spherical microparticles, whereas we consistently found prolate ellipsoids in the simulations (see, e.g., inset of Figure 34 c). We were only able to create spherical microparticles (with disordered lamellae) in our simulations

when we changed solvent instantaneously (see Methods). Thus, the preparation protocol plays an important role in the size and shape of the resulting microparticles.

Table 4: Specifics of SBM/hPB microparticles.

Code[a]	hPB	ϕ_S [b]	ϕ_B [b]	ϕ_M [b]	L_0^c
SBM-0	0	40	22	38	27.9
SBM-10	10	39	24	37	28.0
SBM-25	25	38	26	36	28.5
SBM-50	50	36	30	34	29.9
SBM-75	75	34	33	33	30.9
SBM-100	100	33	36	31	31.5
SBM-200	200	28	46	26	32.8
SBM-300	300	24	53	23	

[a] SBM-x with x = added hPB in wt %. [b] Overall composition within the microparticles in wt %. [c] Thickness of the PB microdomain according to gray-scale analysis.

Microparticle Morphologies of SBM/hPB Blends: Table 4 gives specifics for SBM/hPB microparticles prepared with a pore diameter of $D_{pore} = 0.6\,\mu m$ and the added weight fractions of hPB ranging from $x = 0, 10, 25, 50, 75, 100, 200$, and 300 wt% with respect to PB in the SBM terpolymer. Exemplified on 100% hPB (SBM-100), to 10 mg of SBM-0 that contains 2.2 mg of PB (22 wt %), another 2.2 mg of hPB was added before emulsification. We chose a small molecular weight of $M_n = 2000\,g\,mol^{-1}$ for hPB so that the hPB chains enrich in the PB microdomain of the SBM morphology after solvent evaporation [186]. Since the hydrophobic hPB cannot escape the shrinking oil droplets, the overall composition of the microphases (ϕ_{SBM}) within the microparticle changes with the amount of added hPB, *e.g.*, for 100% hPB the composition becomes $\phi_{PS} = 33$ wt%, $\phi_{PB} = 36$ wt%, and $\phi_{PMMA} = 31$ wt%.

Figure 35 summarizes the morphological evolution of the SBM/hPB morphology in the microparticles, in simulations, as well as after crosslinking of the PB/hPB microdomain and redispersion in THF. Changes to the inner morphology with increasing hPB content were measured by grayscale analysis using ImageJ (Table 4). Although morphological changes can be followed in close-up TEM images to some extent, they were rather subtle from $0\% - 50\%$ hPB, and became more noticeable for $75\% - 200\%$ hPB. Our DPD simulations are not affected by such analytic challenges,

making them a valuable tool for analyzing the internal microparticle morphology. All microparticles retained their prolate ellipsoidal shape after hPB blending and predominantly reside on the TEM grid with their major axis parallel to the surface (Figure 35 a-f). The SPG method produced microparticles with narrow size distribution and the DLS measurements give an average hydrodynamic radii in the range of $R_h = 180 - 300\,\text{nm}$. On the first view, the hPB migrated into the PB microdomains and did not microphase separate from the triblock terpolymer to form homopolymer domains as would be the case for high M_n additives [186, 203].

At 0% hPB ($\phi_{PB} = 22\,\text{wt\%}$), microparticles exhibit single dark spots of PB sandwiched between the PS/PMMA lamellae attributed to PB cylinders (Figure 35 a). This assumption is supported by the lamellar-cylinder bulk morphology and the ring morphology obtained from simulation results that agree well with previous works [190]. After crosslinking, the resulting nanodiscs contained a cylinder morphology, yet, arranged as parallel stripes instead of concentric rings. We already observed a range of transition structures at $\phi_{PB} = 22\,\text{wt\%}$ in previous works, which we attributed to the polydisperse microparticle populations obtained from the uncontrolled emulsion process. With the SPG method, we here obtained more homogeneous microparticles, and the fraction of striped nanodiscs increased. The difference between experiment and simulation might be assigned to a volume increase of the PB microdomain in experiments due to an undetermined amount of OsO_4 that is introduced during crosslinking [190]. Nevertheless, both simulation and experiment confirm PB cylinders, albeit with different orientations. At 10% hPB ($\phi_{PB} = 24\,\text{wt\%}$) and 25% hPB ($\phi_{PB} = 26\,\text{wt\%}$), the microparticles developed diagonal stripes suggesting changes to the PB morphology (Figure 35 b, c). This transition is confirmed by our simulation results, where we first observed the formation of small bridges between the concentric rings, followed by a transition of the PB layers to perforated lamellae [204], where the pore size decreases with increasing ϕ_{PB}. The crosslinked nanodiscs closely followed the morphologies predicted by our microparticle simulations, *i.e.*, the cylinders have merged into a perforated morphology with an average hole diameter of 40 nm that decreased to 25 nm. At 50% hPB ($\phi_{PB} = 29\,\text{wt\%}$), PB microdomains appear lamellar, and after crosslinking only few pores remained with a ring of perforations at the

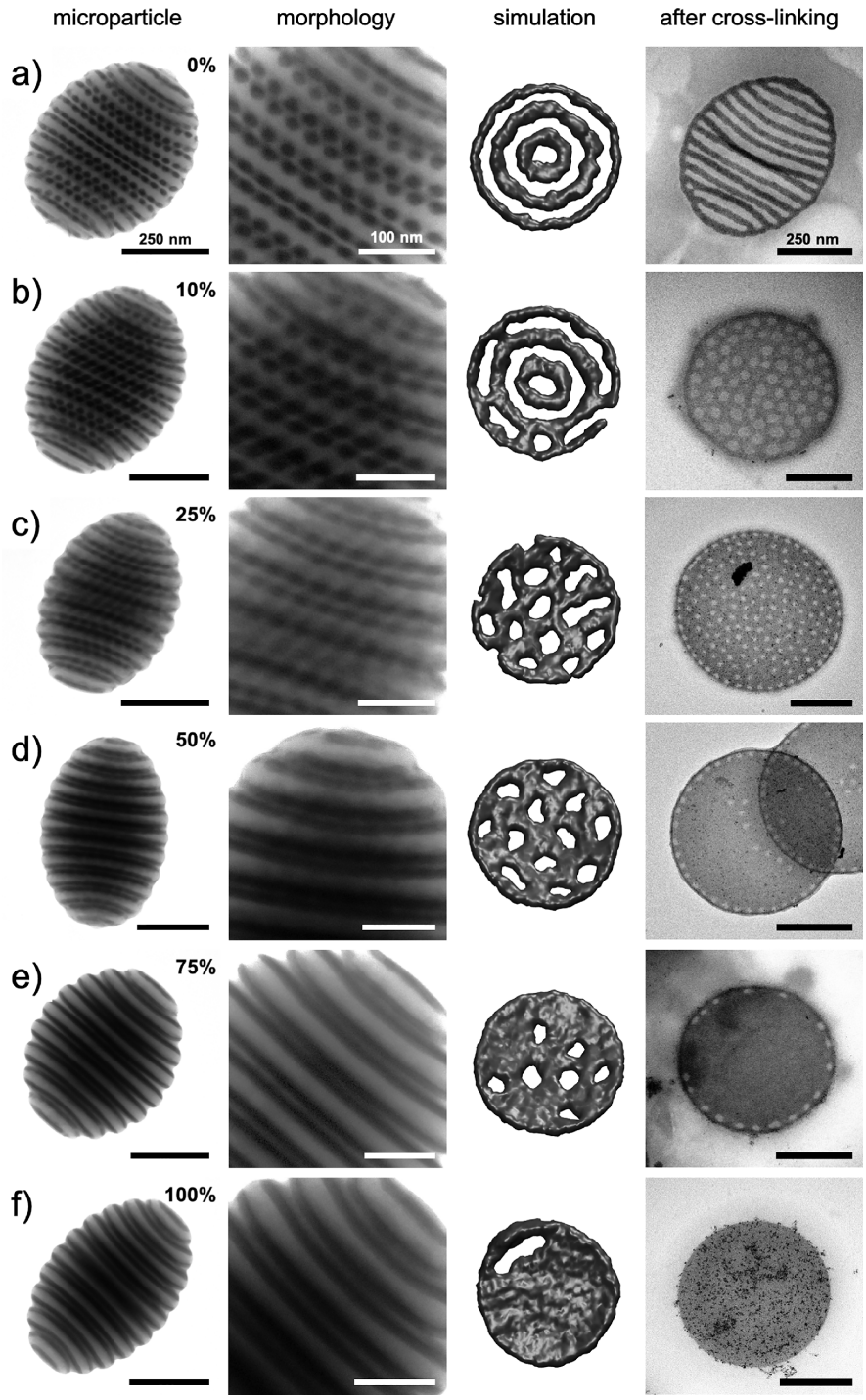

Figure 35: Morphological evolution of the PB microphase with increasing addition of hPB followed by TEM and simulations. (**a**) Without hPB, (**b**) 10% hPB, (**c**) 25% hPB, (**d**) 50% hPB, (**e**) 75% hPB, and (**f**) 100% hPB. Scale bars in (**b-f**) are as indicated in (**a**).

nanodiscs edge (Figure 35 d). The increase in L_0 from 28.5 nm to 29.9 nm supported the morphological transition to a more continuous PB lamella, because fewer pores provide space for the adjacent PS and PMMA chains that instead entropically stretch at the lamella-lamella interface. At 75% hPB ($\phi_{PB} = 33$ wt%), microparticles showed

a transition to lamella-lamella morphology. The interior of the crosslinked nanodiscs was filled completely and merely a few perforations remained at the nanodisc edge, as also confirmed by our DPD simulations (Figure 35 e). Homogeneous filling of the PB microdomain to complete lamella was achieved at 100% hPB ($\phi_{PB} = 36\,wt\%$) (Figure 35 f), which persisted at 200% hPB ($\phi_{PB} = 46\,wt\%$) with increased L_0 from 31.5 nm to 32.8 nm. The observed morphological developments upon addition of hPB are similar to our previous findings for the bulk morphologies of the same SBM/hPB blends up to 200% (Figure 26) hPB [192] .

There are, however, limitations to the amount of hPB that can be blended into the PB lamella. At 300% hPB ($\phi_{PB} = 53\,wt\%$), a complete morphological transition occurred for the confined systems. The microparticle shape changed to spheres where PB apparently formed a three-dimensional bicontinuous microphase, likely because the previously separated PB lamellae connected through the PS/PMMA microphases that now form the minority fraction with about 25 wt% each. This morphology is interesting as PS and PMMA are separated by the PB microphase, opening possibilities to create mesoporous microparticles with two chemically different interpenetrating networks.

The shape, internal morphology, and Janus character of the nanodisc were further analyzed by AFM measurements (Figure 36). Janus nanodiscs derived from SBM-0 exhibited a height of approximately 38 nm, while the height increased to 46 nm for 25% hPB, and to 48 nm for 100% hPB (Figure 36 a). The height increase is expected as hPB chains progressively fill the space between the PB microdomains and thereby prevent the PS and PMMA chains from collapsing into this space. Additional contributions to the height stem from the PS and PMMA chains that are swollen by the casting solvent (THF) and randomly collapse on top and below the nanodiscs. The lower order of collapsed chains (*e.g.*, compared to slow drying in the microparticles) contributes to the measured height and explains the difference to the measured L_0 in the microparticles. In addition, we were also able to visualize the inner structure of the nanodiscs via AFM topography. The PB beams at 0% appear to be flexible and bent out of plain independent of each other, reminiscent of nanodiscs cut into stripes. The solvent swelled PMMA/PS chains induce considerable stress on the PB frame-

work leading to the fracturing of the structure on several occasions. Similarly, it was possible to visualize the holes of the perforated nanodiscs, which confirmed that the nanodiscs are indeed porous on the inside.

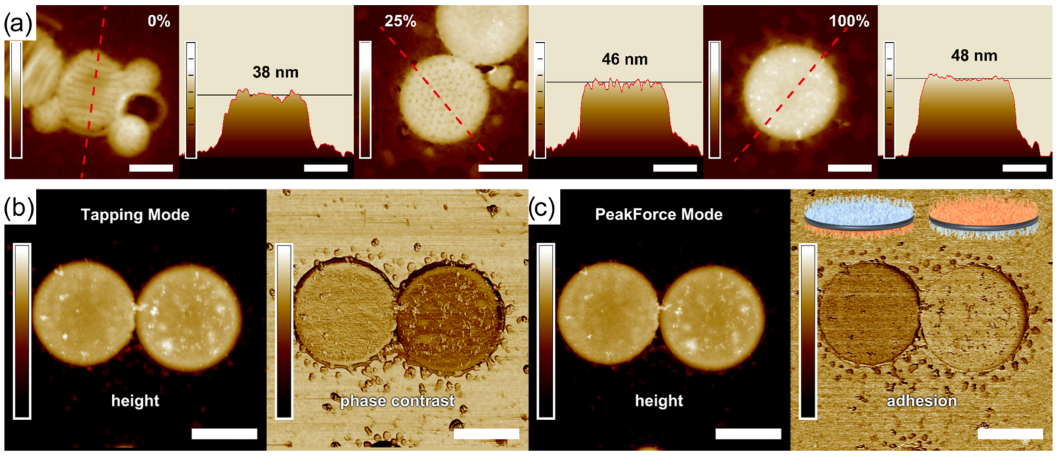

Figure 36: AFM analysis of Janus nanodiscs. (**a**) AFM topography images (left) and corresponding height profiles (right) of Janus nanodiscs from SBM/hPB blends as indicated. Two Janus nanodiscs of SBM-100 (ϕPB = 36%) measured with (**b**) tapping mode to give height and phase contrast images and (**c**) peak force mode to measure height and adhesion, respectively (the schematics in (**c**) are an interpretation of the disc orientation); the color bar indicates the data range between the minimum (dark) and maximum (bright) of phase shift and adhesion. The total z range of each height color bar is 70 nm. Lateral scale bars are 250 nm.

Although all nanodiscs should consist of a PB core decorated with PS chains on one side and PMMA chains on the other, it is not possible to distinguish both sides in TEM projection imaging. In AFM however, we were able to show the Janus character of the nanodiscs, as exemplified on filled nanodiscs prepared from SBM-100 (Figure 36 b, c). We identified differences in the phase shift (phase contrast, Figure 36 b) of the two sides in tapping mode, as well as in the adhesion between the tip and sample surface for PeakForce measurements (adhesion contrast, Figure 36 c). Although both disc surfaces, PMMA and PS, cannot be directly assigned to one of the displayed discs, the measurements clearly show a difference between both sides and confirm the Janus character.

Hybrid SBM/Pt Janus Nanodiscs: Combining the amphiphilicity of the nanodisc surface with the complex structure of the core could lead to promising templates for interfacial catalysis. To investigate the possibility of selectively incorporating catalytic metal nanoparticles into the Janus nanodiscs, we loaded Pt into the PB core. We

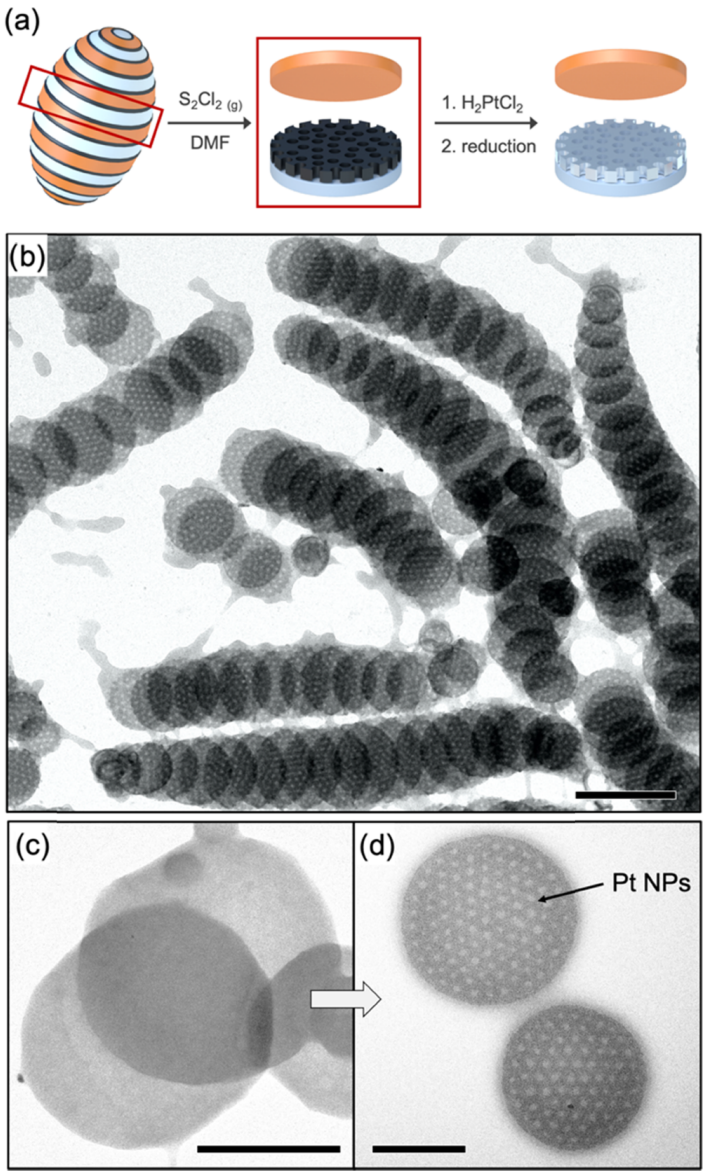

Figure 37: Pt NPs loading of perforated Janus nanodiscs. (**a**) Schematic process of S_2Cl_2 crosslinking followed by separation and Pt loading. (**b**) TEM overview image of S_2Cl_2 crosslinked nanodiscs (stained with OsO_4; scale bar is 500 nm). **c**) TEM image without staining and before Pt loading and (**d**) after loading (scale bars are 250 nm).

chose the perforated topology at 10% hPB loading as the most promising candidate due to their mechanical stability (compared to the striped pattern at 0% hPB) as well as their larger interfacial area compared to filled nanodiscs. Prior to the Pt loading, the microparticle dispersion was dried and exposed to S_2Cl_2 vapor, which is another selective crosslinking method for the PB domains. Sulfur crosslinking led to perforated sheets as seen in Figure 37 b (the contrast was enhanced by OsO_4 vapor only for TEM imaging). The sulfur bridges are able to coordinate the H_2PtCl_2 precursor

that in a subsequent step was reduced to Pt NPs with ethylene glycol under elevated temperatures (Figure 37 a) [205]. The successful formation of Pt NPs was then verified by comparing TEM images of the perforated Janus nano-discs before (Figure 37 c) and after nanoparticle formation (Figure 37 d). While sulfur crosslinking (without staining) does not provide any contrast for TEM imaging, the embedded Pt NPs exhibit strong own contrast due to the heavier atoms present. This contrast gives a qualitative measure of how well the Pt NPs were distributed in the perforated PB core. After loading, the inner PB core can be seen very clearly, suggesting that the Pt NPs formed evenly throughout the PB core. This finding demonstrates that it is possible to introduce active materials selectively into the core domain of the Janus nanodiscs.

6.4 CONCLUSIONS

In summary, the combination of simulations, theory, and experiments provided detailed insights into the microphase separation behavior in double confinement, *i.e.*, in three-dimensional microparticles with two-dimensional, confined polymer lamellae. After crosslinking the PB microdomains, redispersion of the microparticles led to Janus nanodiscs with a complex inner structure depending on the blended PB homopolymer fraction. Janus nanodiscs exhibit uniform thickness from microphase separation and narrow size dispersity due to the microparticle diameter controlled by the SPG membrane. Preliminary work on PB core loading with Pt nanoparticles confirmed the formation of perforated Pt/SBM nanodisc hybrids, which we currently pursue as nanoreactors in interfacial catalysis and hydrogenation reactions [206]. These hybrids combine the interfacial activity from the Janus character with the high surface area of the catalytic species in the perforated core, which alleviates the purification of products by straightforward catalyst removal through centrifugation or filtration. More generally, the presented method is scalable to polymer concentrations of $50\,\mathrm{g\,L^{-1}}$, thus allowing for the large-scale fabrication of polymer Janus nanodiscs in quantitative yields. Given the large variety of existing ABC triblock terpolymers, we

expect the straightforward tuning of microdomains to be adapted to other chemistries towards the synthesis of larger libraries of functional Janus nanoparticles.

7

SELF-ASSEMBLY OF AMPHIPHILIC POLYMERS INTO PATCHY POLYMEROSOMES

7.1 INTRODUCTION

Polymerosomes are spherical vesicles formed by the self-assembly of amphiphilic block copolymers in an aqueous solution and have a bilayer architecture. Their architecture is similar to liposomes which are vesicles of naturally occurring phospholipids. Polymerosomes are more stable both mechanically and chemically as compared to liposomes [207, 208] because of the higher molecular weight of polymers, and they have applications drug delivery [209], nanoreactors [210, 211], artificial organelles [212] and cell tracking. The polymers used for fabricating polymerosomes are usually diblock copolymers or symmetric triblock copolymers, which form unilamellar vesicles with a homogeneous surface. Triblock terpolymers which consist of two different hydrophilic blocks, make the self-assembly of vesicles with an inhomogeneous surface or asymmetric membranes possible. In many applications, surface exposure plays an important role, especially in drug delivery applications where we can target the affected cell appropriately, making the study of such patchy polymerosomes significant. Several studies have already been conducted on obtaining polymeric vesicles, but very little is known about the patchy polymerosomes. To explore the idea of patchiness on the surface of the Polymerosome, we investigated the effect of different positioning of the blocks in a triblock terpolymer chain as well as the different configurations of the triblock terpolymer using coarse-grained DPD simulations. Also, we have showcased the effect of hydrophilic block length on the formed surface patches of the polymerosomes along with the cavity size.

7.2 MODEL AND SIMULATION DETAILS

We used the DPD simulation technique [99, 105, 213] in combination with a coarse-grained bead-spring model. In DPD, the net force on a particle i is given by the sum over conservative forces, $\mathbf{F}_C$, dissipative forces, $\mathbf{F}_D$, and random forces, $\mathbf{F}_R$, given in Equation 75.

In our simulations, the DPD particles are modeled as spherical beads with diameter a and unit mass m, irrespective of the specific particle type. For the conservative forces between bonded and non-bonded DPD particles, we employed the standard soft repulsion (Equation 94).

The parameter A_{ij} controls the (maximum) repulsion between particles i and j and the specific values of A_{ij} depend on the simulated system and the chosen parameterization, and the mapping to experiments is discussed further below. Bonded interactions within a polymer are modeled using harmonic springs (see Equation 95).

The value of the spring constant is $k = 4k_BT/a^2$ in the reduced simulation units, same as we used in previous work (Section 6.2.2).

The DPD particles are also subject to pairwise dissipative (Equation 96 and 98) and random forces (Equation 97 and 98), which impart thermal fluctuation and drag, and also serves as thermostat on the DPD particles.

To satisfy the fluctuation-dissipation theorem, the random independent variable ξ has zero mean, $\xi(t) = 0$, and a variance $\langle \xi(t)\xi(t') \rangle = 2k_BT\delta(t - t')$ [99]. In this work we used the same drag coefficient $\gamma_{ij} = \gamma = 4.5\sqrt{mk_BT}/a$ for all particles.

All simulations have been conducted in a cubic box of dimensions $L_x = L_y = L_z = 80\,a$, with periodic boundary conditions applied to all three Cartesian directions. A particle number density of $\rho = 3\,a^{-3}$ was used, and the temperature was set to $T = 1$ for all simulations. Starting configurations were generated by randomly placing all polymers and solvent beads in the simulation box. Initially, we set the cross-interaction to $A_{ij} = A_{ii}$ so that the polymers are well dispersed in the solvent. Afterward, the A_{ij} were gradually increased to their final values for 4×10^6 time steps ($\Delta t = 0.05$). Typically, the simulations were run for 7×10^6 time steps in total, and we verified that the systems reached equilibrium by tracking the system's poten-

tial energy. All simulations have been conducted using the HOOMD-blue simulation package (v.2.2.1) [135, 214].

7.2.1 *Model Parameterization*

In order to choose the DPD repulsive parameters A_{ij}, it is instructive to consider an experimental system as a reference. In this work, we have considered amphiphilic polymers composed of hydrophobic Poly(ethylethylene) (PEE), hydrophilic Poly(2-propenamide) (PAM), and hydrophilic Poly(ethyleneoxide) (PEO). These polymers are interesting for the fabrication of patchy micelles and polymerosomes in water (W) because they are partially immiscible to each other and the aqueous solvent and they are commercially available in large quantities. Further, the hydroxylic end-groups of diblock PEE-*b*-PEO (EO) copolymers can be used to attach ligands or antibodies, which is an interesting feature for applications in drug delivery [215].

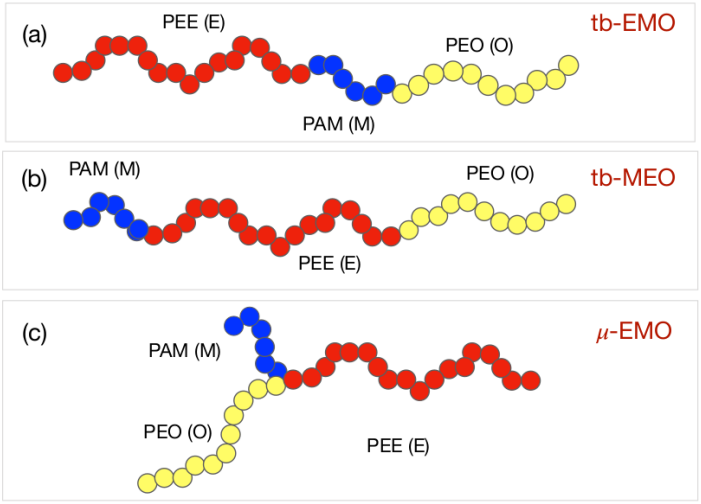

Figure 38: Different configurations of asymmetric triblock copolymer, (**a**) tb-EMO, (**b**) tb-MEO, and (**c**) 3-arm miktoarm (μ)-EMO, with E beads represented in red color, M in dark blue and O in yellow. The same color codes have been used for respective blocks in all Figures.

In this work we considered two diblock copolymers, *i.e.*, EO and PEE-*b*-PAM (EM), and three triblock copolymers consisting of PEE, PEO, and PAM. The three blocks can be arranged in various ways to obtain different triblock configurations. Here, we considered linear PEE-*b*-PAM-*b*-PEO (tb-EMO), linear PAM-*b*-PEE-*b*-PEO (tb-MEO),

and a star shaped PEE-*b*-PAM-*b*-PEO also know as miktoarm (μ-EMO), as shown in Figure 38.

In the employed model, the only distinguishing feature between the different monomer types is the mutual interaction strength A_{ij}, while all the other properties, *e.g.*, bead diameter, bond length, and bending stiffness are identical. On the one hand, such a simplified polymer description neglects atomistic details, such as chain tacticity and hydrogen bonding. On the other hand, the generic nature of the employed model allows for reaching longer simulation length- and time-scales. Further, it facilitates the extension of our simulation results to other systems that have similar solution properties.

Groot and Warren derived relations between the interaction strength A_{ij} and the Flory-Huggins χ parameter [105]. For the employed particle number density of $\rho = 3\,a^{-3}$ it is

$$A_{ij} = A_{ii} + 3.497\chi\,, \tag{101}$$

where $A_{ii} = 25\,k_BT$ is the interaction strength between particles of the same type.

For the PEO-water interactions, Groot and Rabone reported a value of $\chi(O-W) \approx 0.3$ [100, 216], by extrapolating experimental data by Saeki *et al.* from high-temperature demixing data to room temperature [217]. For the PAM-water interaction, a value of $\chi(M-W) \approx 0.49$ was reported in the literature [218]. We were unable to find reference data for $\chi(O-E)$, $\chi(O-M)$, and $\chi(E-M)$, and therefore resorted to the Hildebrand-Scott relation to estimate the interaction parameters

$$\chi_{ij} = \sqrt{(V_iV_j)}\frac{(\delta_i-\delta_j)^2}{RT}\,. \tag{102}$$

Here, V_i and V_j are the molar volumes of molecules i and j, with Hildebrand solubility parameters δ_i and δ_j, respectively, and R is the ideal gas constant. The employed values for V_i and δ_i are summarized in Table 5 and the resulting Flory-Huggins interaction parameters are presented in Table 6.

Table 5: Molecular mass M, molecular volume V, mass density ρ_M and solubility parameter δ [218].

	M	$V(Å^3)$	$\rho_M(g/cm^3)$	$\delta(cal^{1/2}cm^{-3/2})$
W	18.1	30.02	1.001	23.47
O	44	64.75	1.13	9.97
E	56.11	108.25	0.859	8.21
M	71.08	90.65	1.3	11.98

Table 6: Flory Huggins χ and interaction parameters A_{ij} between all particle pairs.

Interaction pairs	χ	χ_{eff}	A_{ij}
E-W		15.02 [219]	77.5
M-W	0.49	4.18	39.6
O-W	0.3	3.05	35.7
E-M	1.43	8.29	54.0
O-M	0.31	2.61	34.1
O-E	0.26	1.83	31.4

In our simulations, the diblock copolymers consist of $N_E = 18$ E and $N_M = 6$ M beads, respectively ($N = N_E + N_M = 24$), while the EO diblock copolymers have $N_E = 18$ E and $N_O = 11$ O beads, respectively ($N = N_E + N_O = 29$). The triblock copolymers consist of $N_E = 18$ E, $N_M = 6$ M and $N_O = 11$ O beads, so that $N = 35$. These values corresponds to an experimental system of $13\,kg\,mol^{-1}$. The volume fraction of the hydrophobic block in the diblock copolymers EO and EM are $f_E = N_E/N = 0.62$ and 0.75, respectively, while it is fixed for triblock copolymers, *i.e.*, $f_E = 0.51$. Note that in our model, the volume, number, and mass fraction are interchangeable quantities, since all beads have equal volume and mass. In our model, all types of coarse-grained beads have the same volume of $600\,Å^3$ ($a = 1.05\,nm$). As a consequence, each bead type contains a different number of monomers, so that one needs to rescale the χ parameter to preserve the experimental χN. These adjusted values, χ_{eff} are also listed in Table 6. We were unavailable to find $\chi(E-W)$ in literature, and have taken the χ_{eff} for PEE and water from the work of Zhao *et al.* [219].

7.3 RESULTS AND DISCUSSION

The snapshots in Figure 39 for two diblock copolymers EM and EO show that both the copolymers self-assemble into unilamellar polymeric vesicles in an aqueous solution. We estimated the vesicle size and cavity size, *i.e.*, the outer radius (r_o) and the inner radius (r_i), respectively. We evaluated the thickness of the membrane wall as $d = r_o - r_i \approx 2\,R_g$, where R_g is the radius of gyration of the wall-forming hydrophobic E block, which can be calculated as, $2\,R_g \approx 2\,a(N_E/6)^{1/2}$. The volume of the hydrophobic shell is, $V_{shell} = 4\pi({r_o}^3 - {r_i}^3)/3$, and in simulation it corresponds to the total number of hydrophobic beads, $V_{shell} = N_E N_P/\rho$. Substituting all corresponding values and solving the equations, we obtain the inner and outer radius as $\approx 28\,a$ and $\approx 32\,a$. It is important to note that in this approximation, the vesicle size is independent of the size of the hydrophilic blocks.

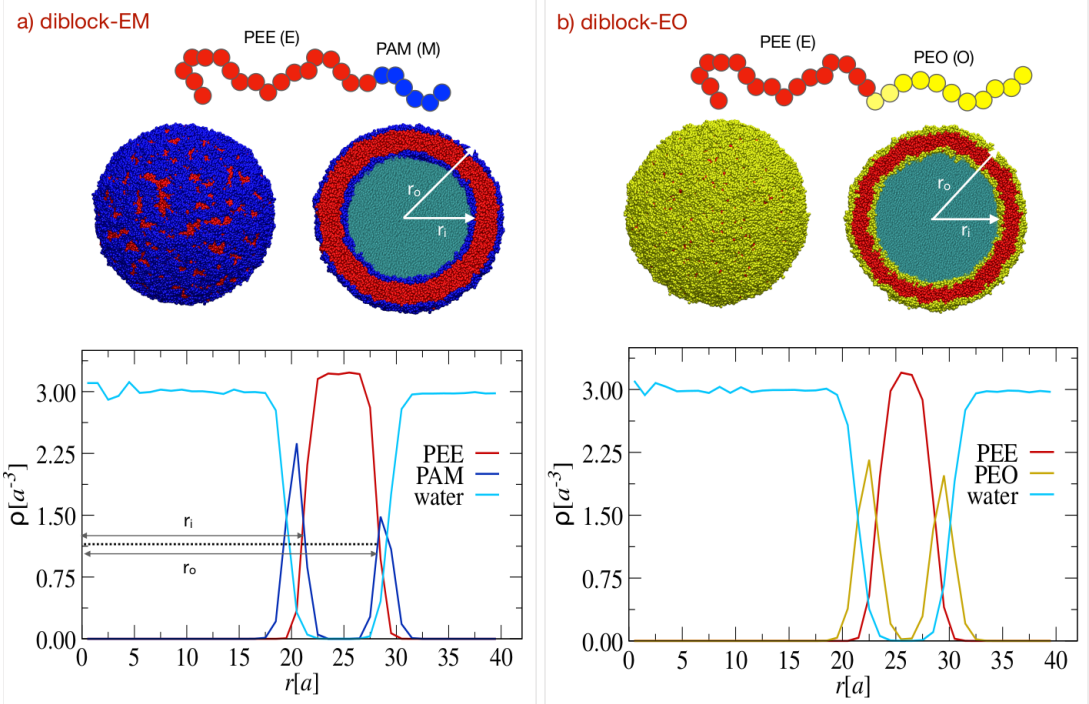

Figure 39: Simulation snapshots and their radial density distribution as a function of distance from the vesicle center of mass (COM) for (**a**) diblock EM, and (**b**) diblock EO.

Furthermore, to analyze the structure of the polymeric vesicle, the radial density distribution profile [220] from the vesicle center of mass (COM) is plotted in Figure 39. The two peaks of the hydrophilic M and O blocks signify the two water interfaces,

and the flat bottom valley of the water beads specifies the area occupied by the hydrophobic E beads. We also obtained the cavity size and vesicle size from the radial distribution plot by determining the radial distance where the number density of water beads became $1.5\,a^{-3}$ (Figure 39).

For diblock copolymer EM (Figure 39 a), the $r_i \approx 19.5\,a$ and $r_o \approx 29.4\,a$, and the wall thickness, $d = r_o - r_i \approx 9.9\,a$. The theoretically estimated values are larger than the values obtained from the density plot because we considered the thickness of the hydrophobic block in terms of R_g. From the radius, we calculated the inner and outer surface area to estimate the number of hydrophilic beads required to fill up the entire surface of the vesicle. The inner surface area is calculated as $A_i = 4\pi {r_i}^2 \approx 4783\,a^2$ and the outer surface area is $A_o = 4\pi {r_o}^2 \approx 10832\,a^2$. Hence, the total number of M beads required to fill up both the inner and outer surface of the vesicle is 46847, considering the density to be $3a^{-3}$. The total number of M beads present in the system is 39498, meaning fewer hydrophilic beads, which are not enough to cover up the vesicle's entire surface and explains the patchy surface of the diblock EM.

Similarly, the obtained values for the inner and outer radius of diblock EO are $r_i \approx 21\,a$ and $r_o \approx 30\,a$, respectively, and the wall thickness is $d = 9\,a$. The corresponding surface areas are $A_i \approx 5728\,a^2$ and $A_o \approx 11529\,a^2$. Here, the number of hydrophilic beads required to fill up both the inner and outer surface is 51772, which is much smaller than the $\approx$ 72413 O beads present in the system. Thus, there are sufficient O beads to cover both the surfaces (Figure 39 b).

The formation of thermodynamically stable block copolymer morphology is predominantly governed by three contributions to the system's free energy: (*1*). The degree of stretching of the hydrophobic block, (*2*). The interfacial tension between the vesicle forming the core and the solvent outside the core, and (*3*). The interactions among the corona forming hydrophilic chains. Since the hydrophobic block length is the same for the diblock EO and EM, the size of the vesicle is controlled by the balance of the two other contributions, *i.e.*, the interfacial tension between the core and water, and the repulsion between the chains forming corona. The longer chain size results in increased repulsion between the chains, and we observe the formation of a bigger vesicle. This also contributes to a bigger cavity size and thinner wall

membrane for EO than EM. Also, the interaction of an individual block with water ($\chi - parameter$) has a considerable effect on the size of the formed particle. Due to the higher hydrophilicity of O than M, O increases the contact area with water, and hence EO formed a bigger vesicle.

We reported two diblock copolymers EO and EM, for the same polymer concentration in water, they self-assembled into a bilayer vesicle with a homogeneous surface. We also simulated diblock EM and EO for different hydrophilic block lengths *i.e.*, $E_{18}M_6$, $E_{18}M_{11}$, $E_{18}M_{17}$, and $E_{18}O_6$, $E_{18}O_{11}$, $E_{18}O_{17}$. Comparing the two diblock systems for the same length of the hydrophilic block shows that the diblock EO forms a bi-layered vesicle for $N_O = 11$ and 17, while EM does it for $N_M = 6$ and 11.

Amphiphilic diblock copolymers self-assembled into polymer vesicles depending on the hydrophilic block length/volume fraction. However, vesicle formation in triblock copolymers induces the formation of morphologies that are inaccessible by diblock copolymers or symmetric triblock copolymers. Considering that the morphologies of self-assembled nanostructures are mainly governed by the length of the respective blocks and the volume fraction of the polymer in the solution, we investigated the asymmetric triblock terpolymer system.

From Figure 40 a and Figure 40 b, we can see that the aggregate formed for tb-EMO is a patchy polymerosome with small uniformly distributed islands of PAM at the two water interfaces. The radial density distribution profile (Figure 41 a) shows two distinct peaks of M and O blocks, which implies they are present both at the outer surface and inner surface of the vesicle. The hydrophobic E block occupies the region in between the two peaks of hydrophilic blocks. The U-shaped curve of water beads confirms the presence of water inside the cavity. We obtained the vesicle radius and the cavity radius in the same way we did for the diblock copolymers from the density plot. The values are $r_i \approx 12\,a$, $r_o \approx 27\,a$, and $d \approx 15a$. The polymerosome formed from triblock copolymer tb-EMO is smaller than the diblock copolymer EO and EM due to a smaller concentration of hydrophobic E block, which defines the size of the polymerosomes.

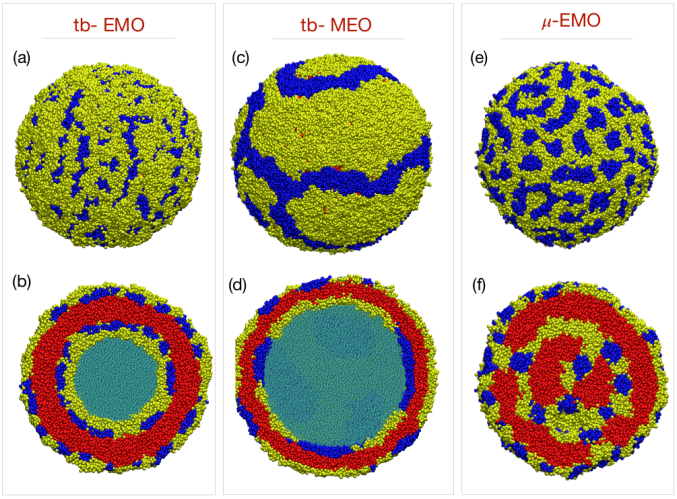

Figure 40: Simulation snapshots showing full particle view in a,c, and e, and cross-sectional view in b, d, and f, for triblocks tb-EMO, tb-MEO and μ-EMO respectively.

Figure 40 c and d shows the snapshots of the full view and the cross-sectional view for triblock tb-MEO. Again, the triblock copolymers self-assembled into vesicles with a bi-continuous patch of the hydrophilic blocks, M and O. Polymerosomes formed by triblock copolymers with two different hydrophilic blocks at both ends can potentially have different orientations. We can have one hydrophilic block inside and the other outside and vice versa. In the third case, we can have a mixture of both the hydrophilic blocks at both the water interfaces. Wolfgang *et al.* [221] report that if one of the two hydrophilic blocks is distinctively shorter than the other, one will obtain a stable vesicle with the shorter ones at the interior surface and the longer ones on the exterior surface [221], in contrast to what we have observed in our simulations. A plausible explanation for the presence of a mixture of hydrophilic blocks on the water interfaces is that the hydrophilic blocks PAM and PEO like each other more than they like water.

We calculated the inner and outer radius from the radial density plot (Figure 41 b), and the values are $r_i \approx 22\,a$ and $r_o \approx 31\,a$ respectively, which corresponds to a wall thickness of $\approx 9\,a$. Comparing the two linear triblock tb-EMO and tb-MEO, it is very well noticeable that tb-MEO has a bigger cavity and a thinner wall, concluding a bigger vesicle. Also, the patchy polymerosome formed for tb-MEO is bigger than the diblocks EO and EM due to the arrangement of the hydrophilic blocks, which reduces the repulsion between the corona forming hydrophilic block.

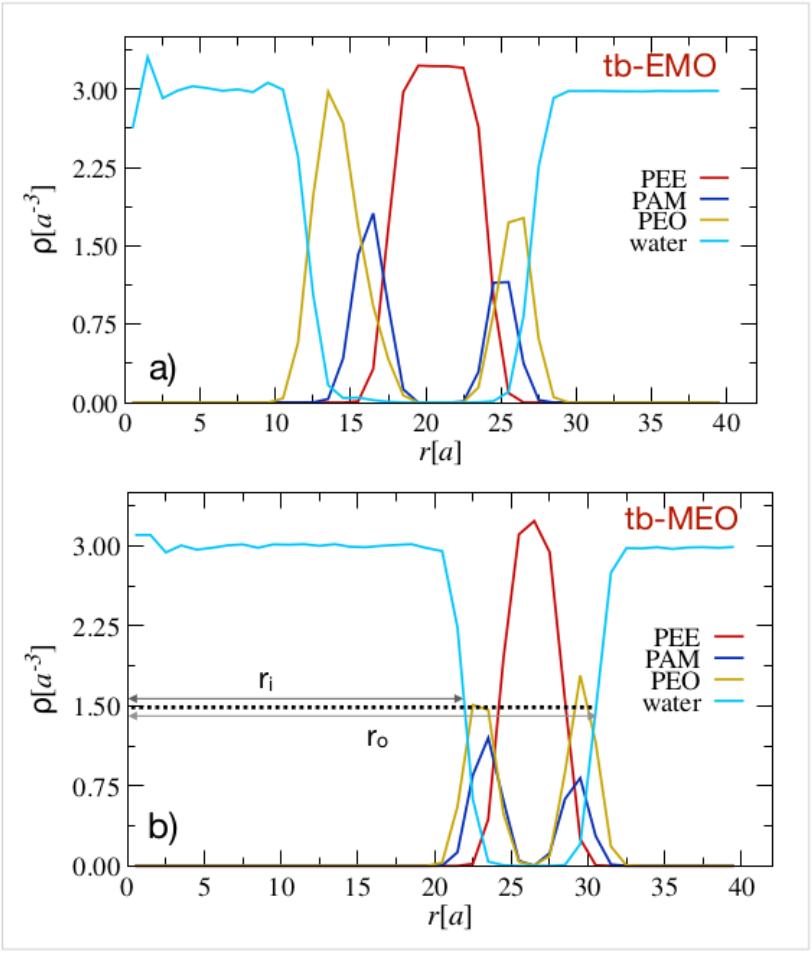

Figure 41: Radial density distribution of a) triblock EMO, and b) triblock MEO, as a function of distance from vesicle COM.

The stages of vesicle formation for tb-MEO are shown in Figure 42, where the simulation starts with a homogeneous mixture at time steps, $t = 0$. With time, the aggregates of polydispersed micelles begin to form. At an intermediate time steps, the micelles fuse together, forming rods which subsequently bends (Figure 42 a at $t = 7 \times 10^5$) and enclosure of such bent rods marks the formation of the final aggregate called vesicle (Figure 42 f at $t = 3.2 \times 10^6$ steps).

To examine the effect of polymer architecture on the self-assembled morphology, we also simulated a star-shaped triblock copolymer (μ-EMO). Figure 40 e, f shows that the nanostructure obtained is not vesicles anymore. Instead, the cross-sectional view reveals an onion-like micelle with two layers of hydrophobic E block.

Apart from the polymer architecture, we also investigated the effects of different hydrophilic block lengths on tb-MEO, keeping the hydrophobic length the same *i.e.*,

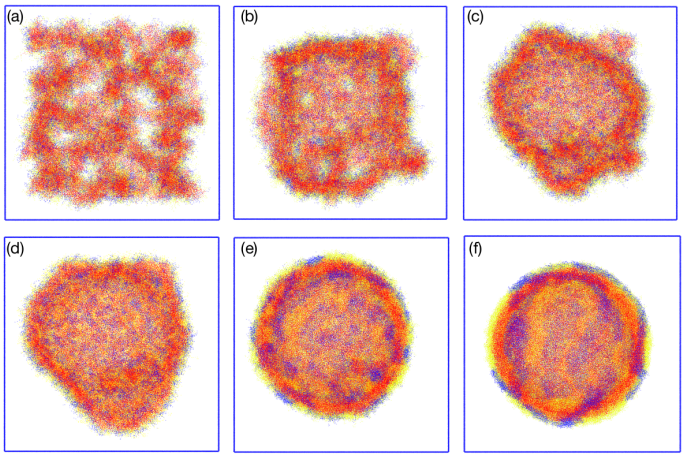

Figure 42: Simulation snapshots of time evolution at different time steps (t) of tb-MEO in aqueous solution, (**a**) 7×10^5, (**b**) 9.5×10^5, (**c**) 1.05×10^6, (**d**)1.2×10^6, (**e**)2×10^6, (**f**)3.2×10^6

.

$N_E = 18$. We considered six different combinations by varying the length of hydrophilic blocks, M and O. For a fixed chain length; we varied the length of both the hydrophilic blocks to keep the total length of the hydrophilic block the same for all the systems. Here, for simplicity, we show the results for the M block only. The lengths of the M block (N_M) are $0, 2, 6, 9, 15, 17$ and the corresponding O blocks (N_O) are $17, 15, 11, 8, 2, 0$. The resulting volume fractions of the hydrophilic M block are $f_M = 0.00, 0.06, 0.17, 0.26, 0.43, 0.49$.

It is apparent from the snapshots (Figure 43) that in the absence of M block, the diblock copolymer $E_{18}O_{17}$ self-assembled into a bi-layered vesicle with a homogeneous surface as seen before also for the diblock $E_{18}O_{11}$. As soon as we have a triblock with a small fraction of M, the island-like patches start to appear on both the water interfaces. With further increase in M, the distant patches become continuous and appear as bi-continuous patches. Finally, more increase in f_M leads to a transformation of the patchy surface from bi-continuous to more Janus-like with two distant patches of each block. The cross-sectional view suggests that the increase in the fraction of M block hinders the stability of the polymeric vesicle, as the cavity size has a noticeable change. In addition, we plotted the density distribution profile of water beads (Figure

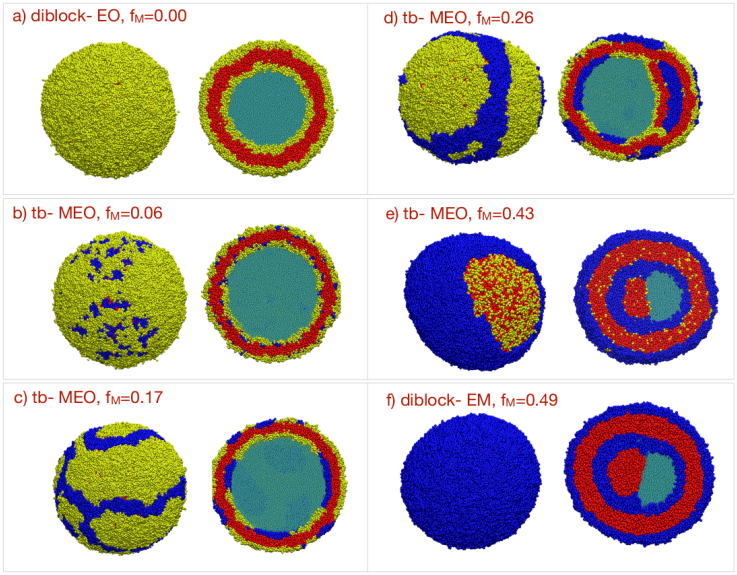

Figure 43: Simulation snapshots showing full and cross-sectional view for tb-MEO at different hydrophilic fractions, (**a**) 0.0-M, (**b**) 0.06-M, (**c**) 0.17-M, (**d**) 0.26-M, (**e**) 0.43-M, and (**f**) 0.49-M.

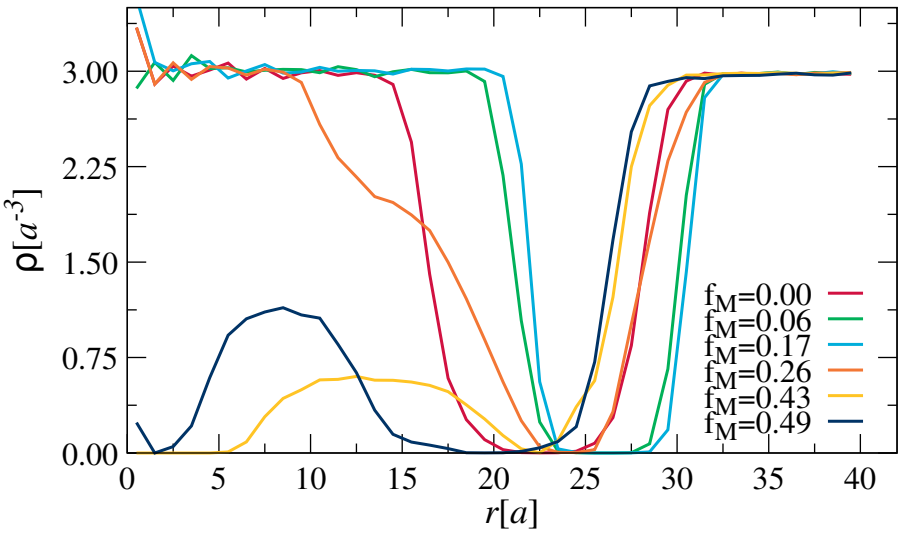

Figure 44: Radial density distribution of water beads, for tb-MEO at different fractions of hydrophilic M block as a function of distance from vesicle COM.

44) for different f_M. The plot also shows that the increase in f_M changes the vesicle formation. For $f_M \geqslant 0.26$ the flat-bottomed valley profile of water beads is distorted. This is because the increase of f_M and decrease of f_O increases the overall hydrophobicity of the system, due to which the formation of the vesicular structure is less favored. It is also important to note that depending on the interaction ($\chi - parameter$) of the hydrophilic block with water, the polymeric vesicle formation range is different for

different polymers. The deviation in forming a vesicle with increasing M block and decreasing O block is explained by the change in the nanostructure formation for diblocks when the length of the hydrophilic block is altered.

Here, the increase in M block length also induces a shape anisotropy. To quantify it, we plotted the relative shape anisotropy (κ^2), which is calculated from the diagonal elements of the gyration tensor, $\kappa^2 = 1.5\,(\lambda_x{}^2 + \lambda_y{}^2 + \lambda_z{}^2/(\lambda_x + \lambda_y + \lambda_z)^2)) - 0.5$, where λ_x, λ_y, λ_z are the principal moments of the square of gyration tensor. The relative shape anisotropy is bound to be between zero and one; when $\kappa^2 = 0$ then all the particles lie on a sphere, and when it is $\kappa^2 = 1$ then they lie on a straight line.

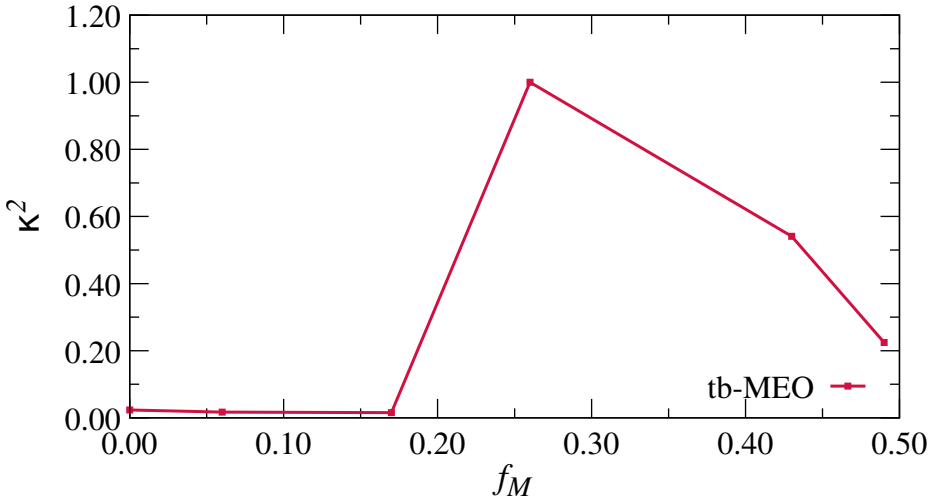

Figure 45: Relative shape anisotropy for tb-MEO at varied fractions of hydrophilic M block, normalized to the maximum value.

Figure 45 shows, for a small fraction of hydrophilic M block, the relative shape anisotropy has a lower value ≈ 0, summarizing a spherical shape for the nanostructure. For $f_M > 0.17$, the shape anisotropy has a higher value, showing a deviation from the spherical shape. Again, we observe a decrease in the relative shape anisotropy when we increase f_M further above 0.26. This is because increasing the concentration of M block and decreasing O to a certain extent promotes micellar structure, due to which an increasing amount of f_M accounts for a smaller cavity. The cavity is not present in the vesicle center but is radially shifted, due to which the pressure from the water present in the cavity is not homogeneous, which distorts

the vesicle's shape. A lower concentration of O balances the increase in M, which reduces the distortion of shape and promotes vesicle formation, due to which the shape anisotropy decreases.

7.4 CONCLUSIONS

We have performed DPD simulations to study the self-assembly of amphiphilic triblock terpolymers in an aqueous solution. Our results show that the arrangement of hydrophobic/hydrophilic blocks in a triblock terpolymer influences the patchy polymerosome. Specifically, when the hydrophobic block is present in the center of the two hydrophilic blocks, the cavity size increases, and the wall thickness decreases, compared to the one when the hydrophobic block is at one end, the same is observed for the miktoarm. Moreover, the patches formed on the inner and outer surface change with the arrangement of the blocks from a distant island-like to a bi-continuous one. The length of the hydrophilic blocks changes the shape of the polymerosome from spherical to ellipsoidal, along with decreasing its cavity size and changing the surface patchiness.

Here, we did not explore the size of the particle, but we do propose to control the size by adding specific surfactant or homopolymer to the system, which can inhibit the growth of such polymerosomes. Overall, this investigation paves the way for designing the patchy polymerosomes with different volume fractions of solvent inside and distinct patches on the surface. This can aid in enhancing the on-target effects in drug delivery applications.

8

GENERAL CONCLUSIONS

In this thesis work, we have used different simulation techniques to investigate the segregation behavior of the polymer systems. In the flow-based separation study, we have employed a hybrid simulation approach due to the different length scales of the polymer and the solvent particles, while for the phase separation of the multiblock copolymers, we have utilized a coarse-grained simulation technique for polymers in the bulk and solution.

We have realized a means to separate polymers based on the macromolecular architecture in a pressure-driven flow. Wherein the cross-stream migration of polymers within the slit channel was explored. The star polymer in infinite dilution experiences a powerful lift force and moves to the channel center compared to its linear counterpart of the same size. Our simulation has shown that the cross-stream separation of polymer mixture arises from a combination of wall induced hydrodynamic lift and viscoelastic forces originating from the linear chains. The phenomenon observed here is similar to the viscoelastic focusing of the rigid colloids.

Furthermore, we have highlighted the different self-assembled morphologies of ABC triblock terpolymer with hPB blending. Here, the morphological evolution of the sandwiched B phase goes from cylinders to perforated lamellae and finally to continuous lamellae with increasing homopolymer volume fraction. We recognized that the distribution of homopolymer (hPB) is uniform throughout the B phase. Our simulations are in perfect agreement with experimental observations regarding morphological progression and transitions. This simulation-driven approach helps to gain useful insight into sandwiched B microphase formation and its stability and offers directions to target specific morphologies for other ABC/B terpolymer blends. This blending route will provide access to a vast library of different morphologies of triblock systems depending on the used ABC triblock terpolymer.

We also exhibited the self-assembly of triblock terpolymer in an aqueous solution and showcased the evaporation-induced confinement assembly of triblock ABC blended systems. Our simulation gave valuable insights on self-assembly in double confinement *i.e.*, in three-dimensional microparticles with two-dimensional, confined polymer lamellae. We reported the morphological transition of the B microphase from concentric rings to perforated lamellae to lamellae, which is in agreement with the experiments. We presented the different confined morphologies obtained via blending in solution.

Finally, we have presented the phase separation based on the different architecture of the triblock copolymer and showcased its influence on the self-assembled morphologies. We have demonstrated that the arrangement of the hydrophilic block resulted in different kinds of self-assembled structures, from polymeric vesicle to micelle. Moreover, we have shown the effect of the hydrophilic block length on the cavity size and surface patches. This investigation paves the way to design patchy polymerosomes with different cavity sizes and patches, which can enhance the on-target effects in drug delivery applications.

The hybrid simulation methodology used here represents a roadmap to study flow-based separation and phase separation of polymers. So far, most of the experimental research concentrates on the self-assembly of polymers constituting three blocks, but our simulation methodology can be used to study polymers with three or more blocks. This computational strategy can be further applied to systematically explore different architectures rather than star or chain polymer. Overall, this work can aid in the development of future materials with more intricate morphologies of multiblock polymers.

BIBLIOGRAPHY

[1] Jay Hoon Park and Gregory C Rutledge. "50th anniversary perspective: Advanced polymer fibers: High performance and ultrafine." In: *Macromolecules* 50.15 (2017), pp. 5627–5642.

[2] Christopher M Bates and Frank S Bates. "50th Anniversary Perspective: Block Polymers Pure Potential." In: *Macromolecules* 50.1 (2017), pp. 3–22.

[3] Roland Geyer, Jenna R Jambeck, and Kara Lavender Law. "Production, use, and fate of all plastics ever made." In: *Science advances* 3.7 (2017), e1700782.

[4] Nitin H Mutha, Martin Patel, and V Premnath. "Plastics materials flow analysis for India." In: *Resources, conservation and recycling* 47.3 (2006), pp. 222–244.

[5] Ronald G Larson. *The structure and rheology of complex fluids*. Vol. 150. Oxford university press New York, 1999.

[6] Robert Byron Bird, Charles F Curtiss, Robert C Armstrong, and Ole Hassager. *Dynamics of polymeric liquids, volume 2: Kinetic theory*. Wiley, 1987.

[7] Todd M Squires and Stephen R Quake. "Microfluidics: Fluid physics at the nanoliter scale." In: *Reviews of modern physics* 77.3 (2005), p. 977.

[8] Xing Chen, Chang Chun Liu, Hui Li, et al. "Microfluidic chip for blood cell separation and collection based on crossflow filtration." In: *Sensors and Actuators B: Chemical* 130.1 (2008), pp. 216–221.

[9] Timm Krüger, David Holmes, and Peter V Coveney. "Deformability-based red blood cell separation in deterministic lateral displacement devices—A simulation study." In: *Biomicrofluidics* 8.5 (2014), p. 054114.

[10] Arash Nikoubashman and Christos N Likos. "Branched polymers under shear." In: *Macromolecules* 43.3 (2010), pp. 1610–1620.

[11] Sunil P Singh, Gerhard Gompper, and Roland G Winkler. "Steady state sedimentation of ultrasoft colloids." In: *The Journal of chemical physics* 148.8 (2018), p. 084901.

[12] Douglas E Smith, Hazen P Babcock, and Steven Chu. "Single-polymer dynamics in steady shear flow." In: *Science* 283.5408 (1999), pp. 1724–1727.

[13] Sergiy Gerashchenko and Victor Steinberg. "Statistics of tumbling of a single polymer molecule in shear flow." In: *Physical review letters* 96.3 (2006), p. 038304.

[14] Philip LeDuc, Charbel Haber, Gang Bao, and Denis Wirtz. "Dynamics of individual flexible polymers in a shear flow." In: *Nature* 399.6736 (1999), pp. 564–566.

[15] Subra Suresh. "Biomechanics and biophysics of cancer cells." In: *Acta biomaterialia* 3.4 (2007), pp. 413–438.

[16] Leonard A Herzenberg, Richard G Sweet, and Leonore A Herzenberg. "Fluorescence-activated cell sorting." In: *Scientific American* 234.3 (1976), pp. 108–118.

[17] Jan Krüger, Kirat Singh, Alan O'Neill, Carl Jackson, Alan Morrison, and Peter O'Brien. "Development of a microfluidic device for fluorescence activated cell sorting." In: *Journal of micromechanics and microengineering* 12.4 (2002), p. 486.

[18] WA Bonner, HR Hulett, RG Sweet, and LA Herzenberg. "Fluorescence activated cell sorting." In: *Review of Scientific Instruments* 43.3 (1972), pp. 404–409.

[19] Nicole Pamme. "Continuous flow separations in microfluidic devices." In: *Lab on a Chip* 7.12 (2007), pp. 1644–1659.

[20] Daniel R Gossett, Westbrook M Weaver, Albert J Mach, Soojung Claire Hur, Henry Tat Kwong Tse, Wonhee Lee, Hamed Amini, and Dino Di Carlo. "Label-free cell separation and sorting in microfluidic systems." In: *Analytical and bioanalytical chemistry* 397.8 (2010), pp. 3249–3267.

[21] Andreas Lenshof and Thomas Laurell. "Continuous separation of cells and particles in microfluidic systems." In: *Chemical Society Reviews* 39.3 (2010), pp. 1203–1217.

[22] A Karimi, S Yazdi, and AM Ardekani. "Hydrodynamic mechanisms of cell and particle trapping in microfluidics." In: *Biomicrofluidics* 7.2 (2013), p. 021501.

[23] CN Likos, H Löwen, M Watzlawek, B Abbas, O Jucknischke, J Allgaier, and D Richter. "Star polymers viewed as ultrasoft colloidal particles." In: *Physical review letters* 80.20 (1998), p. 4450.

[24] Ian W Hamley. *Developments in block copolymer science and technology*. John Wiley & Sons, 2004.

[25] Frank S Bates and Glenn H Fredrickson. "Block copolymer thermodynamics: theory and experiment." In: *Annual review of physical chemistry* 41.1 (1990), pp. 525–557.

[26] Frank S Bates. "Network phases in block copolymer melts." In: *MRS bulletin* 30.7 (2005), pp. 525–532.

[27] Georg Krausch and Robert Magerle. "Nanostructured thin films via self-assembly of block copolymers." In: *Advanced Materials* 14.21 (2002), pp. 1579–1583.

[28] PF Onyon. *Textbook of polymer science: Fred W. Billmeyer, Jr., Wiley—Interscience, New York, 2nd edn, 1971, 598 pp.£ 7.50 (paper,£ 4.30)*. 1972.

[29] Munmaya Mishra and Shiro Kobayashi. *Star and hyperbranched polymers*. Vol. 53. CRC Press, 1999.

[30] Marshall Fixman. "Radius of gyration of polymer chains." In: *The Journal of Chemical Physics* 36.2 (1962), pp. 306–310.

[31] Paul J Flory and M Volkenstein. "Statistical mechanics of chain molecules." In: *Biopolymers: Original Research on Biomolecules* 8.5 (1969), pp. 699–700.

[32] Michael P Howard, Arash Nikoubashman, and Athanassios Z Panagiotopoulos. "Stratification in Drying Polymer–Polymer and Colloid–Polymer Mixtures." In: *Langmuir* 33.42 (2017), pp. 11390–11398.

[33] Iwao Teraoka. *Polymer solutions*. John Wiley & Sons, Inc, 2002.

[34] Hugo Hernandez. "Clausius' sphere of action for different intermolecular potentials." In: *ForsChem Research Reports* 10 (2017).

[35] JE Mayer and M Goeppert. "Mayer, Statistical Mechanics." In: *JohnW iley & Sons, New York* (1940).

[36] WH Stockmayer and HE Stanley. "Light-scattering measurement of interactions between unlike polymers." In: *The Journal of Chemical Physics* 18.1 (1950), pp. 153–154.

[37] Wenlin Zhang, Enrique D Gomez, and Scott T Milner. "Predicting Flory-Huggins χ from simulations." In: *Physical review letters* 119.1 (2017), p. 017801.

[38] Paul J Flory. *Principles of polymer chemistry*. Cornell University Press, 1953.

[39] Michael Rubinstein, Ralph H Colby, et al. *Polymer physics*. Vol. 23. Oxford university press New York, 2003.

[40] Pierre-Gilles De Gennes and Pierre-Gilles Gennes. *Scaling concepts in polymer physics*. Cornell university press, 1979.

[41] M Doi and SF Edwards. "The theory of polymer dynamics Oxford University Press (Clarendon) London New York." In: (1986).

[42] James G Mitchell and Kazuhiro Kogure. "Bacterial motility: links to the environment and a driving force for microbial physics." In: *FEMS microbiology ecology* 55.1 (2006), pp. 3–16.

[43] Don S Lemons and Anthony Gythiel. "Paul langevin's 1908 paper "on the theory of brownian motion"["sur la théorie du mouvement brownien," cr acad. sci.(paris) 146, 530–533 (1908)]." In: *American Journal of Physics* 65.11 (1997), pp. 1079–1081.

[44] Pierre-Henri Chavanis. "Generalized Euler, Smoluchowski and Schrödinger equations admitting self-similar solutions with a Tsallis invariant profile." In: *The European Physical Journal Plus* 134.7 (2019), p. 353.

[45] Rep Kubo. "The fluctuation-dissipation theorem." In: *Reports on progress in physics* 29.1 (1966), p. 255.

[46] J Weber. "Fluctuation dissipation theorem." In: *Physical Review* 101.6 (1956), p. 1620.

[47] Olaf Sparre Andersen. "Sequencing and the single channel." In: *Biophysical journal* 77.6 (1999), p. 2899.

[48] Chia-Fu Chou, Robert H Austin, Olgica Bakajin, Jonas O Tegenfeldt, Judith A Castelino, Shirley S Chan, Edward C Cox, Harold Craighead, Nicholas Darnton, Thomas Duke, et al. "Sorting biomolecules with microdevices." In: *ELECTROPHORESIS: An International Journal* 21.1 (2000), pp. 81–90.

[49] Alex Lim, Eileen T Dimalanta, Konstantinos D Potamousis, Galex Yen, Jennifer Apodoca, Chunhong Tao, Jieyi Lin, Rong Qi, John Skiadas, Arvind Ramanathan, et al. "Shotgun optical maps of the whole Escherichia coli O157: H7 genome." In: *Genome Research* 11.9 (2001), pp. 1584–1593.

[50] Nicole T Perna, Guy Plunkett, Valerie Burland, Bob Mau, Jeremy D Glasner, Debra J Rose, George F Mayhew, Peter S Evans, Jason Gregor, Heather A Kirkpatrick, et al. "Genome sequence of enterohaemorrhagic Escherichia coli O157: H7." In: *Nature* 409.6819 (2001), pp. 529–533.

[51] M Hinz, S Gura, B Nitzan, S Margel, and H Seliger. "Polymer support for exonucleolytic sequencing." In: *Journal of biotechnology* 86.3 (2001), pp. 281–288.

[52] Sho Asakura and Fumio Oosawa. "On interaction between two bodies immersed in a solution of macromolecules." In: *The Journal of chemical physics* 22.7 (1954), pp. 1255–1256.

[53] James H Aubert and Matthew Tirrell. "Effective viscosity of dilute polymer solutions near confining boundaries." In: *The Journal of Chemical Physics* 77.1 (1982), pp. 553–561.

[54] D Ausserre, H Hervet, and F Rondelez. "Concentration dependence of the interfacial depletion layer thickness for polymer solutions in contact with nonadsorbing walls." In: *Macromolecules* 19.1 (1986), pp. 85–88.

[55] US Agarwal, A Dutta, and RA Mashelkar. "Migration of macromolecules under flow: the physical origin and engineering implications." In: *Chemical Engineering Science* 49.11 (1994), pp. 1693–1717.

[56] Myung S Jhon and Karl F Freed. "Polymer migration in Newtonian fluids." In: *Journal of Polymer Science: Polymer Physics Edition* 23.5 (1985), pp. 955–971.

[57] Hongbo Ma and Michael D Graham. "Theory of shear-induced migration in dilute polymer solutions near solid boundaries." In: *Physics of Fluids* 17.8 (2005), p. 083103.

[58] Juan P Hernández-Ortiz, Hongbo Ma, Juan J de Pablo, and Michael D Graham. "Cross-stream-line migration in confined flowing polymer solutions: Theory and simulation." In: *Physics of Fluids* 18.12 (2006), p. 123101.

[59] Eva Blasco, Michael B Sims, Anja S Goldmann, Brent S Sumerlin, and Christopher Barner-Kowollik. "50th anniversary perspective: Polymer functionalization." In: *Macromolecules* 50.14 (2017), pp. 5215–5252.

[60] Volker Abetz and Peter FW Simon. "Phase behaviour and morphologies of block copolymers." In: *Block copolymers I*. Springer, 2005, pp. 125–212.

[61] JN Israelachvili. *Intermolecular and surface forces, Thirdth edn*. 2011.

[62] Celesta Fong, Tu Le, and Calum J Drummond. "Lyotropic liquid crystal engineering–ordered nanostructured small molecule amphiphile self-assembly materials by design." In: *Chemical Society Reviews* 41.3 (2012), pp. 1297–1322.

[63] Shrirang V Ranade, Kathleen M Miller, Robert E Richard, A Ken Chan, Michael J Allen, and Michael N Helmus. "Physical characterization of controlled release of paclitaxel from the TAXUS™ Express2™ drug-eluting stent." In: *Journal of Biomedical Materials Research Part A* 71.4 (2004), pp. 625–634.

[64] Seth B Darling. "Block copolymers for photovoltaics." In: *Energy & Environmental Science* 2.12 (2009), pp. 1266–1273.

[65] Weichao Shi, Yuichi Tateishi, Wei Li, Craig J Hawker, Glenn H Fredrickson, and Edward J Kramer. "Producing small domain features using miktoarm block copolymers with large interaction parameters." In: *ACS Macro Letters* 4.11 (2015), pp. 1287–1292.

[66] Annette Rösler, Guido WM Vandermeulen, and Harm-Anton Klok. "Advanced drug delivery devices via self-assembly of amphiphilic block copolymers." In: *Advanced drug delivery reviews* 64 (2012), pp. 270–279.

[67] Zachary L Tyrrell, Youqing Shen, and Maciej Radosz. "Fabrication of micellar nanoparticles for drug delivery through the self-assembly of block copolymers." In: *Progress in Polymer Science* 35.9 (2010), pp. 1128–1143.

[68] Gurusamy Saravanakumar, Hyeongmok Park, Jinhwan Kim, Dongsik Park, Swapan Pramanick, Dae Heon Kim, and Won Jong Kim. "Miktoarm amphiphilic block copolymer with singlet oxygen-labile stereospecific β-aminoacrylate junction: Synthesis, self-assembly, and photodynamically triggered drug release." In: *Biomacromolecules* 19.6 (2018), pp. 2202–2213.

[69] Wen-Jian Zhang, Chun-Yan Hong, and Cai-Yuan Pan. "Polymerization-induced self-assembly of functionalized block copolymer nanoparticles and their application in drug delivery." In: *Macromolecular rapid communications* 40.2 (2019), p. 1800279.

[70] Ho-Cheol Kim, Sang-Min Park, and William D Hinsberg. "Block copolymer based nanostructures: materials, processes, and applications to electronics." In: *Chemical reviews* 110.1 (2010), pp. 146–177.

[71] Frank S Bates and GH Fredrickson. "Block copolymers-designer soft materials." In: *Physics today* 52 (2000).

[72] Erin M Lennon, Kirill Katsov, and Glenn H Fredrickson. "Free energy evaluation in field-theoretic polymer simulations." In: *Physical review letters* 101.13 (2008), p. 138302.

[73] Mark W Matsen and Frank S Bates. "Origins of complex self-assembly in block copolymers." In: *Macromolecules* 29.23 (1996), pp. 7641–7644.

[74] Justin E Poelma, Kosuke Ono, Daigo Miyajima, Takuzo Aida, Kotaro Satoh, and Craig J Hawker. "Cyclic block copolymers for controlling feature sizes in block copolymer lithography." In: *ACS nano* 6.12 (2012), pp. 10845–10854.

[75] Kay EB Doncom, Lewis D Blackman, Daniel B Wright, Matthew I Gibson, and Rachel K O'Reilly. "Dispersity effects in polymer self-assemblies: a matter of hierarchical control." In: *Chemical Society Reviews* 46.14 (2017), pp. 4119–4134.

[76] Zuojun Guo, Guojie Zhang, Feng Qiu, Hongdong Zhang, Yuliang Yang, and An-Chang Shi. "Discovering ordered phases of block copolymers: New results from a generic Fourier-space approach." In: *Physical review letters* 101.2 (2008), p. 028301.

[77] Yasuhiro Mogi, Hiroyuki Kotsuji, Yuji Kaneko, Katsuaki Mori, Yushu Matsushita, and Ichiro Noda. "Preparation and morphology of triblock copolymers of the ABC type." In: *Macromolecules* 25.20 (1992), pp. 5408–5411.

[78] Yasuhiro Mogi, Katsuaki Mori, Yushu Matsushita, and Ichiro Noda. "Tricontinuous morphology of triblock copolymers of the ABC type." In: *Macromolecules* 25.20 (1992), pp. 5412–5415.

[79] Rajeev Kumar, Scott W Sides, Monojoy Goswami, Bobby G Sumpter, Kunlun Hong, Xiaodong Wu, Thomas P Russell, Samuel P Gido, Konstantinos Misichronis, Sofia Rangou, et al. "Morphologies of ABC Triblock Terpolymer Melts Containing Poly (Cyclohexadiene): Effects of Conformational Asymmetry." In: *Langmuir* 29.6 (2013), pp. 1995–2006.

[80] Clemens Auschra and Reimund Stadler. "New ordered morphologies in ABC triblock copolymers." In: *Macromolecules* 26.9 (1993), pp. 2171–2174.

[81] Jörg Beckmann, Clemens Auschra, and Reimund Stadler. ""Ball at the wall"—A new lamellar multiphase morphology in a polystyrene-block-polybutadiene-block-poly (methyl methacrylate) triblock copolymer." In: *Macromolecular rapid communications* 15.1 (1994), pp. 67–72.

[82] Ulrike Breiner, Udo Krappe, and Reimund Stadler. "Evolution of the "knitting pattern" morphology in ABC triblock copolymers." In: *Macromolecular rapid communications* 17.8 (1996), pp. 567–575.

[83] Thomas H Epps, Eric W Cochran, Travis S Bailey, Ryan S Waletzko, Cordell M Hardy, and Frank S Bates. "Ordered network phases in linear poly (isoprene-b-

styrene-b-ethylene oxide) triblock copolymers." In: *Macromolecules* 37.22 (2004), pp. 8325–8341.

[84] MP Allen and DJ Tildesley. "Molecular Simulation of Liquids." In: *Clarendon, Oxford* (1987).

[85] Florian Müller-Plathe. "Coarse-graining in polymer simulation: from the atomistic to the mesoscopic scale and back." In: *ChemPhysChem* 3.9 (2002), pp. 754–769.

[86] E Moeendarbary, TY Ng, and M Zangeneh. "Dissipative particle dynamics: introduction, methodology and complex fluid applications—a review." In: *International Journal of Applied Mechanics* 1.04 (2009), pp. 737–763.

[87] Michael P Allen et al. "Introduction to molecular dynamics simulation." In: *Computational soft matter: from synthetic polymers to proteins* 23 (2004), pp. 1–28.

[88] Daan Frenkel and Berend Smit. *Understanding molecular simulation: from algorithms to applications*. Vol. 1. Elsevier, 2001.

[89] Loup Verlet. "Computer" experiments" on classical fluids. I. Thermodynamical properties of Lennard-Jones molecules." In: *Physical review* 159.1 (1967), p. 98.

[90] Daan Frenkel and Berend Smit. *Understanding molecular simulation: From algorithms to applications*. 2002.

[91] Michael P Allen and Dominic J Tildesley. *Computer simulation of liquids*. Oxford university press, 2017.

[92] Anatoly Malevanets and Raymond Kapral. "Mesoscopic model for solvent dynamics." In: *The Journal of chemical physics* 110.17 (1999), pp. 8605–8613.

[93] T Ihle and DM Kroll. "Stochastic rotation dynamics: A Galilean-invariant mesoscopic model for fluid flow." In: *Physical Review E* 63.2 (2001), p. 020201.

[94] Michael P Howard, Arash Nikoubashman, and Jeremy C Palmer. "Modeling hydrodynamic interactions in soft materials with multiparticle collision dynamics." In: *Current Opinion in Chemical Engineering* 23 (2019), pp. 34–43.

[95] Ingo O Götze, Hiroshi Noguchi, and Gerhard Gompper. "Relevance of angular momentum conservation in mesoscale hydrodynamics simulations." In: *Physical Review E* 76.4 (2007), p. 046705.

[96] Hiroshi Noguchi, Norio Kikuchi, and Gerhard Gompper. "Particle-based mesoscale hydrodynamic techniques." In: *EPL (Europhysics Letters)* 78.1 (2007), p. 10005.

[97] E Allahyarov and G Gompper. "Erratum: Mesoscopic solvent simulations: Multiparticle-collision dynamics of three-dimensional flows [Phys. Rev. E 66, 036702 (2002)]." In: *Physical Review E* 67.5 (2003), p. 059901.

[98] PJ Hoogerbrugge and JMVA Koelman. "Simulating microscopic hydrodynamic phenomena with dissipative particle dynamics." In: *EPL (Europhysics Letters)* 19.3 (1992), p. 155.

[99] Pep Espanol and Patrick Warren. "Statistical mechanics of dissipative particle dynamics." In: *EPL (Europhysics Letters)* 30.4 (1995), p. 191.

[100] Robert D Groot and KL Rabone. "Mesoscopic simulation of cell membrane damage, morphology change and rupture by nonionic surfactants." In: *Biophysical journal* 81.2 (2001), pp. 725–736.

[101] Pep Espanol. "Dissipative particle dynamics with energy conservation." In: *EPL (Europhysics Letters)* 40.6 (1997), p. 631.

[102] Michael P Allen and Friederike Schmid. "A thermostat for molecular dynamics of complex fluids." In: *Molecular Simulation* 33.1-2 (2007), pp. 21–26.

[103] Simeon D Stoyanov and Robert D Groot. "From molecular dynamics to hydrodynamics: a novel Galilean invariant thermostat." In: *The Journal of chemical physics* 122.11 (2005), p. 114112.

[104] Robert D Groot. "A local Galilean invariant thermostat." In: *Journal of chemical theory and computation* 2.3 (2006), pp. 568–574.

[105] Robert D Groot and Patrick B Warren. "Dissipative particle dynamics: Bridging the gap between atomistic and mesoscopic simulation." In: *The Journal of chemical physics* 107.11 (1997), pp. 4423–4435.

[106] Eric E Keaveny, Igor V Pivkin, Martin Maxey, and George Em Karniadakis. "A comparative study between dissipative particle dynamics and molecular dynamics for simple-and complex-geometry flows." In: *The Journal of chemical physics* 123.10 (2005), p. 104107.

[107] Camilo Cruz, Francisco Chinesta, and Gilles Regnier. "Review on the Brownian dynamics simulation of bead-rod-spring models encountered in computational rheology." In: *Archives of Computational Methods in Engineering* 19.2 (2012), pp. 227–259.

[108] Yelena R Sliozberg, Timothy W Sirk, John K Brennan, and Jan W Andzelm. "Bead-spring models of entangled polymer melts: Comparison of hard-core and soft-core potentials." In: *Journal of Polymer Science Part B: Polymer Physics* 50.24 (2012), pp. 1694–1698.

[109] Robert C Armstrong. "Kinetic theory and rheology of dilute solutions of flexible macromolecules. I. Steady state behavior." In: *The Journal of Chemical Physics* 60.3 (1974), pp. 724–728.

[110] Dmitry A Fedosov, Julia Fornleitner, and Gerhard Gompper. "Margination of white blood cells in microcapillary flow." In: *Physical review letters* 108.2 (2012), p. 028104.

[111] Seungyoung Yang, Sung Sik Lee, Sung Won Ahn, Kyowon Kang, Wooyoung Shim, Gwang Lee, Kyu Hyun, and Ju Min Kim. "Deformability-selective particle entrainment and separation in a rectangular microchannel using medium viscoelasticity." In: *Soft Matter* 8.18 (2012), pp. 5011–5019.

[112] Gaetano D'Avino, Giovanni Romeo, Massimiliano M Villone, Francesco Greco, Paolo A Netti, and Pier Luca Maffettone. "Single line particle focusing induced by viscoelasticity of the suspending liquid: theory, experiments and simulations to design a micropipe flow-focuser." In: *Lab on a Chip* 12.9 (2012), pp. 1638–1645.

[113] J McGrath, M Jimenez, and H Bridle. "Deterministic lateral displacement for particle separation: a review." In: *Lab on a Chip* 14.21 (2014), pp. 4139–4158.

[114] Kerwin Kwek Zeming, Thoriq Salafi, Chia-Hung Chen, and Yong Zhang. "Asymmetrical deterministic lateral displacement gaps for dual functions of enhanced separation and throughput of red blood cells." In: *Scientific reports* 6 (2016), p. 22934.

[115] P Sajeesh and Ashis Kumar Sen. "Particle separation and sorting in microfluidic devices: a review." In: *Microfluidics and nanofluidics* 17.1 (2014), pp. 1–52.

[116] Gina S Fiorini and Daniel T Chiu. "Disposable microfluidic devices: fabrication, function, and application." In: *BioTechniques* 38.3 (2005), pp. 429–446.

[117] Rajesh Khare, Michael D Graham, and Juan J de Pablo. "Cross-stream migration of flexible molecules in a nanochannel." In: *Physical review letters* 96.22 (2006), p. 224505.

[118] L Cannavacciuolo, RG Winkler, and G Gompper. "Mesoscale simulations of polymer dynamics in microchannel flows." In: *EPL (Europhysics Letters)* 83.3 (2008), p. 34007.

[119] Christos N Likos. "Effective interactions in soft condensed matter physics." In: *Physics Reports* 348.4-5 (2001), pp. 267–439.

[120] Dimitris Vlassopoulos, George Fytas, Tadeusz Pakula, and Jacques Roovers. "Multiarm star polymers dynamics." In: *Journal of Physics: Condensed Matter* 13.41 (2001), R855.

[121] Dimitris Vlassopoulos and Michel Cloitre. "Tunable rheology of dense soft deformable colloids." In: *Current opinion in colloid & interface science* 19.6 (2014), pp. 561–574.

[122] Sunil P Singh, Roland G Winkler, and Gerhard Gompper. "Nonequilibrium forces between dragged ultrasoft colloids." In: *Physical review letters* 107.15 (2011), p. 158301.

[123] John D Weeks, David Chandler, and Hans C Andersen. "Role of repulsive forces in determining the equilibrium structure of simple liquids." In: *The Journal of chemical physics* 54.12 (1971), pp. 5237–5247.

[124] Kurt Kremer and Gary S Grest. "Dynamics of entangled linear polymer melts: A molecular-dynamics simulation." In: *The Journal of Chemical Physics* 92.8 (1990), pp. 5057–5086.

[125] Arash Nikoubashman and Christos N Likos. "Flow-induced polymer translocation through narrow and patterned channels." In: *The Journal of chemical physics* 133.7 (2010), p. 074901.

[126] G Gompper, T Ihle, DM Kroll, and RG Winkler. "Multi-particle collision dynamics: A particle-based mesoscale simulation approach to the hydrodynamics of complex fluids." In: *Advanced computer simulation approaches for soft matter sciences III* (2009), pp. 1–87.

[127] Chien-Cheng Huang, Gerhard Gompper, and Roland G Winkler. "Hydrodynamic correlations in multiparticle collision dynamics fluids." In: *Physical Review E* 86.5 (2012), p. 056711.

[128] E Allahyarov and G Gompper. "Mesoscopic solvent simulations: Multiparticle-collision dynamics of three-dimensional flows." In: *Physical Review E* 66.3 (2002), p. 036702.

[129] A Lamura, G Gompper, T Ihle, and DM Kroll. "Erratum: Multi-particle collision dynamics: Flow around a circular and a square cylinder." In: *Europhysics Letters* 56.5 (2001), pp. 768–768.

[130] Arash Nikoubashman, Nathan A Mahynski, Michael P Howard, and Athanassios Z Panagiotopoulos. "Erratum: Flow-induced demixing of polymer-colloid mixtures in microfluidic channels [J. Chem. Phys. 140, 094903 (2014)]." In: *The Journal of Chemical Physics* 141.14 (2014), p. 149906.

[131] Michael P Howard, Athanassios Z Panagiotopoulos, and Arash Nikoubashman. "Inertial and viscoelastic forces on rigid colloids in microfluidic channels." In: *The Journal of chemical physics* 142.22 (2015), p. 224908.

[132] Jae Young Kim, Sung Won Ahn, Sung Sik Lee, and Ju Min Kim. "Lateral migration and focusing of colloidal particles and DNA molecules under viscoelastic flow." In: *Lab on a Chip* 12.16 (2012), pp. 2807–2814.

[133] Arash Nikoubashman and Michael P Howard. "Equilibrium dynamics and shear rheology of semiflexible polymers in solution." In: *Macromolecules* 50.20 (2017), pp. 8279–8289.

[134] Marisol Ripoll, K Mussawisade, RG Winkler, and G Gompper. "Dynamic regimes of fluids simulated by multiparticle-collision dynamics." In: *Physical Review E* 72.1 (2005), p. 016701.

[135] Joshua A Anderson, Chris D Lorenz, and Alex Travesset. "General purpose molecular dynamics simulations fully implemented on graphics processing units." In: *Journal of computational physics* 227.10 (2008), pp. 5342–5359.

[136] Jens Glaser, Trung Dac Nguyen, Joshua A Anderson, Pak Lui, Filippo Spiga, Jaime A Millan, David C Morse, and Sharon C Glotzer. "Strong scaling of general-purpose molecular dynamics simulations on GPUs." In: *Computer Physics Communications* 192 (2015), pp. 97–107.

[137] Michael P Howard, Joshua A Anderson, Arash Nikoubashman, Sharon C Glotzer, and Athanassios Z Panagiotopoulos. "Efficient neighbor list calculation for molecular simulation of colloidal systems using graphics processing units." In: *Computer Physics Communications* 203 (2016), pp. 45–52.

[138] Jonas Riest, Labrini Athanasopoulou, Sergei A Egorov, Christos N Likos, and Primož Ziherl. "Elasticity of polymeric nanocolloidal particles." In: *Scientific reports* 5.1 (2015), pp. 1–12.

[139] Raghunath Chelakkot, Roland G Winkler, and Gerhard Gompper. "Migration of semiflexible polymers in microcapillary flow." In: *EPL (Europhysics Letters)* 91.1 (2010), p. 14001.

[140] S Reddig and H Stark. "Cross-streamline migration of a semiflexible polymer in a pressure driven flow." In: *The Journal of chemical physics* 135.16 (2011), 10B620.

[141] M Ripoll, RG Winkler, and G Gompper. "Star polymers in shear flow." In: *Physical review letters* 96.18 (2006), p. 188302.

[142] Chien-Cheng Huang, Roland G Winkler, Godehard Sutmann, and Gerhard Gompper. "Semidilute polymer solutions at equilibrium and under shear flow." In: *Macromolecules* 43.23 (2010), pp. 10107–10116.

[143] Bruno H Zimm. "Dynamics of polymer molecules in dilute solution: viscoelasticity, flow birefringence and dielectric loss." In: *The journal of chemical physics* 24.2 (1956), pp. 269–278.

[144] Gary S Grest, Kurt Kremer, Scott Thomas Milner, and TA Witten. "Relaxation of self-entangled many-arm star polymers." In: *Macromolecules* 22.4 (1989), pp. 1904–1910.

[145] Deepika Srivastva and Arash Nikoubashman. "Flow behavior of chain and star polymers and their mixtures." In: *Polymers* 10.6 (2018), p. 599.

[146] Philip R Wohl and SI Rubinow. "The transverse force on a drop in an unbounded parabolic flow." In: *Journal of Fluid Mechanics* 62.1 (1974), pp. 185–207.

[147] PC-H Chan and LG Leal. "The motion of a deformable drop in a second-order fluid." In: *Journal of Fluid Mechanics* 92.1 (1979), pp. 131–170.

[148] Ryan L Marson, Yuanding Huang, Ming Huang, Taotao Fu, and Ronald G Larson. "Inertio-capillary cross-streamline drift of droplets in Poiseuille flow using dissipative particle dynamics simulations." In: *Soft Matter* 14.12 (2018), pp. 2267–2280.

[149] Christian Schaaf and Holger Stark. "Inertial migration and axial control of deformable capsules." In: *Soft Matter* 13.19 (2017), pp. 3544–3555.

[150] John W Perram and Lee R White. "Structure of the liquid/vapour and liquid/solid interfaces." In: *Faraday Discussions of the Chemical Society* 59 (1975), pp. 29–37.

[151] Douglas Henderson, Farid F Abraham, and John A Barker. "The Ornstein-Zernike equation for a fluid in contact with a surface." In: *Molecular Physics* 31.4 (1976), pp. 1291–1295.

[152] Ian K Snook and Douglas Henderson. "Monte Carlo study of a hard-sphere fluid near a hard wall." In: *The Journal of Chemical Physics* 68.5 (1978), pp. 2134–2139.

[153] Michael P Howard, Aishwarya Gautam, Athanassios Z Panagiotopoulos, and Arash Nikoubashman. "Axial dispersion of Brownian colloids in microfluidic channels." In: *Physical Review Fluids* 1.4 (2016), p. 044203.

[154] K Devanand and JC Selser. "Asymptotic behavior and long-range interactions in aqueous solutions of poly (ethylene oxide)." In: *Macromolecules* 24.22 (1991), pp. 5943–5947.

[155] Edward JW Crossland, Marleen Kamperman, Mihaela Nedelcu, Caterina Ducati, Ulrich Wiesner, Detlef-M Smilgies, Gilman ES Toombes, Marc A Hillmyer, Sabine Ludwigs, Ullrich Steiner, et al. "A bicontinuous double gyroid hybrid solar cell." In: *Nano letters* 9.8 (2009), pp. 2807–2812.

[156] Seungmin Yoo, Jung-Hwan Kim, Myoungsoo Shin, Hyungmin Park, Jeong-Hoon Kim, Sang-Young Lee, and Soojin Park. "Hierarchical multiscale hyperporous block copolymer membranes via tunable dual-phase separation." In: *Science advances* 1.6 (2015), e1500101.

[157] Volker Abetz. "Isoporous block copolymer membranes." In: *Macromolecular rapid communications* 36.1 (2015), pp. 10–22.

[158] Sabine Ludwigs, Alexander Böker, Andrej Voronov, Nicolaus Rehse, Robert Magerle, and Georg Krausch. "Self-assembly of functional nanostructures from ABC triblock copolymers." In: *Nature materials* 2.11 (2003), pp. 744–747.

[159] Morgan Stefik, Stefan Guldin, Silvia Vignolini, Ulrich Wiesner, and Ullrich Steiner. "Block copolymer self-assembly for nanophotonics." In: *Chemical Society Reviews* 44.15 (2015), pp. 5076–5091.

[160] V Abetz and A Boschetti-de Fierro. "Block copolymers in the condensed state." In: (2012).

[161] Wei Zheng and Zhen-Gang Wang. "Morphology of ABC triblock copolymers." In: *Macromolecules* 28.21 (1995), pp. 7215–7223.

[162] Yanfei Liu, Volker Abetz, and Axel HE Müller. "Janus cylinders." In: *Macromolecules* 36.21 (2003), pp. 7894–7898.

[163] Rainer Erhardt, Alexander Böker, Heiko Zettl, Håkon Kaya, Wim Pyckhout-Hintzen, Georg Krausch, Volker Abetz, and Axel HE Müller. "Janus micelles." In: *Macromolecules* 34.4 (2001), pp. 1069–1075.

[164] Andreas Walther, Xavier André, Markus Drechsler, Volker Abetz, and Axel HE Müller. "Janus discs." In: *Journal of the American Chemical Society* 129.19 (2007), pp. 6187–6198.

[165] Andrea Wolf, Andreas Walther, and Axel HE Müller. "Janus triad: Three types of nonspherical, nanoscale janus particles from one single triblock terpolymer." In: *Macromolecules* 44.23 (2011), pp. 9221–9229.

[166] Shimei Jiang, Astrid Göpfert, and Volker Abetz. "Novel morphologies of block copolymer blends via hydrogen bonding." In: *Macromolecules* 36.16 (2003), pp. 6171–6177.

[167] Clemens Auschra and Reimund Stadler. "Synthesis of block copolymers with poly (methyl methacrylate): P (Bb-MMA), P (EB-b-MMA), P (SbBb-MMA) and P (Sb-EB-b-MMA)." In: *Polymer Bulletin* 30.3 (1993), pp. 257–264.

[168] Reimund Stadler, Clemens Auschra, Joerg Beckmann, Udo Krappe, Ingrid Voight-Martin, and Ludwik Leibler. "Morphology and thermodynamics of symmetric poly (A-block-B-block-C) triblock copolymers." In: *Macromolecules* 28.9 (1995), pp. 3080–3097.

[169] Ulrike Breiner, Udo Krappe, Volker Abetz, and Reimund Stadler. "Cylindrical morphologies in asymmetric ABC triblock copolymers." In: *Macromolecular Chemistry and Physics* 198.4 (1997), pp. 1051–1083.

[170] Ulrike Breiner, Udo Krappe, Thomas Jakob, Volker Abetz, and Reimund Stadler. "Spheres on spheres–a novel spherical multiphase morphology in polystyrene-block-polybutadiene-block-poly (methyl methacrylate) triblock copolymers." In: *Polymer Bulletin* 40.2 (1998), pp. 219–226.

[171] PG Bolhuis, AA Louis, JP Hansen, and EJ Meijer. "Accurate effective pair potentials for polymer solutions." In: *The Journal of Chemical Physics* 114.9 (2001), pp. 4296–4311.

[172] Robert D Groot and Timothy J Madden. "Dynamic simulation of diblock copolymer microphase separation." In: *The Journal of chemical physics* 108.20 (1998), pp. 8713–8724.

[173] Dahuan Liu and Chongli Zhong. "Dissipative particle dynamics simulation of microphase separation and properties of linear–dendritic diblock copolymer melts under steady shear flow." In: *Macromolecular rapid communications* 26.24 (2005), pp. 1960–1964.

[174] Pavel Petrus, Martin Lísal, and John K Brennan. "Self-assembly of lamellar- and cylinder-forming diblock copolymers in planar slits: insight from dissipative particle dynamics simulations." In: *Langmuir* 26.18 (2010), pp. 14680–14693.

[175] Alexey A Gavrilov, Yaroslav V Kudryavtsev, and Alexander V Chertovich. "Phase diagrams of block copolymer melts by dissipative particle dynamics simulations." In: *The Journal of chemical physics* 139.22 (2013), p. 224901.

[176] Felix H Schacher, Hidekazu Sugimori, Song Hong, Hiroshi Jinnai, and Axel HE Müeller. "Tetragonally Perforated Lamellae of Polybutadiene-block-poly (2-vinylpyridine)-block-poly (tert-butyl methacrylate)(BVT) Triblock Terpolymers in the Bulk: Preparation, Cross-Linking, and Dissolution." In: *Macromolecules* 45.19 (2012), pp. 7956–7963.

[177] William Humphrey, Andrew Dalke, and Klaus Schulten. "VMD: visual molecular dynamics." In: *Journal of molecular graphics* 14.1 (1996), pp. 33–38.

[178] Joerg Kressler, Noboru Higashida, Ken Shimomai, Takashi Inoue, and Toshiaki Ougizawa. "Temperature Dependence of the Interaction Parameter between Polystyrene and Poly (methyl methacrylate)." In: *Macromolecules* 27.9 (1994), pp. 2448–2453.

[179] Eva Betthausen, Martin Dulle, Christoph Hanske, Melanie Müller, Andreas Fery, Stephan Förster, Felix H Schacher, and Axel HE Müeller. "Nanoporous sheets and cylinders via bulk templating of triblock terpolymer/homopolymer blends." In: *Macromolecules* 47.18 (2014), pp. 6289–6301.

[180] Klaus-Viktor Peinemann, Volker Abetz, and Peter FW Simon. "Asymmetric superstructure formed in a block copolymer via phase separation." In: *Nature materials* 6.12 (2007), pp. 992–996.

[181] Janina Hahn, Volkan Filiz, Sofia Rangou, Juliana Clodt, Adina Jung, Kristian Buhr, Clarissa Abetz, and Volker Abetz. "Structure formation of integral-asymmetric membranes of polystyrene-block-Poly (ethylene oxide)." In: *Journal of Polymer Science Part B: Polymer Physics* 51.4 (2013), pp. 281–290.

[182] Yong Wang, Ling Tong, and Martin Steinhart. "Swelling-induced morphology reconstruction in block copolymer nanorods: Kinetics and impact of surface tension during solvent evaporation." In: *ACS nano* 5.3 (2011), pp. 1928–1938.

[183] Jay R Werber, Chinedum O Osuji, and Menachem Elimelech. "Materials for next-generation desalination and water purification membranes." In: *Nature Reviews Materials* 1.5 (2016), pp. 1–15.

[184] Hao-Cheng Yang, Jingwei Hou, Vicki Chen, and Zhi-Kang Xu. "Janus membranes: exploring duality for advanced separation." In: *Angewandte Chemie International Edition* 55.43 (2016), pp. 13398–13407.

[185] Jiangping Xu, Ke Wang, Jingyi Li, Huamin Zhou, Xiaolin Xie, and Jintao Zhu. "ABC triblock copolymer particles with tunable shape and internal structure through 3D confined assembly." In: *Macromolecules* 48.8 (2015), pp. 2628–2636.

[186] Jiangping Xu, Yi Yang, Ke Wang, Jingyi Li, Huamin Zhou, Xiaolin Xie, and Jintao Zhu. "Additives induced structural transformation of ABC triblock copolymer particles." In: *Langmuir* 31.40 (2015), pp. 10975–10982.

[187] Xiaolian Qiang, Steffen Franzka, Xuezhi Dai, and André H Gröschel. "Multicompartment Microparticles of SBT Triblock Terpolymers through 3D Confinement Assembly." In: *Macromolecules* 53.11 (2020), pp. 4224–4233.

[188] Giada Quintieri, Marco Saccone, Matthias Spengler, Michael Giese, and André H Gröschel. "Supramolecular modification of abc triblock terpolymers in confinement assembly." In: *Nanomaterials* 8.12 (2018), p. 1029.

[189] Xiaolian Qiang, Xuezhi Dai, Andrea Steinhaus, and André H Gröschel. "Multicompartment microparticles with Patchy Topography through solvent-adsorption annealing." In: *ACS Macro Letters* 8.12 (2019), pp. 1654–1659.

[190] Andrea Steinhaus, Ramzi Chakroun, Markus Müllner, Tai-Lam Nghiem, Marcus Hildebrandt, and Andreé H Gröschel. "Confinement assembly of ABC triblock terpolymers for the high-yield synthesis of Janus nanorings." In: *ACS nano* 13.6 (2019), pp. 6269–6278.

[191] Johannes Schindelin, Ignacio Arganda-Carreras, Erwin Frise, Verena Kaynig, Mark Longair, Tobias Pietzsch, Stephan Preibisch, Curtis Rueden, Stephan Saalfeld, Benjamin Schmid, et al. "Fiji: an open-source platform for biological-image analysis." In: *Nature methods* 9.7 (2012), pp. 676–682.

[192] Andrea Steinhaus, Deepika Srivastva, Arash Nikoubashman, and André H Gröschel. "Janus Nanostructures from ABC/B Triblock Terpolymer Blends." In: *Polymers* 11.7 (2019), p. 1107.

[193] Carolyn L Phillips, Joshua A Anderson, and Sharon C Glotzer. "Pseudo-random number generation for Brownian Dynamics and Dissipative Particle Dynamics simulations on GPU devices." In: *Journal of Computational Physics* 230.19 (2011), pp. 7191–7201.

[194] G Ronca and TP Russell. "Concentration fluctuations of polystyrene-polybutadiene blends." In: *Physical Review B* 35.16 (1987), p. 8566.

[195] Kie Hyun Nam and Won Ho Jo. "The effect of molecular weight and polydispersity of polystyrene on the interfacial tension between polystyrene and polybutadiene." In: *Polymer* 36.19 (1995), pp. 3727–3731.

[196] Craig J Carriere, Girma Biresaw, and Robert L Sammler. "Temperature dependence of the interfacial tension of PS/PMMA, PS/PE, and PMMA/PE blends." In: *Rheologica acta* 39.5 (2000), pp. 476–482.

[197] Jae Man Shin, Minsoo P Kim, Hyunseung Yang, Kang Hee Ku, Se Gyu Jang, Kyung Ho Youm, Gi-Ra Yi, and Bumjoon J Kim. "Monodipserse nanostructured spheres of block copolymers and nanoparticles via cross-flow membrane emulsification." In: *Chemistry of Materials* 27.18 (2015), pp. 6314–6321.

[198] Jae Man Shin, YongJoo Kim, Hongseok Yun, Gi-Ra Yi, and Bumjoon J Kim. "Morphological evolution of block copolymer particles: effect of solvent evaporation rate on particle shape and morphology." In: *ACS nano* 11.2 (2017), pp. 2133–2142.

[199] Irving Langmuir. "The evaporation of small spheres." In: *Physical review* 12.5 (1918), p. 368.

[200] Wendong Liu, Jiarul Midya, Michael Kappl, Hans-Jürgen Butt, and Arash Nikoubashman. "Segregation in drying binary colloidal droplets." In: *ACS nano* 13.5 (2019), pp. 4972–4979.

[201] G Floudas, Tadeusz Pakula, Erhard W Fischer, N Hadjichristidis, and S Pispas. "Ordering kinetics in a symmetric diblock copolymer." In: *Acta polymerica* 45.3 (1994), pp. 176–181.

[202] Yi Wang, Bao-Hua Guo, Xian Wan, Jun Xu, Xin Wang, and Yin-Ping Zhang. "Janus-like polymer particles prepared via internal phase separation from emulsified polymer/oil droplets." In: *Polymer* 50.14 (2009), pp. 3361–3369.

[203] Hiroshi Yabu, Shunsuke Sato, Takeshi Higuchi, Hiroshi Jinnai, and Masatsugu Shimomura. "Creating suprapolymer assemblies: nanowires, nanorings, and nanospheres prepared from symmetric block-copolymers confined in spherical particles." In: *Journal of Materials Chemistry* 22.16 (2012), pp. 7672–7675.

[204] Peng Chen, Haojun Liang, and An-Chang Shi. "Origin of microstructures from confined asymmetric diblock copolymers." In: *Macromolecules* 40.20 (2007), pp. 7329–7335.

[205] Stefanie Tjaberings, Markus Heidelmann, Alexander Tjaberings, Andrea Steinhaus, Steffen Franzka, Bernd Walkenfort, and André H Gröschel. "Terpolymer Multicompartment Nanofibers as Templates for Hybrid Pt Double Helices." In: *ACS Applied Materials & Interfaces* 12.35 (2020), pp. 39586–39594.

[206] Tai-Lam Nghiem, Deniz Coban, Stefanie Tjaberings, and André H Gröschel. "Recent Advances in the Synthesis and Application of Polymer Compartments for Catalysis." In: *Polymers* 12.10 (2020), p. 2190.

[207] Bohdana M Discher, You-Yeon Won, David S Ege, James CM Lee, Frank S Bates, Dennis E Discher, and Daniel A Hammer. "Polymersomes: tough vesicles made from diblock copolymers." In: *Science* 284.5417 (1999), pp. 1143–1146.

[208] Léa Messager, Jens Gaitzsch, Luca Chierico, and Giuseppe Battaglia. "Novel aspects of encapsulation and delivery using polymersomes." In: *Current opinion in pharmacology* 18 (2014), pp. 104–111.

[209] Kasper Renggli, Patric Baumann, Karolina Langowska, Ozana Onaca, Nico Bruns, and Wolfgang Meier. "Selective and responsive nanoreactors." In: *Advanced Functional Materials* 21.7 (2011), pp. 1241–1259.

[210] Dennis E Discher, Vanessa Ortiz, Goundla Srinivas, Michael L Klein, Younghoon Kim, David Christian, Shenshen Cai, Peter Photos, and Fariyal Ahmed. "Emerging applications of polymersomes in delivery: from molecular dynamics to shrinkage of tumors." In: *Progress in polymer science* 32.8-9 (2007), pp. 838–857.

[211] Vimalkumar Balasubramanian, Bárbara Herranz-Blanco, Patrick V Almeida, Jouni Hirvonen, and Hélder A Santos. "Multifaceted polymersome platforms: Spanning from self-assembly to drug delivery and protocells." In: *Progress in Polymer Science* 60 (2016), pp. 51–85.

[212] Corinne Nardin, J Widmer, M Winterhalter, and W Meier. "Amphiphilic block copolymer nanocontainers as bioreactors." In: *The European Physical Journal E* 4.4 (2001), pp. 403–410.

[213] NA Spenley. "Scaling laws for polymers in dissipative particle dynamics." In: *EPL (Europhysics Letters)* 49.4 (2000), p. 534.

[214] Joshua A Anderson, Jens Glaser, and Sharon C Glotzer. "HOOMD-blue: A Python package for high-performance molecular dynamics and hard particle Monte Carlo simulations." In: *Computational Materials Science* 173 (2020), p. 109363.

[215] Paul Dalhaimer, Adam J Engler, Ranganath Parthasarathy, and Dennis E Discher. "Targeted worm micelles." In: *Biomacromolecules* 5.5 (2004), pp. 1714–1719.

[216] Vanessa Ortiz, Steven O Nielsen, Dennis E Discher, Michael L Klein, Reinhard Lipowsky, and Julian Shillcock. "Dissipative particle dynamics simulations of polymersomes." In: *The Journal of Physical Chemistry B* 109.37 (2005), pp. 17708–17714.

[217] Susumu Saeki, Nobuhiro Kuwahara, Mitsuo Nakata, and Motozo Kaneko. "Upper and lower critical solution temperatures in poly (ethylene glycol) solutions." In: *Polymer* 17.8 (1976), pp. 685–689.

[218] Allan FM Barton. *Handbook of polymer-liquid interaction parameters and solubility parameters*. CRC press, 1990.

[219] Ying Zhao, Li-Yan You, Zhong-Yuan Lu, and Chia-Chung Sun. "Dissipative particle dynamics study on the multicompartment micelles self-assembled from the mixture of diblock copolymer poly (ethyl ethylene)-block-poly (ethylene oxide) and homopolymer poly (propylene oxide) in aqueous solution." In: *Polymer* 50.22 (2009), pp. 5333–5340.

[220] Mengying Xiao, Jiannan Liu, Jiexin Yang, Rong Wang, and Daiqian Xie. "Biomimetic membrane control of block copolymer vesicles with tunable wall thickness." In: *Soft Matter* 9.8 (2013), pp. 2434–2442.

[221] Evgeniia V Konishcheva, Ulmas E Zhumaev, and Wolfgang P Meier. "PEO-b-PCL-b-PMOXA triblock copolymers: from synthesis to microscale polymersomes with asymmetric membrane." In: *Macromolecules* 50.4 (2017), pp. 1512–1520.